

Simulation of the Sudbury Neutrino Observatory Neutral Current Detectors

Hok Seum Wan Chan Tseung
Wadham College, Oxford

Thesis submitted in partial fulfilment of the requirements
for the degree of Doctor of Philosophy
at the University of Oxford
Trinity Term 2008

Simulation of the Sudbury Neutrino Observatory Neutral Current Detectors

Hok Seum Wan Chan Tseung
Wadham College, Oxford

Thesis submitted in partial fulfilment of the requirements for the
degree of Doctor of Philosophy at the University of Oxford
Trinity Term 2008

Abstract

The Sudbury Neutrino Observatory (SNO), a heavy water Cherenkov experiment, was designed to detect solar ^8B neutrinos via their elastic scattering interactions on electrons, or charge current and neutral current (NC) interactions on deuterium. In the third phase of SNO, an array of ^3He proportional counters was deployed to detect neutrons produced in NC interactions.

A simulation of the current pulses and energy spectra of the main kinds of ionization events inside these Neutral Current Detectors (NCDs) was developed. To achieve this, electron drift times in NCDs were evaluated with a Monte Carlo method, and constrained by using wire alpha activity inside the counters. The pulse calculation algorithm applies to any ionization event, and takes into account processes such as straggling, electron diffusion, and propagation through the NCD hardware. A space charge model was developed to fully explain the energy spectra of neutron and alpha events. Comparisons with data allowed the various classes of alpha backgrounds to be identified, and gave evidence for the spatial non-uniformity of ^{238}U and ^{232}Th chain nuclei in the counter walls.

The simulation was applied to determine the fractional contents of the main types of alpha backgrounds in each NCD string. The number of neutron capture events in the array was extracted via a statistical separation, using Monte Carlo generated alpha background pulse shape parameter distributions and minimal energy information. The inferred total ^8B solar neutrino flux is:

$$\Phi_{NC} = 5.74 \pm 0.77 \text{ (stat.)} \pm 0.39 \text{ (sys.)} \times 10^6 \text{ cm}^{-2}\text{s}^{-1}$$

in agreement with Standard Solar Model predictions and previous SNO results.

To my parents

Acknowledgements

I am greatly indebted to the Oxford SNO group: Profs. Nick Jelley and Steve Biller, Dr. Simon Peeters, Dr. Nick West, and my office-mates over the years: Drs. Jeanne Wilson, Jessica Dunmore, Charlotte Sims, James Loach, Helen O’Keeffe and Gabriel Orebi-Gann.

It has been an immense pleasure to be part of the SNO collaboration and the NCD group, and to work with Noah Oblath, Prof. Hamish Robertson, Prof. Hans Bichsel, Drs. Sean McGee, Keith Rielage, Jocelyn Monroe, Gersende Prior and Berta Beltran on NCD simulation.

I am grateful to the many friends who helped me during my time as a graduate student, in particular: Chen-Chi Lin, Ryan Wei, Matthew Bladen, Merim Bilalic, Mrs. Gilbert, Melin Huang, Adam Cox and Charles Duba. Most of all, I thank my family for their unwavering support.

This work was sponsored by the Oxford University Press and Wadham College through a Clarendon Fund Scholarship, an ORS award, and the University of Washington through a visiting studentship.

Contents

1	Introduction	1
1.1	Summary of neutrino properties	1
1.2	Neutrino oscillations	1
1.3	Solar neutrinos	3
1.4	The SNO experiment	4
2	Neutral Current Detectors	8
2.1	Counter properties	8
2.2	Electronics	12
2.3	Calibration	13
2.4	Signals	13
2.5	Aims and outline of this thesis	16
3	Electron Transport in NCDs	19
3.1	Simulation method	21
3.1.1	Difference equations	21
3.1.2	Null collision technique	22
3.1.3	Kinematics of isotropic collisions	24
3.1.4	Anisotropic collisions	25
3.2	Implementation and benchmarking	25
3.2.1	Drift speeds at constant fields	27
3.2.2	Diffusion coefficients in ^4He and CF_4 at constant fields	30
3.3	Results	32
3.3.1	Drift and time resolution in NCD counters	32
3.3.2	Corrected drift curve	36
3.3.3	z resolution	37
3.3.4	Charge distributions	37
3.4	Summary	41
4	Simulation of NCD Pulses	43
4.1	Method	43
4.2	Current from point charges	46
4.3	Protons, tritons and alphas in NCDs	48
4.3.1	Stopping and range of ions in NCD gas	48

4.3.2	Proton, triton and α particle tracks	50
4.3.3	Straight track approximation	53
4.3.4	Energy straggling of ions in NCD gas	54
4.4	β particles	55
4.5	Hardware model	56
4.5.1	Pulse reflections	56
4.5.2	Propagation along NCD wires	59
4.5.3	Electronics and DAQ	59
4.5.4	Simulation of NCD baseline noise	61
4.6	Data-Monte Carlo comparisons	67
4.6.1	Neutron pulse shape parameter distributions	68
4.6.2	Low energy α pulse shape parameter distributions	70
4.7	Non-standard α pulses	73
4.7.1	Wire α events	73
4.7.2	End-effect α events	74
4.8	Summary	77
5	Simulation of NCD Energy Spectra	79
5.1	Gas gain	80
5.2	Simulation of space charge effects	80
5.2.1	Motivation	80
5.2.2	Simulation method	83
5.2.3	Model optimization	85
5.2.4	Model predictions	87
5.3	Energy resolution	90
5.4	Straggling of α particles in nickel	90
5.5	Alpha energy spectra	92
5.5.1	^{210}Po spectrum	92
5.5.2	Bulk spectra	93
5.6	Background content of NCD strings	98
5.7	β energy spectrum	102
5.7.1	Estimation of the β event rate	102
5.7.2	Simulation method	103
5.8	Summary	106
6	Separation of Neutrons and Alphas	108
6.1	Representation of alphas below 1 MeV	109
6.2	Alpha $R_{10,40}$ parameter distributions	112
6.2.1	Instrumental systematics	113
6.2.2	Physics model uncertainties	116
6.2.3	Wire, end-cap and other neutron-like alphas	116
6.2.4	Comparisons with α data	117
6.3	Extraction of neutrons	117
6.3.1	Fit procedure	117

6.3.2	Results	119
6.4	The neutral current flux	120
6.4.1	Discussion	122
7	Summary and Conclusions	124
A	String-by-string differences	126
B	^{238}U and ^{232}Th chains	128
C	Semi-analytic pulse calculation	129
D	Pulse shape parameters	131
E	Software implementation	133
F	Low energy bulk α spectra	134
G	Coincidence events	135
H	List of neutron-like alpha pulses	136
	Bibliography	138

List of Figures

1.1	Solar neutrino energy spectra, and MSW electron neutrino survival probability as a function of energy for ^8B neutrinos	3
1.2	Neutrino fluxes from the SNO salt phase	5
1.3	Schematic of the SNO detector	7
2.1	Schematic of an NCD string	10
2.2	The NCD array configuration	11
2.3	The NCD Electronics and DAQ system	14
2.4	Example NCD shaper ADC spectra and pulses	17
3.1	Describing the path of an electron in NCD gas	22
3.2	Flow diagram for e^- transport MC	26
3.3	Calculation of e^- drift speeds in Ar	28
3.4	Calculation of e^- drift speeds in CH_4	29
3.5	Calculation of e^- drift speeds in He	29
3.6	Calculation of e^- drift speeds in CF_4	30
3.7	Calculations of e^- drift speeds in 80:20 and 90:10 ^3He and CF_4 mixtures	31
3.8	Calculations of D_T/μ_e , the transverse diffusion coefficient to mobility ratio in CF_4 and He for electrons	31
3.9	Calculated e^- drift times in NCD gas, with experimental constraints	34
3.10	$pw30$ vs Energy scatter plots for alphas	35
3.11	Predicted time resolution due to e^- diffusion, and calculated z distributions of avalanche electrons at the NCD anode	35
3.12	Scaling of e^- drift times using wire α events	37
3.13	An example simulated e^- avalanche at the anode	39
3.14	Simulated z -profile of electrons at the anode in multiple avalanches	40
4.1	Steps in the calculation of I_{track} for a $p-t$ event	45
4.2	Example simulated NCD events: $p-t$, α and β	47
4.3	Stopping powers and ranges of protons, tritons and alphas in NCD gas	51
4.4	Simulated proton and α particle tracks in NCD gas	53
4.5	Lateral straggling of alphas in NCD gas	54
4.6	Definition of track parameters for straight line travel	55
4.7	Simplified electronics model	57
4.8	Average micro-discharge pulse from string 27, compared with simulation	59

4.9	Effects of NCD hardware on pulse shape	60
4.10	Validation of noise simulation technique	64
4.11	Plot of μ_e vs σ_g for NCD noise	65
4.12	Baseline NCD noise spectra from electronic calibration runs	66
4.13	Variation of baseline noise RMS with time, and stability of noise power spectra	66
4.14	An example simulated baseline noise train	67
4.15	Comparisons of simulated neutron pulse width distributions with data . . .	69
4.16	Comparisons of simulated neutron pulse shape moment distributions with data	71
4.17	Biases on MC pulse shape distributions due to differing MUX electronics .	72
4.18	Impact of bulk impurity depths on simulated α pulse parameter distributions	73
4.19	Example recorded and simulated wire α events	74
4.20	Equipotential lines at counter ends	75
4.21	Expected end-cap alphas fractions as a function of energy	76
4.22	Candidate α pulse from a silica feedthrough	77
4.23	Comparisons of simulated $pw40$ -Energy space with data for all known ionization event types	78
5.1	Dependence of NCD gas gain with voltage, compared with Diethorn model predictions	81
5.2	Effects of space charge on mono-energetic peaks	81
5.3	Compelling evidence for space charge effects	83
5.4	Optimization of space charge model variables	86
5.5	Dependence of space charge charge loss on θ for neutrons, and an example simulated neutron energy spectrum	88
5.6	Dependence of space charge charge loss on θ for neutrons, and an example simulated ^{210}Po α energy spectrum	89
5.7	Straggling of α particles in Ni	91
5.8	Simulated ^{210}Po energy spectrum compared to data, and dependence of the low energy ^{210}Po spectrum shape on mean impurity depth	92
5.9	Selection of bulk α events in $pw50$ vs Energy space	94
5.10	Evidence for non-uniformity of bulk impurity profiles	96
5.11	Variation of bulk spectral shapes with mean impurity depths	97
5.12	Fitting the NCD α energy spectrum with MC-generated ^{210}Po , ^{238}U and ^{232}Th pdfs	101
5.13	Expected yield of β events above 200 keV	103
5.14	Parametrization of β spectra	105
5.15	Simulated NCD β spectrum of ^{238}U and ^{232}Th electrons	106
6.1	Type I and II alphas in $pw50$ vs Energy space	110
6.2	Pulse moment pdfs from NCD data in the neutron energy region, compared to a combination of neutron and type I and II α pdfs	111
6.3	Biases on the mean value of $R_{10,40}$ arising from MUX differences	114

6.4	Physics model uncertainties on $R_{10,40}$	115
6.5	End-cap and neutron-like alpha cut	116
6.6	Comparisons of MC type I and II $R_{10,40}$ pdfs to α data	118
6.7	$R_{10,40}$ NCD data in the neutron energy region fitted to neutron calibration and MC $R_{10,40}$ type I and II α pdfs	121
6.8	SNO NC flux results	123
B.1	The ^{238}U chain	128
B.2	The ^{232}Th chain	128
D.1	Definitions of pulse widths and amplitude rise times	132
G.1	^{220}Rn and ^{216}Po α coincidence events from the ^{232}Th chain	135
H.1	Examples of neutron-like wide alpha pulses	137

List of Tables

1.1	Magnitude of solar neutrino fluxes	3
2.1	Summary of NCD counter properties	11
3.1	Values of K used in the null collision algorithm for e^- transport simulation	27
3.2	Summary of e^- transport MC calculated parameters	42
4.1	Constants for the parameterization of S_e for protons passing through He, C and F	50
4.2	Constants used in the NCD electronics simulation	61
4.3	Percentages of invisible and distorted neutron events in the NCD array . .	75
4.4	Estimated percentages of invisible and distorted ^{238}U , ^{232}Th and ^{210}Po α events in an NCD string of average length	76
5.1	Space charge model input values	85
5.2	Estimated ^{238}U , ^{232}Th , ^{210}Po and wire α contents of NCD strings	100
5.3	Constants used in the parameterization of β spectra	104
5.4	Fractions of ^{238}U and ^{232}Th β decays resulting in an electron penetrating the live region with over 200 keV K.E.	105
6.1	Decomposition of ^{238}U α pdfs, at different impurity depths, into type I and II α pdfs	112
6.2	Parameterization of the mean value of $R_{10,40}$ as a function of E for type I and II alphas	114
6.3	Additional variance in observed $R_{10,40}$ distributions	114
6.4	Physics model uncertainties on $R_{10,40}$	115
6.5	Summary of systematic errors on the extracted neutron fraction	120
6.6	Summary of neutron backgrounds in the NCD array	122
A.1	String-by-string differences	127
H.1	A list of neutron-like alpha pulses in the energy range $0.9 < E < 1.2$ MeV .	136

Glossary

AV Acrylic Vessel

BS05 J. Bahcall and A. Serenelli's Standard Solar Model (2005).

CC Charged Current

correlated scope-shaper pair A correlated scope-shaper pair consists of a shaper and a MUX-scope event that triggered within 10 μ s of each other, and originating from the same string.

CVD Chemical Vapour Deposition

DAQ Data AcQuisition

EGS Electron Gamma Shower

ES Elastic Scattering

FFT Fast Fourier Transform

FWHM Full Width at Half Maximum

GTID Global Trigger IDentification

K.E. Kinetic Energy

K-S Kolmogorov-Smirnov

LMA Large Mixing Angle

MC Monte Carlo

MCNP Monte Carlo N-Particle

MSW Mikheyev-Smirnov-Wolfenstein

MUX MUltipleXer

NC Neutral Current

NCD Neutral Current Detector

neutron energy window This refers to the energy range from 0.2 MeV to 0.9 MeV, which contains all neutron events.

neutron peak A sharper energy spectrum peak appearing at 764 keV, resulting from fully-contained proton-triton tracks.

pdf probability density function

PMNS Pontecorvo-Maki-Nakagawa-Sakata

PMT PhotoMultiplier Tube

p-t proton-triton

RMS Root Mean Square

SM Standard Model

SNO Sudbury Neutrino Observatory

SNOMAN SNO Monte carlo and Analysis program

SNP Solar Neutrino Problem

SRIM Stopping and Range of Ions in Matter

SSM Standard Solar Model

TRIM TRansport of Ions in Matter

ZBL Ziegler-Biersack-Littmark

Chapter 1

Introduction

1.1 Summary of neutrino properties

Neutrinos are the neutral, colourless spin- $\frac{1}{2}$ partners of the charged leptons (e, μ, τ). Postulated by Pauli from considerations of β decay experiments [1], they were first observed by Reines and Cowan in 1956, through inverse β decay [2, 3]. In the Standard Model (SM), neutrinos interact exclusively via the weak interaction, in two ways: neutral current (NC) interactions, in which Z^0 bosons are exchanged, and charged current (CC) interactions mediated by W^\pm bosons, in which they couple with their charged partners. Observations of Z^0 decays established that there are only three active neutrino flavours: ν_e , ν_μ and ν_τ [4]. ν_μ and ν_τ neutrinos were first observed in 1962 and 2000, respectively [5, 6].

Experimental evidence [7, 8] is consistent with the hypothesis that all neutrinos have negative helicity. This supported the idea of massless, left-handed neutrinos in the SM. The existence of neutrino masses, however, gives rise to mixed helicity states and flavour change, which is discussed next.

1.2 Neutrino oscillations

The time evolution of neutrinos in vacuum is determined by the Hamiltonian $H = H_I + H_P$, where the interaction Hamiltonian H_I incorporates weak interactions during particle production, or detection, and the propagation component H_P describes free motion. The eigenstates of H_I are flavour eigenstates $|\nu_f\rangle$, while those of H_P are mass eigenstates $|\nu_i\rangle$. Flavour eigenstates can be thought of as superpositions of three mass states with

masses m_1 , m_2 and m_3 : $|\nu_f\rangle = \sum_{i=1}^3 U_{fi}|\nu_i\rangle$. U_{fi} is the Pontecorvo-Maki-Nakagawa-Sakata (PMNS) matrix, commonly expressed as $U = V_{23} \cdot V_{13} \cdot V_{12}$, where:

$$V_{23} = \begin{pmatrix} 1 & 0 & 0 \\ 0 & c_{23} & s_{23} \\ 0 & -s_{23} & c_{23} \end{pmatrix}, V_{13} = \begin{pmatrix} c_{13} & 0 & s_{13}e^{i\delta} \\ 0 & 1 & 0 \\ -s_{13}e^{i\delta} & 0 & c_{13} \end{pmatrix}, V_{12} = \begin{pmatrix} c_{12} & s_{12} & 0 \\ -s_{12} & c_{12} & 0 \\ 0 & 0 & 1 \end{pmatrix} \quad (1.1)$$

In this parameterization, U_{fi} contains 3 mixing angles θ_{12} , θ_{13} , θ_{23} and a CP-violating phase δ . The sines and cosines of mixing angles are denoted by c and s (e.g. $s_{23} = \sin \theta_{23}$).

The probability of flavour change, after travelling a time t , is $P(\nu_f \rightarrow \nu_g) = |\langle \nu_g(t) | \nu_f \rangle|^2$. This expression is considerably simplified, as (1) $\theta_{13} \sim 0$ [9], and (2) the mass splittings are such that $|\Delta m_{13}^2| \sim |\Delta m_{23}^2| \gg |\Delta m_{21}^2|$. Decoupling of $(|m_1\rangle, |m_2\rangle)$ and $(|m_2\rangle, |m_3\rangle)$ mixing then occurs, because the length scales over which flavour change takes place can be very different in each case. To a good approximation, a two-flavour scenario therefore applies to most experiments, and P takes the simple form:

$$P(\nu_e \rightarrow \nu_\mu) = \sin^2 2\theta_{12} \sin^2 \frac{1.27 \Delta m_{21}^2 x}{E} \quad (1.2)$$

for $(|m_1\rangle, |m_2\rangle)$ mixing. In Eq. 1.2, x , the distance travelled, is in metres, Δm_{21}^2 in eV^2 , and the neutrino energy E in MeV.

In 1978, Wolfenstein remarked that the CC scattering of ν_e with electrons in matter should modify the propagation Hamiltonian H_P to include an additional potential [10]. Correspondingly, the mass eigenstates change from $|\nu_i\rangle$ to $|\nu_{im}\rangle$. In a two-flavour picture, the relation between $|\nu_f\rangle$ and $|\nu_{im}\rangle$ is, again, a rotation matrix, with the matter mixing angle θ_m given by [11]:

$$\tan 2\theta_m = \frac{\tan 2\theta}{1 - \sqrt{2}G_F N_e / (\frac{\Delta m^2}{2E} \cos 2\theta)} \quad (1.3)$$

where N_e is the density of electrons. θ_m can become very large if $\sqrt{2}G_F N_e = \frac{\Delta m^2}{2E} \cos 2\theta$. This matter-induced flavour change enhancement, known as the Mikheyev-Smirnov-Wolfenstein (MSW) effect, plays a vital role in the flavour conversion of solar neutrinos.

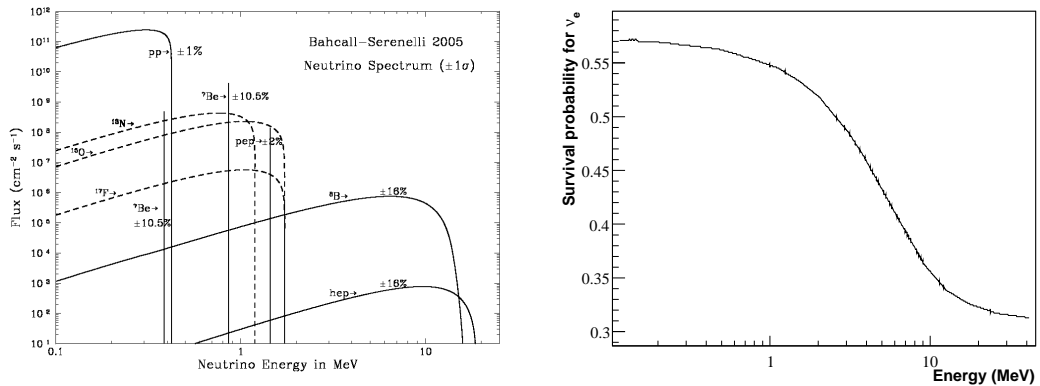
There is now a wealth of evidence (from solar [12, 13], reactor [14], accelerator [15, 16], and atmospheric neutrino [17] experiments) for neutrino oscillations. These experiments determined the oscillation parameters to be: $\Delta m_{21}^2 \sim 8 \times 10^{-5} \text{ eV}^2$, $\Delta m_{32}^2 \sim 0.002 \text{ eV}^2$, $\theta_{12} \sim 33^\circ$, and $\theta_{23} \sim 45^\circ$.

Reaction	Name	Flux ($\text{cm}^{-2}\text{s}^{-1}$)
$pp \rightarrow de^+\nu_e$	pp	$5.99(1.00 \pm 0.01) \times 10^{10}$
$pe^+p \rightarrow d\nu_e$	pep	$1.42(1.00 \pm 0.02) \times 10^8$
${}^3\text{He}p \rightarrow {}^4\text{He}e^+\nu_e$	hep	$7.93(1.00 \pm 0.16) \times 10^3$
${}^7\text{Be}e^- \rightarrow {}^7\text{Li}\nu_e\gamma$	${}^7\text{Be}$	$4.84(1.00 \pm 0.11) \times 10^9$
${}^8\text{B} \rightarrow {}^8\text{Be}^*e^+\nu_e$	${}^8\text{B}$	$5.69(1.00 \pm 0.16) \times 10^6$
${}^{13}\text{N} \rightarrow {}^{13}\text{C}e^+\nu_e$	${}^{13}\text{N}$	$3.07(1.00^{+0.31}_{-0.28}) \times 10^8$
${}^{15}\text{O} \rightarrow {}^{15}\text{N}e^+\nu_e$	${}^{15}\text{O}$	$2.33(1.00^{+0.33}_{-0.29}) \times 10^8$
${}^{17}\text{F} \rightarrow {}^{17}\text{O}e^+\nu_e$	${}^{17}\text{F}$	$5.84(1.00 \pm 0.52) \times 10^6$

Table 1.1: The magnitude of solar neutrino fluxes, as predicted by the BS05 SSM [18].

1.3 Solar neutrinos

The Sun is an intense source of electron-type neutrinos produced in fusion reactions in its core. The expected ν_e fluxes at the Earth, from the different reactions comprising the fusion chains, can be calculated by Standard Solar Models (SSM) [18] (table 1.1). The energy spectra of the various ν_e fluxes are shown in fig. 1.1 (left). SSM predictions of solar properties agree very well with helioseismological, and other measurements [19]. However, generations of experiments [20, 21, 22, 23, 24] have reported a deficit in the flux of solar ν_e compared to SSM predictions. These disagreements, commonly referred to as the Solar Neutrino Problem (SNP), are now understood to be consequences of neutrino flavour change.

Figure 1.1: Left: solar neutrino spectra calculated by the BS05 SSM [18]. Right: probability of ${}^8\text{B}$ solar neutrinos reaching the Earth as electron neutrinos.

The actual flavour conversion picture has to take into account the MSW effect in

the Sun. Fig. 1.1 (right) shows the probability of a ${}^8\text{B}$ solar neutrino detected on Earth as an electron neutrino, if $\Delta m^2 = 8 \times 10^{-5} \text{ eV}^2$ and $\theta_{12} = 33^\circ$. The curve follows the equation:

$$P(\nu_e \rightarrow \nu_e) = \frac{1}{2} + \frac{1}{2} \cos 2\theta_m \cos 2\theta_{12} \quad (1.4)$$

approximately [25]. For example, according to Eq. 1.3, a 10 MeV neutrino created at the centre of the Sun experiences resonance at $\sim 0.23R_{sun}$, where R_{sun} is the solar radius¹. At the neutrino production point, $\sin \theta_m \sim 1$ and $\cos \theta_m \sim 0$, *i.e.* the ν_e is created essentially in a $|\nu_{2m}\rangle$ state. Owing to the slow decrease in N_e , the neutrino maintains the same mass eigenstate, until it exits the surface of the Sun with a ν_e content of $\sim \frac{2}{3}$. The chance of detecting it as an electron neutrino on Earth is further suppressed by a factor of ~ 2 due to vacuum oscillations, so that $P(\nu_e \rightarrow \nu_e) \sim \frac{1}{3}$.

1.4 The SNO experiment

The Sudbury Neutrino Observatory (SNO) experiment [26], located at a depth of 2039 m in the INCO Creighton mine in Sudbury, Canada, was designed to detect ${}^8\text{B}$ solar neutrinos. SNO provided the first direct evidence for neutrino flavour change [12]. Together with the KamLAND experiment [14], it confirmed the Large Mixing Angle (LMA) MSW solution as the answer to the SNP. It is now aimed towards a precision measurement of the mixing parameters Δm_{21}^2 and θ_{12} .

SNO consists of a 12 m diameter acrylic vessel (AV) containing 1 kilotonne of D_2O (fig. 1.3), which is shielded from cavity wall backgrounds by ordinary water. An array of 9456 photomultiplier tubes (PMT) surrounds the AV to detect Cherenkov light emitted by charged particles travelling in the D_2O . Neutrinos can interact with deuterium in the heavy water in the following ways:

$$\nu_x + e^- \rightarrow \nu_x + e^- \quad (\text{ES}) \quad (1.5)$$

$$\nu_e + d \rightarrow p + p + e^- \quad (\text{CC}) \quad (1.6)$$

$$\nu_x + d \rightarrow p + n + \nu_x \quad (\text{NC}) \quad (1.7)$$

¹An exponential radial electron density profile N_e is assumed in the Sun in this calculation: $N_e = N_0 e^{-10.54r/R_{sun}}$, with $N_0 = 245 \text{ mol/cm}^3$ [19].

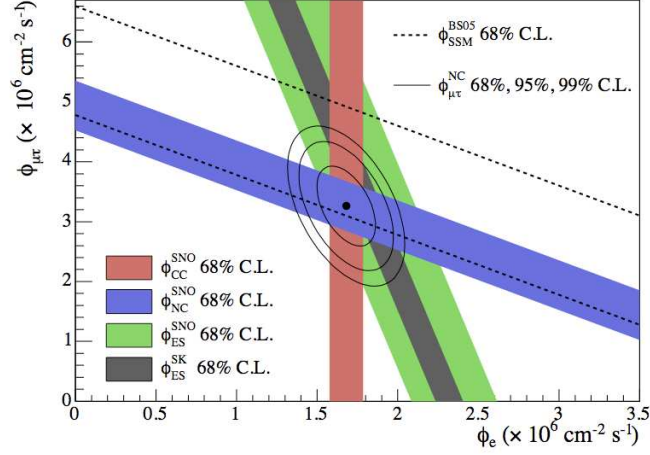


Figure 1.2: The flux of muon, or tau neutrinos vs the flux of electron neutrinos, as measured in the salt phase. The BS05 SSM prediction in a flavour-conversion scenario is shown by the diagonal dashed lines. Figure from [27].

The elastic scattering reaction (ES) is around 6 times more sensitive to ν_e than other flavours, and there is a strong correlation between the outgoing electron and incident neutrino directions. The CC reaction is sensitive only to ν_e , with a threshold of 1.44 MeV. The energy of the outgoing electron is directly related to that of the incident neutrino. Both CC and ES events are detected via Cherenkov light emission by the final state electron. The NC reaction, with a threshold of 2.22 MeV, is totally flavour-blind, and thus, provides a direct measurement of the total ${}^8\text{B}$ solar neutrino flux. Therefore, the ratio of the number of CC to NC events is closely related to the ν_e survival probability.

Each phase of SNO is characterized by a different method for detecting the NC neutron. The first phase observed neutron captures on deuteron via the resulting 6.25 MeV γ -rays. These Compton scattered, producing electrons above Cherenkov threshold that could then be observed. The second phase [27] involved the addition of two tonnes of NaCl to the D_2O , increasing the neutron detection efficiency from 14.4 % in the first phase, to 40.7 %. The inclusion of salt also improved the Cherenkov light yield of NC events, and allowed these to be better separated from CC events². Flux results from the

²The distribution of PMT hits of NC events is more isotropic than CC events, due to multiple γ -ray emissions following neutron capture on ${}^{35}\text{Cl}$.

salt phase are summarized in fig. 1.2. The measured CC, ES and NC fluxes were [27]:

$$\Phi_{CC} = 1.68_{-0.06}^{+0.06}(\text{stat.})_{-0.09}^{+0.08}(\text{sys.}) \times 10^6 \text{ cm}^{-2}\text{s}^{-1} \quad (1.8)$$

$$\Phi_{ES} = 2.35_{-0.22}^{+0.22}(\text{stat.})_{-0.15}^{+0.15}(\text{sys.}) \times 10^6 \text{ cm}^{-2}\text{s}^{-1} \quad (1.9)$$

$$\Phi_{NC} = 4.94_{-0.21}^{+0.21}(\text{stat.})_{-0.34}^{+0.38}(\text{sys.}) \times 10^6 \text{ cm}^{-2}\text{s}^{-1} \quad (1.10)$$

The CC spectrum was also extracted and found to be consistent with an undistorted ^8B neutrino spectrum.

In the third and final phase, an array of 36 ^3He proportional counters, known as Neutral Current Detectors (NCDs), were installed inside the AV (fig. 1.3) [28] to detect NC neutrons, thereby measuring the NC flux in a completely different manner. The addition of NCDs was motivated by the following:

- (1) In the first and second phases, CC and NC events were separated based on their characteristic distributions in a number of observables, *e.g.* reconstructed radius, direction, energy and isotropy. Significant correlations between the CC and NC signals resulted, because of substantial overlaps between the characteristic pdfs. In the NCD phase, CC and NC events could be recorded differently with the PMT and NCD arrays, respectively. The number of NC events coming from the PMT array was decreased considerably. The CC-NC correlation could therefore be reduced significantly, and a measurement of the NC flux could be made without knowing the CC flux.
- (2) Because a different, and essentially independent, detector system was involved, the NC flux measurement carries very different systematic uncertainties in the third phase. This provides a rigorous verification of results from previous phases.

This thesis is concerned with the third phase of SNO, and focusses on data from the NCD counters; PMT data will not be discussed. A description of the NCDs is given next.

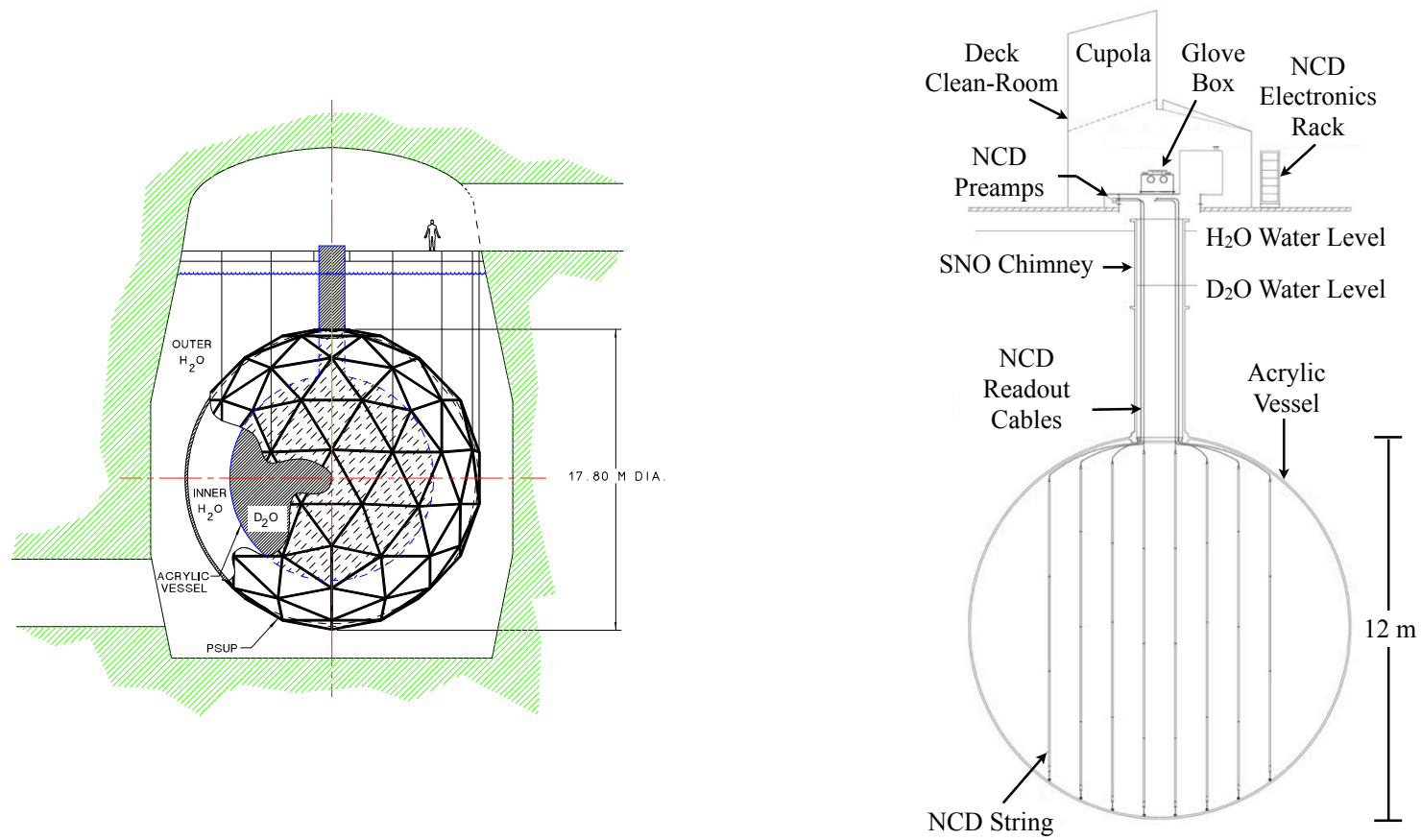


Figure 1.3: Schematic diagram of the SNO detector (left) in its underground cavity. Figure from [26]. Right: the NCD counters inside the AV [29].

Chapter 2

Neutral Current Detectors

2.1 Counter properties

NCDs are ^3He proportional counters made of very low-background materials. Their purpose in SNO was to detect thermalized NC neutrons via the reaction



which has a cross-section of 5316 b. The proton (p) and triton (t) are emitted back-to-back and isotropically, with 573 and 191 keV of kinetic energy, respectively. These particles ionize the counter gas, producing free electrons, which drift towards the anode, and start to multiply at a radius of $\sim 50 \mu\text{m}$. Ions produced in the resulting electron cascade slowly drift towards the cathode. In doing so, the induced charge on the anode changes with time, thus creating a current pulse that can be read off the wire. The total charge contained in the pulse is directly related to the total deposited energy. Therefore, if the particle track is fully-contained in the gas, the pulse integral is a direct measure of the initial particle energy.

NCD gas is a mixture of 85 % ^3He and 15 % CF_4 at 2.5 atm (measured at 297 K). In addition to boosting the gas gain¹ considerably, CF_4 acts as a quencher, and its inclusion results in very good proportional counter pulse imaging properties [30]. The gas proportions and pressure were optimized to the above values, so that: (1) the operating voltage could be kept relatively low, (2) the tubes did not collapse under water, and (3) the length of p - t tracks were short enough for most of them to be fully-contained². Except

¹ CF_4 can be ionized both by accelerated electrons and excited ^3He atoms, since its first ionization energy is lower than the 2^3S or 2^1S states of ^3He .

²The fraction of all p - t tracks that are fully-contained is 0.73.

for very brief spells, NCDs operated at 1950 V (corresponding to a gas gain of 219) and a temperature of ~ 10 C throughout the third phase of SNO.

The typical NCD string (fig. 2.1) was 10 m-long, and consisted of four 2 m-long counters welded together (see table A.1 for the total lengths and number of counters in each string). A 8 cm-long ‘dead volume’, filled with a mixture of Ar and CO₂, was present between successive counters. Counter bodies are around 2.5 cm in radius, 0.037 cm thick, and made of very pure nickel. They were manufactured by Chemical-Vapour-Deposition (CVD) on an aluminium mandrel. This process reduced the ²³⁸U and ²³²Th content in the walls by around 6 orders of magnitude, down to the pg/gNi level. NCD wires, made of high purity copper, are 25 μ m in radius. Each anode is shielded at the counter ends by a 6 cm-long quartz feedthrough, to avoid charge multiplication in regions of distorted electric field.

Data was read out from the top ends of strings only, to minimize the amount of material inserted in the heavy water. All strings were terminated by a 16 cm-long open-ended delay line. Upon formation on the anode, current pulses separate into upward and downward components of nearly equal magnitude. The time lag between the two parts is directly related to the point of formation on the wire. Because it propagates through the delay line, the downward-going pulse is delayed by at least 89 ns with respect to the direct pulse. This allows the vertical capture positions of a fraction of neutron events to be resolved.

The deployed NCD array consisted of 36 ³He and 4 ⁴He strings, arranged as shown in fig. 2.2, with a 1 m inter-string spacing. The array size and configuration were optimized to detect NC neutrons as efficiently as possible, without shadowing too much Cherenkov light: 26.4 % of all NC neutrons were captured by NCDs, and ~ 9 % of Cherenkov photons were absorbed. The ⁴He strings were introduced to study non-neutron backgrounds. They are the only source of high-purity α data that can be used to calibrate simulations. ⁴He α pulse shapes are not expected to be different compared to those from ³He strings; the *set* of ⁴He string pulses, however, is not representative of α backgrounds from the rest of the array. Due to hardware defects, elevated radioactivity, counter gain mismatches and high instrumental background rates, six ³He strings (0, 1, 8, 18, 26, and 31), and one ⁴He string (20) were deemed unsuitable for analysis [31].

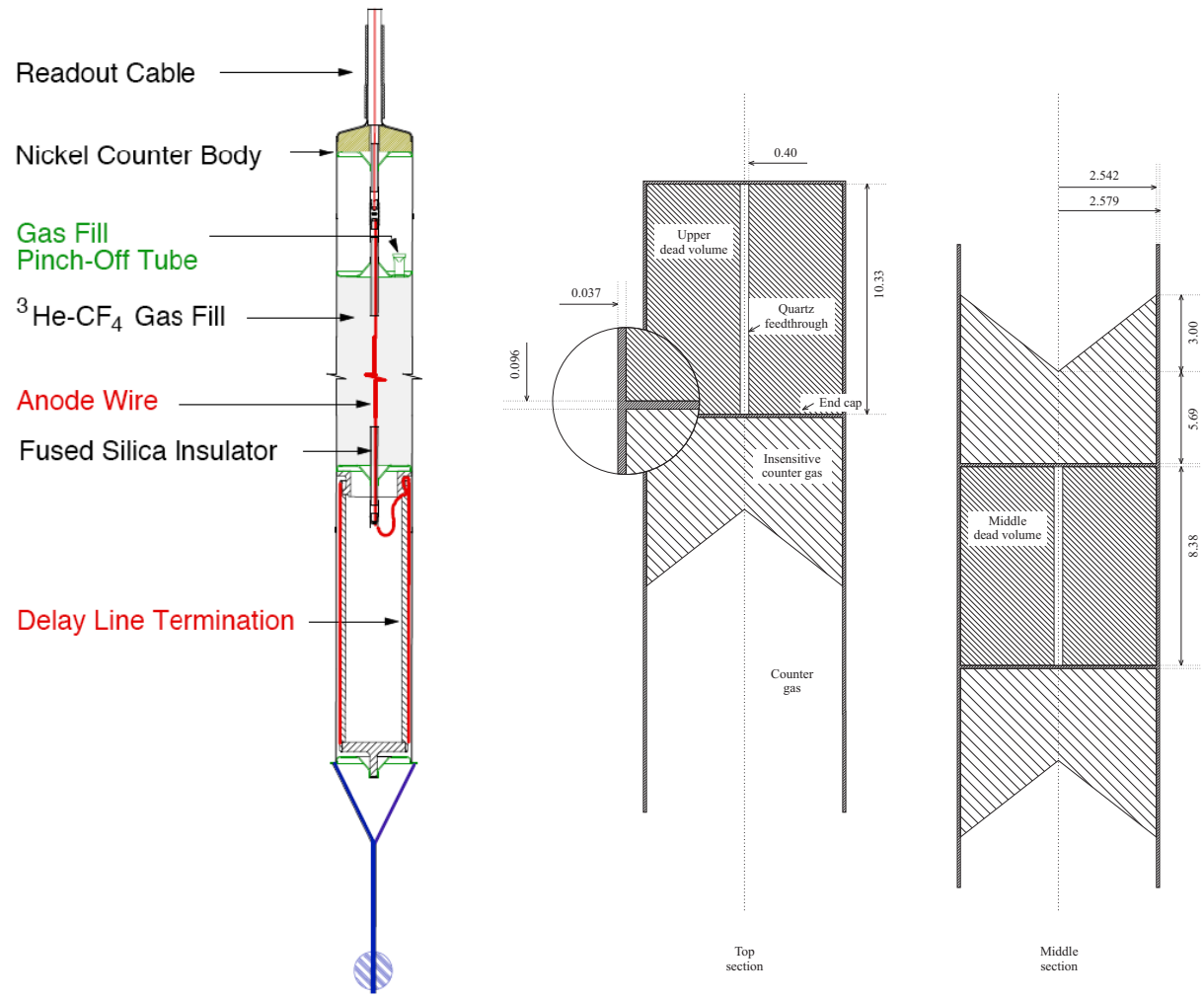
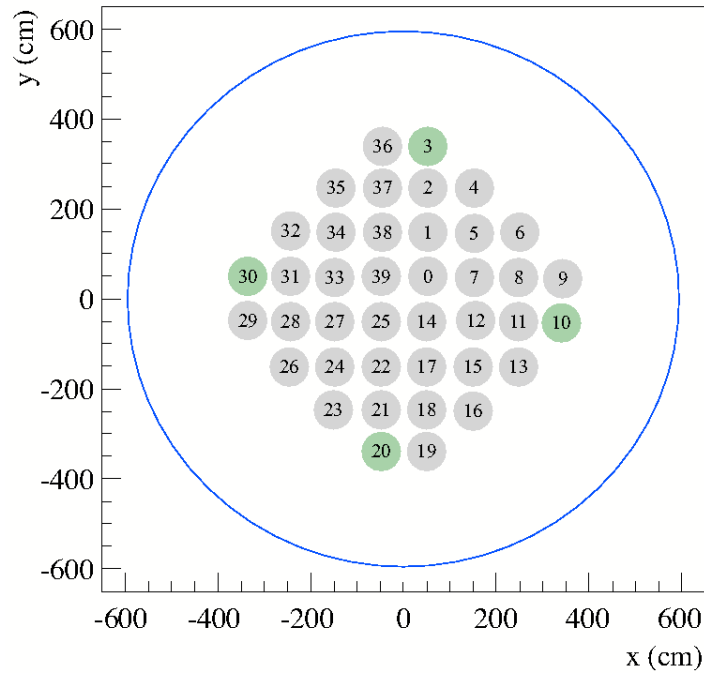


Figure 2.1: Schematic diagram of an NCD string (left). Figure from [28]. A simplified, geometric representation of a typical string is pictured on the right (figure taken from [32]), showing the dimensions of counter ends and middle sections.

Quantity	Value
Gas composition	85 % ^3He , 15 % CF_4
Pressure at 297 K	2.5 atm
Operating temperature	283 K
Gas density	$1.6178 \times 10^{-3} \text{ g cm}^{-3}$
Mean wall thickness	371 μm
Active volume radius, b	2.5421 cm
Anode radius, a	25 μm
Counter lengths	2, 2.5, 3 m
Typical string length	10 m
Delay line length and delay	20 cm, 89 ns
NCD cable length (to preamp)	9 to 12 m, ~ 50 ns transit
Operating voltage	1950 V
Gas gain	219
Total active volume in array	778501 cm^{-3}
Total active NCD length	396 m
Total NCD nickel mass in array	203 kg

Table 2.1: Summary of NCD properties.

Figure 2.2: The NCD array configuration in the AV (blue circle), looking down the detector. ^4He strings are shown in green. NCD diameters are not to scale. Figure from [29].

2.2 Electronics

Fig. 2.3 shows the NCD Data Acquisition (DAQ) system. Each string was connected by means of a 9–12 m-long coaxial cable (resulting in a ~ 50 ns transit time) to a current preamplifier, located in the Deck Clean Room (DCR). The preamplifier linearly converted the NCD current pulse to a voltage signal, with a gain of $27.5 \text{ mV}/\mu\text{A}$. This signal then entered a multiplexer (MUX), located in the SNO control room just outside the DCR. There, it was split in two parts, each of which went through two independently triggered readout systems:

- (1) A fast data path using shaper-ADCs, which measured the total charge of pulses, and, hence, the energy deposited by ionizing particles in the gas.
- (2) A digitizing path that recorded NCD signals as $15 \mu\text{s}$ -long oscilloscope traces, to provide the time profiles of NCD events for analysis.

The shaper-ADC path was capable of recording data at the kHz event rates typical of supernova bursts, up to a maximum rate of 20 kHz. Each signal was integrated in a $6 \mu\text{s}$ time interval. A shaper trigger occurred if the integrated pulse charge exceeded a certain threshold. If so, a dead time of $236 \mu\text{s}$ was imposed on all shaper channels while the event was being recorded.

The digitizing system, on the other hand, had a maximum readout rate of 1.8 Hz, which was adequate for neutrino data-taking³. A ‘MUX trigger’ occurred when the pulse amplitude was above threshold. The pulse itself was made to pass through a 320 ns delay line while the system was being triggered. In the event of a MUX trigger, a vertical offset of around -15 mV was applied to the pulse before it was logarithmically amplified, and sent to an 8-bit oscilloscope for digitization. The reason for adding the offset was to prevent rectification of baseline noise by the log-amplifier. Pulses needed to be log-amplified in order to accommodate the wide dynamic range (~ 145) of amplitudes on the oscilloscopes, while maintaining an acceptable signal-to-noise ratio on the lowest amplitude events. There were two oscilloscopes, each operating at a sampling rate of 1 GHz over $15 \mu\text{s}$. Each oscilloscope had four channels, one for each MUX. The four multiplexers (labelled 1, 4, 5 and 11) were each connected to 10 strings. The dead times

³A total rate of about 0.15 Hz was observed during normal runs.

associated with the MUX hardware and oscilloscopes were estimated to be ~ 600 ns and 0.75 s, respectively.

Every MUX and shaper trigger was time-stamped and assigned a Global Trigger Identification (GTID) number. The NCD electronics was controlled by the Object-oriented Real-time Control and Acquisition (ORCA) program, a data acquisition application developed at the University of Washington [33].

2.3 Calibration

The NCD electronics was calibrated on a weekly basis, with known pulses from a waveform generator injected into the preamplifier (fig. 2.3). Three separate calibration runs tested the linearity of the shaper energy scale, quantified the shaper and MUX trigger thresholds, and measured the parameters describing the logarithmic amplification process for each channel. The ADC bin-to-energy conversion is carried out offline, as follows: ADC bin values are first expressed as ‘calibrated charge’, using conversion factors (a slope and offset) measured in linearity calibrations. Calibrated charge is then converted to energy, by fixing the peak expected from fully-contained p - t tracks to 0.764 MeV (fig. 2.4). Before being analyzed, oscilloscopes traces need to be linearized, *i.e.* the effects of the log-amplifier have to be inverted, using parameters measured in the log-amplifier calibrations.

The neutron capture efficiency and gas gain stability of the array were monitored periodically throughout the NCD phase. Two kinds of high-rate, point neutron sources were used for these purposes: a canned ^{252}Cf source, and a number of AmBe sources. A source manipulator could position the neutron sources at any point in two vertical planes perpendicular to each other. A uniformly distributed neutron source, which mimicked NC neutrons, was also created by mixing activated ^{24}Na into the heavy water. ^{24}Na β -decays to ^{24}Mg with a half-life of 15 hours, emitting 2.75 MeV γ -rays in the process. These γ -rays can photo-disintegrate deuterium, emitting neutrons. The neutron detection efficiency of the NCD array, excluding the six pathological strings, was measured to be 21 %.

2.4 Signals

NCD events can be classified as follows:

- (1) *Ionization events*

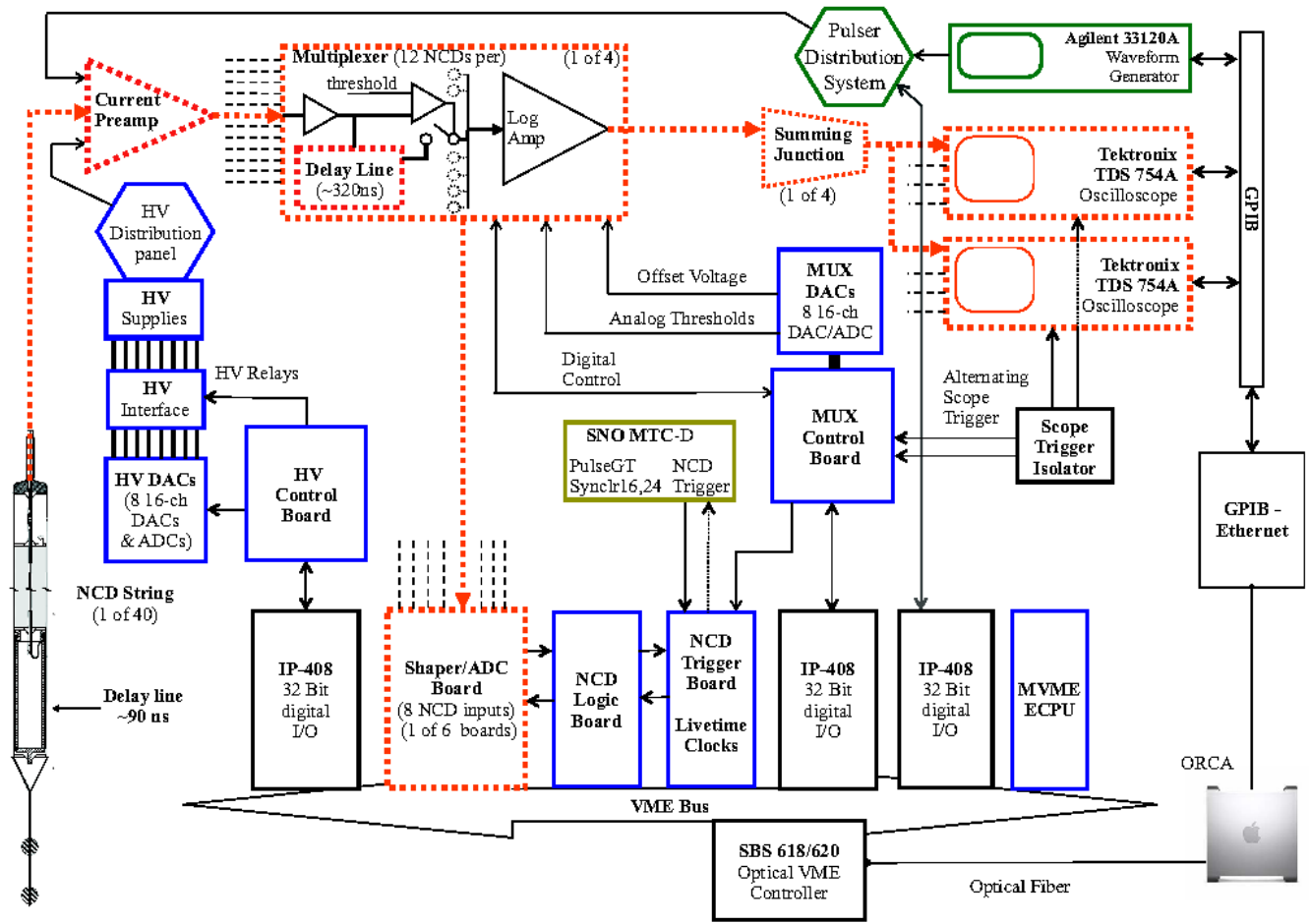


Figure 2.3: The NCD electronics and DAQ system. Figure from [29].

The most common ionizing particles that need to be considered are: p - t pairs emitted in neutron captures, α particles from counter wall and wire impurities, and energetic electrons resulting from β decays and Compton scattered γ -rays. α events are the dominant background in most strings, and come from two main sources: (1) ^{238}U and ^{232}Th chain α decays (see appendix B), and (2) ^{210}Po decays⁴. One can classify α backgrounds according to their origin: (1) *Surface alphas*, which are 5.3 MeV ^{210}Po alphas, (2) *Bulk alphas*, originating from U/Th chain decays within NCD walls, (3) *Wire alphas*, coming from the anode, and (4) *End-effect alphas*, which come from regions of distorted electric field, or from the silica feedthrough. The first two α classes are, by far, the most common. There can be significant differences between these different types of α pulse shapes. All ionization pulses, however, display a slow, decaying tail referred to as the *ion tail*. Ionization backgrounds are ~ 4 times as numerous as neutrons in the neutron energy window (0.2–0.9 MeV).

(2) Instrumental background events

Instrumental backgrounds, which constitute the majority of NCD events, are signals that do not originate from gas ionization, *e.g.* above-threshold thermal noise excursions, discharges, and oscillatory noise. A large number of these can be removed by requiring that all events should trigger both the shaper-ADC and MUX-scope systems within a short time interval ($\sim 10 \mu\text{s}$), resulting in a correlated ‘scope-shaper pair’. Deng and Tolich [34, 35] developed further cuts to eliminate background instrumentals, based on the analysis of oscilloscope traces in both time and frequency domains. All the data analyzed in this thesis are ‘cleaned’, correlated scope-shaper pairs that passed these quality control cuts.

According to SSM predictions, around 13 neutrons per day are expected from NC interactions in the heavy water. Additional neutrons were produced through the photodisintegration of deuterium by ^{238}U and ^{232}Th chain γ -rays with over 2.2 MeV of energy. Trace amounts of U and Th were present in the D_2O , NCD bodies, NCD cables, and light water region. The amounts of U and Th in the D_2O were measured by radio-

⁴The ^{210}Po comes from the plating of Rn daughters on the inner surface of NCD counters during storage. The surfaces were electropolished and acid-etched to mitigate this background. ^{210}Po alphas, however, still constitute around 60 % of all alphas from the array.

assays, as well as *in-situ* techniques⁵. In particular, it was found that two strings (18 and 31) had regions of pronounced radioactivity. The U/Th contents of these ‘hotspots’ have also been measured [36]. Other sources of neutrons include: (α, n) reactions in the AV, $^{17,18}\text{O}(\alpha, n)$ interactions induced by alphas from the counter walls, and atmospheric neutrino interactions.

Example ionization spectra and pulses from the shaper and MUX-scope paths are shown in fig. 2.4. The top row shows energy distributions measured by the shaper-ADCs. The shaper spectrum expected from NC neutrons that are produced uniformly in the AV is on the left. A skewed *neutron peak* at C, with a resolution of ~ 20 keV, results from fully-contained $p-t$ tracks. The flat spectrum from 191 keV to 573 keV consists mainly of events in which the proton runs into the wall. The total NCD array spectrum observed in the 385 live days [37] of data-taking is shown on the right, with a peak at E resulting from ^{210}Po alpha events. The bottom row shows linearized pulses: a neutron event (left), and a high energy α event (right). The MUX trigger occurs at 1500 ns, and the pulse itself starts at ~ 1820 ns. The pre-pulse noise and the oscilloscope baseline offset have been subtracted for clarity.

2.5 Aims and outline of this thesis

The aim of this thesis is twofold:

- (1) To develop a simulation of the NCDs that can model all ionization events from the two data paths (MUX-scope and shaper) as accurately, and efficiently as possible.
- (2) To develop a technique to discriminate between neutrons and ionization backgrounds in NCDs, and, thus, measure the total ^8B solar neutrino flux.

The model should be able to predict spectra and pulses such as those displayed in fig. 2.4, and be accurate enough to answer simple, but important questions such as: what is the shape of the alpha background spectrum in the neutron energy window? Do β events matter? How can pulse shapes be used in extracting the number of neutrons? These, and other issues, will be tackled in this work.

⁵The contaminations of counter bodies could be estimated by studying Cherenkov light emitted by Compton electrons resulting from the photo-disintegration of deuterons by ^{214}Bi or ^{208}Tl γ -rays [36].

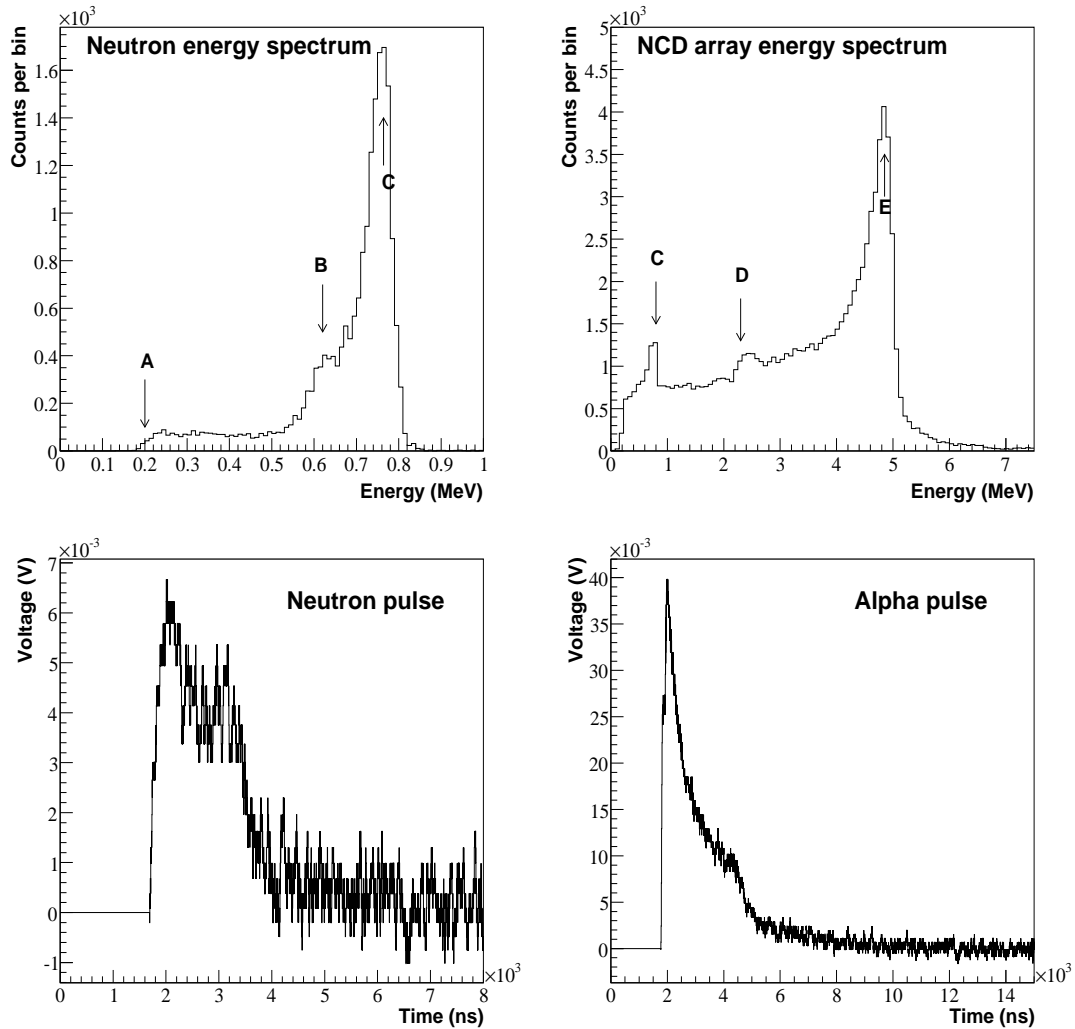


Figure 2.4: Top row: data recorded from the shaper-ADC path. Left: Neutron spectrum from the ^{24}Na calibration source. At A, the proton loses all its energy in the nickel. C is the *neutron peak* arising from fully-contained p - t tracks. Owing to gain loss mechanisms, this peak is skewed towards lower energies, down to B, resulting in a step-shaped feature. Right: accumulated data between 0.2 and 7 MeV, over the 385 live days of the NCD phase. E is the peak resulting from fully-contained 5.3 MeV ^{210}Po alpha tracks, which is skewed to point D. Bottom row: data recorded by the oscilloscopes. Left: an example neutron event. Right: an example alpha event.

An important ingredient in the calculation of pulse shapes is not available experimentally: the radial dependence of electron drift times within NCD counters. Chapter 3 aims to determine this function via a first-principles calculation of the motion of low energy electrons in NCD gas. This electron transport simulation also allows other required quantities, such as avalanche properties and time resolution (due to electron diffusion), to be determined.

The simulation of oscilloscope pulses is the subject of chapter 4. A simple pulse calculation method, applicable to any ionizing particle event, is presented. The various components of the computation (*e.g.* ion transport and trajectories, hardware model) are discussed in detail. Comparisons with neutron calibration data are then made using pulse shape parameter distributions. It is shown that the simulation can be used to identify non-standard alpha events such as wire alphas. Their expected percentages are estimated.

Chapter 5 discusses the calculation of shaper-ADC spectra. It is necessary to have a clear understanding of gain loss mechanisms, and a space charge model is developed. Calculated energy spectra are compared with data, and it is shown that a further piece of information is required: the spatial distribution of impurities in counter walls. Calculated energy pdfs are used to determine the percentage content of each class of background in every NCD string.

In chapter 6, the simulation is used to generate background pulse shape parameter pdfs in a statistical separation of neutrons and alphas, leading to a measurement of the total ^8B solar neutrino flux. The extraction method presented in this thesis makes use, almost exclusively, of pulse shape information.

Chapter 3

Electron Transport in NCDs

All NCD pulse shapes originating from ionization of some sort are considerably influenced by the behaviour of electrons in the 85 % ^3He and 15 % CF_4 mixture. For example, electron drift speeds govern the widths of pulses, since these are mostly determined by the difference between arrival times of the furthest and closest primary electrons. The diffusion of electrons results in a radially dependent smearing effect on all pulses. The ion constant, which is a parameter characterising the tail of pulses, depends on the average ionization radius in an electron cascade close to the anode. Furthermore, the shapes and sizes of these avalanches partly determine the magnitude of space charge effects, which can result in appreciable gain and shape changes. It is therefore clear that accurate electron transport parameters are a critical ingredient in pulse shape calculations.

A Monte Carlo (MC) simulation of electron transport in NCD gas was written with the primary aim of evaluating the mean and RMS drift times of electrons as a function of radius in the counter. The use of the MC method to evaluate gas transport parameters in uniform electric fields is now well established [38, 39], more robust, and involves fewer approximations than typical Boltzmann analyses¹ [40]. Besides the counter geometry and gas state variables, only electron-gas interaction cross-sections are required to solve for electron trajectories. Thus, simulation results are solely dependent on e^- - ^3He and e^- - CF_4 cross-sections for all processes of interest, which are fairly well documented in the literature for the energy ranges required [39, 41, 42].

Existing packages, such as GARFIELD², can perform drift time computations, but

¹These are based on solutions of the Boltzmann equation, which describes the time evolution of particles in fluids.

²GARFIELD is a general purpose wire chamber simulation package from CERN [44].

some discrepancies were observed [43] with the drift measurements of Kopp *et al.* [30] in mixtures of ^3He and CF_4 . GARFIELD loads pre-calculated longitudinal and transverse diffusion constants as a function of electric field from the MAGBOLTZ program, the latest version of which adopts a MC approach [39]. Since these constants are first obtained at constant fields, it is implicitly assumed that the electron equilibrates very rapidly with the gas while moving in the counter. This might not be true, for example: (1) in regions close to the anode, where the field changes very rapidly, and (2) in gases where elastic scattering interactions are dominant over a wide energy range³. By directly propagating electrons in a cylindrical field, one can eliminate such concerns.

Another goal of this work is to study electron multiplication in the vicinity of the wire, to gain insight in the space charge problem. However, NCD gas is a Penning mixture, which means that a significant fraction of all avalanche electrons are a product of CF_4 ionization by, *e.g.* the 2^3S or 2^1S states of ^3He . Measured or calculated cross-sections for these processes are not available, and, hence, they are disregarded throughout the present study. Since ions move very slowly relative to electrons, one can assume that avalanche sizes are not considerably perturbed by Penning ionizations⁴. In other words, the charge distributions computed with the MC presented here should at least be of qualitative value.

This chapter is arranged as follows: in §3.1, an account of the simulation method and algorithm is given. This includes the handling of electrons in both uniform and cylindrical electric fields (§3.1.1), randomization of free times between interactions (§3.1.2) and collision kinematics (§3.1.3, §3.1.4). The software implementation, validation procedure and benchmark results are discussed in §3.2. Finally, the quantities of interest are calculated and discussed in (§3.3), namely drift times and resolution (§3.3.1), as well as avalanche parameters (§3.3.3, §3.3.4).

³For example in argon at room temperature and 1 atm, under a field of 500 Vcm^{-1} , an electron takes several microseconds to reach a stable drift velocity value, because the average energy loss in collisions is very small (§3.2.1).

⁴A Penning ionization is the ionization of a molecule M_1 by another atom, or molecule M_2^* , in an excited state. This excited state energy should be higher than the first ionization energy of M_1 .

3.1 Simulation method

3.1.1 Difference equations

The motion of electrons in the presence of an electric field, \mathcal{E} , without any interactions with matter, is first solved numerically. To a very good approximation, non-relativistic physics applies at all relevant kinetic energies E (0–50 eV). One can also safely assume that an electron interacts with one atom at a time. In a uniform field, Cartesian coordinates with the z -axis antiparallel to the field direction are adopted. Let (x_i, y_i, z_i) be the position at some time t_i . Then, after a time step Δt , the new coordinates $(x_{i+1}, y_{i+1}, z_{i+1})$ are given by:

$$\begin{aligned} z_{i+1} &= z_i + \dot{z}_i \Delta t - \frac{e\mathcal{E}\Delta t^2}{2m_e} & , & \quad \dot{z}_{i+1} = \dot{z}_i - \frac{e\mathcal{E}\Delta t}{m_e} \\ y_{i+1} &= y_i + \dot{y}_i \Delta t & , & \quad \dot{y}_{i+1} = \dot{y}_i \\ x_{i+1} &= x_i + \dot{x}_i \Delta t & , & \quad \dot{x}_{i+1} = \dot{x}_i \\ E_{i+1} &= E_i - e\mathcal{E}(z_{i+1} - z_i) & , & \quad \theta_{i+1} = \cos^{-1} \left(\frac{\dot{z}_{i+1}}{\sqrt{2E_{i+1}/m_e}} \right) \end{aligned} \quad (3.1)$$

where m_e is the mass of the electron, e the electron charge and θ the electron trajectory with respect to the z -axis.

Similarly, under the influence of a cylindrical field $\mathcal{E} = \frac{V}{r \ln(b/a)}$ and in the absence of any collisions, the electron trajectory is solved by the following difference equations:

$$\begin{aligned} r_{i+1} &= r_i + \dot{r}_i \Delta t + \frac{e\mathcal{E}(r_i)\Delta t^2}{2m_e} & , & \quad \dot{r}_{i+1} = \dot{r}_i + \frac{e\mathcal{E}(r_i)\Delta t}{m_e} \\ E_{i+1} &= E_i + eV \frac{\ln(r_{i+1}/r_i)}{\ln(b/a)} & , & \quad \dot{\phi}_{i+1} = \frac{\dot{\phi}_i r_i}{r_{i+1}} \\ \alpha_{i+1} &= \cos^{-1} \left(\frac{\dot{r}_{i+1}}{\sqrt{\dot{r}_{i+1}^2 + \dot{\phi}_{i+1}^2}} \right) & , & \quad \phi_{i+1} = \phi_i \pm \frac{\cos^{-1}(r_{i+1}^2 + r_i^2 - \Delta l^2)}{2r_{i+1}r_i} \end{aligned} \quad (3.2)$$

where b is the radius of the counter and a the radius of the wire, V the anode voltage, and the variables r , ϕ , α and Δl are shown in fig. 3.1. θ is given as in the uniform field case.

Energy and angular momentum conservation are enforced throughout the simulation. To ensure computational accuracy, Δt is constrained by the following conditions:(1) The change in electric field along the distance travelled in Δt is always less than 0.5 %

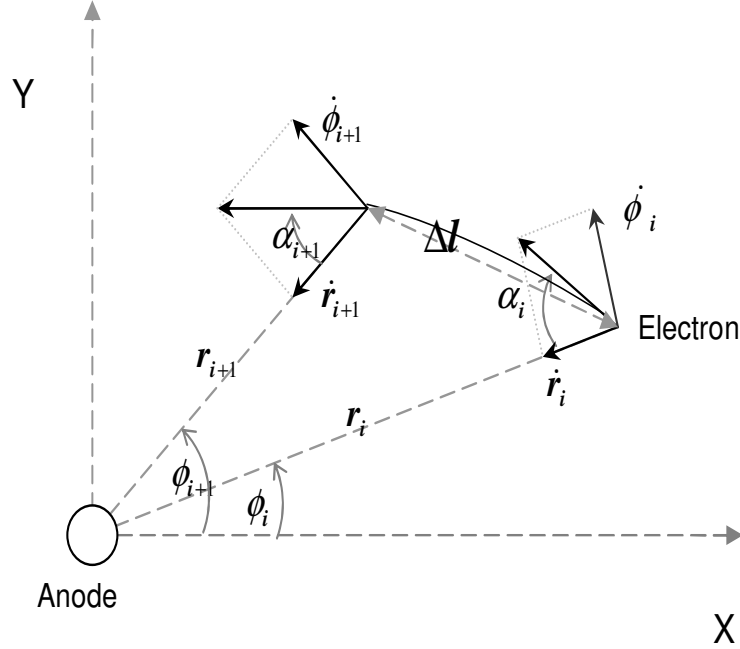


Figure 3.1: The collision-less path of an electron moving under a cylindrical electric field during a time step Δt , and the variables used to describe it. The z -axis points out of the paper.

(*i.e.* the field and the force acting on the electron are approximately constant), which also simplifies the difference equations considerably. (2) In the presence of a gas, at a specific energy or speed v , the *average* value of Δt should be less than the mean free time between interactions (*i.e.* $v\overline{\Delta t}$ is the mean free path between collisions). The procedure for choosing a random time step satisfying the second requirement is based on a technique commonly used in plasma physics, as discussed in the next section.

3.1.2 Null collision technique

Just as for thermalized neutrons, the stochastic choice of an electron free time Δt is straightforward if the mean collision frequency ν or mean free time τ were constant at all times. In the latter case, the probability P of a collision occurring in a time interval t is $P = 1 - e^{-\frac{t}{\tau}}$, so that $\Delta t = -\nu^{-1}\ln R$, where R is a random number between 0 and 1. However, if the speed (and, hence, the collision frequency) changes under the influence of an electric field, the expression for P becomes more complicated and the direct generation of a random set of free times is very difficult. To overcome this problem, Skullerud [45]

devised the null collision technique, in which an artificial constant frequency $\nu' > \nu$ is assumed in the calculations. Therefore, the free time between interactions is randomized in the same fashion as above, while the type of collision (real or null) is decided by another random number. A null collision is a ‘fake’ interaction, in which the state of the electron is completely unchanged.

In this work, a more efficient version first proposed by Lin and Bardsley [46] is implemented, and slightly extended for gas mixtures. Unlike Skullerud’s method, in which any $\nu' > \nu$ is applicable, Lin and Bardsley’s formalism fixes the choice of ν' and saves computation time. The total rate of collisions ν' , is the sum of real and null collisions:

$$\nu' = \nu_{\text{Real}} + \nu_{\text{Null}} \quad (3.3)$$

If ν' is set to K , the maximum collision rate over the energy range of interest, this can be rewritten in terms of cross-sections as

$$\frac{K}{v} = \sigma_{\text{Real}}(E) + \sigma_{\text{Null}}(E) \quad (3.4)$$

where $\sigma_{\text{Real}}(E)$ the total real cross-section, and v the electron speed. Hence, the time between interactions is again exponentially distributed with a mean free time $\tau = (N_e K)^{-1}$ where N_e is the gas number density. After travelling a randomly selected time step Δt under the influence of a field, the collision type is now determined by the ratio

$$\frac{\sigma_{\text{Real}}(E)}{\sigma_{\text{Real}}(E) + \sigma_{\text{Null}}(E)} \quad (3.5)$$

For a mixture of n gases, Eq. 3.5 becomes

$$\frac{K}{v} = f_1 \sigma_{\text{Real},1}(E) + f_2 \sigma_{\text{Real},2}(E) + \dots + f_n \sigma_{\text{Real},n}(E) + \sigma_{\text{Null}}(E) \quad (3.6)$$

where f_1, f_2 , etc are the proportions of each component by partial pressure (or number density). The free time is randomized as for pure gases. However, before choosing the interaction type, the target species has to be picked randomly by taking into account the ratios of collision rates expected from each gas component at a given energy.

In the event of a null collision, the state of the electron is left unchanged and the next interaction is considered. On the other hand, if the collision is real, the interaction type (elastic, ionization, excitation, etc) is selected, based on the cross-section for each process. The velocity and energy of the electron are then modified accordingly, as described in the next section.

3.1.3 Kinematics of isotropic collisions

All relevant interactions of electrons in NCD gas can be grouped into four types: elastic collisions, inelastic collisions that do not result in additional electrons (such as excitations and vibrations), ionizations and electron attachment. The probability of photonic processes, such as bremsstrahlung, is very small and, furthermore, elastic scattering with any free electron is neglected⁵. In this section, electron kinematic variables are determined after each type of interaction.

After an isotropic elastic scatter, the new velocity vector \mathbf{v}' is found in the centre of mass frame and transformed back to the laboratory frame. Let ψ' be the angle between v' and the pre-collision direction $\hat{\mathbf{n}}$, and η' the angle specifying \mathbf{v}' in a plane perpendicular to $\hat{\mathbf{n}}$. ψ' and η' are generated using two random numbers R_1 and R_2 by

$$\psi' = \cos^{-1}(1 - 2R_1) \quad , \quad \eta' = 2R_2\pi \quad (3.7)$$

With ψ' at hand, the electron energy E' after the elastic collision is given by the textbook equation [47]

$$E' = E \left[1 - \frac{2m_e M}{(m_e + M)^2} (1 - \cos \psi') \right] \quad (3.8)$$

where M is the target mass. Then the corresponding angles in the the lab frame are

$$\sin \psi = \frac{M}{M + m_e} \left(\frac{E}{E'} \right)^{\frac{1}{2}} \sin \psi' \quad , \quad \eta = \eta' \quad (3.9)$$

Backscattering occurs in the lab frame if

$$|\mathbf{v}|^2 < |\mathbf{v}'|^2 - |\mathbf{V}|^2 \quad (3.10)$$

where \mathbf{V} is the centre of mass velocity and \mathbf{v} the electron velocity in the lab frame after collision. When $|\mathbf{V}| > |\mathbf{v}|$, forward scattering is always observed in the lab frame, even if backscattering takes place in the centre of mass frame.

Isotropic inelastic collisions are treated in the same way as elastic ones, except that the final electron energy is given by [38]

$$E' = E \left[1 - \frac{M}{M + m_e} \left(\frac{\epsilon}{E} \right) + \frac{2Mm_e}{(M + m_e)^2} \left(\left\{ 1 - \frac{M + m_e}{M} \left(\frac{\epsilon}{E} \right) \right\}^{\frac{1}{2}} \cos \psi' - 1 \right) \right] \quad (3.11)$$

⁵All free electrons drift towards the wire.

with ϵ being the threshold energy for the interaction. The scattered angles in the lab frame are now

$$\sin \psi = \frac{M}{M + m_e} \left(\frac{\epsilon}{E} \right)^{\frac{1}{2}} \left[1 - \frac{M + m_e}{M} \left(\frac{\epsilon}{E} \right) \right]^{\frac{1}{2}} \sin \psi' \quad , \quad \eta = \eta' \quad (3.12)$$

When an ionization occurs, an energy $E - \epsilon$ is shared randomly between the two resulting electrons. If an electron becomes attached to a target, its evolution is terminated immediately and the next electron is considered.

3.1.4 Anisotropic collisions

Due to the scarcity of differential cross-section data, anisotropic collisions are treated using Longo and Capitelli's [48] prescription, as suggested in [39]. In their paper, they derive the forward scattering probability P_f in terms of the total and momentum transfer cross-sections (σ_T and σ_{MT} respectively) for the process in question:

$$P_f = \frac{1}{2} + \frac{\sigma_T - \sigma_{MT}}{\sigma_T} \quad (3.13)$$

Momentum transfer cross-sections are usually more readily available in the literature. Once forward or backward scatter is chosen, the electron direction is picked at random assuming an isotropic angular distribution in the hemisphere in question.

3.2 Implementation and benchmarking

A simplified flow diagram summarizing the code structure, and sequence of calculations discussed in the previous sections, is shown in fig. 3.2. The electron is evolved for a free flight time Δt , as explained in §3.1, and it is then decided whether or not a true interaction occurs (§3.1.2). If so, the type of collision is chosen, and the particle's variables modified (§3.1.3). If not, they are left unchanged, and the next time step considered. The process is repeated until some criterion imposed by the user is met.

To test the code efficiently, motion under a constant electric field is simulated, then compared with measurements in gases of increasing complexity: pure Ar, CH₄ (at energies below 10 eV), ⁴He and CF₄, and mixtures of ³He and CF₄. The first two gases are picked for reasons described below, but also because of the wealth of experiments on the subject given the widespread use of P-10 gas⁶. The transport parameter used in comparisons is

⁶P-10 gas is a mixture of 90 % Ar and 10 % CH₄.

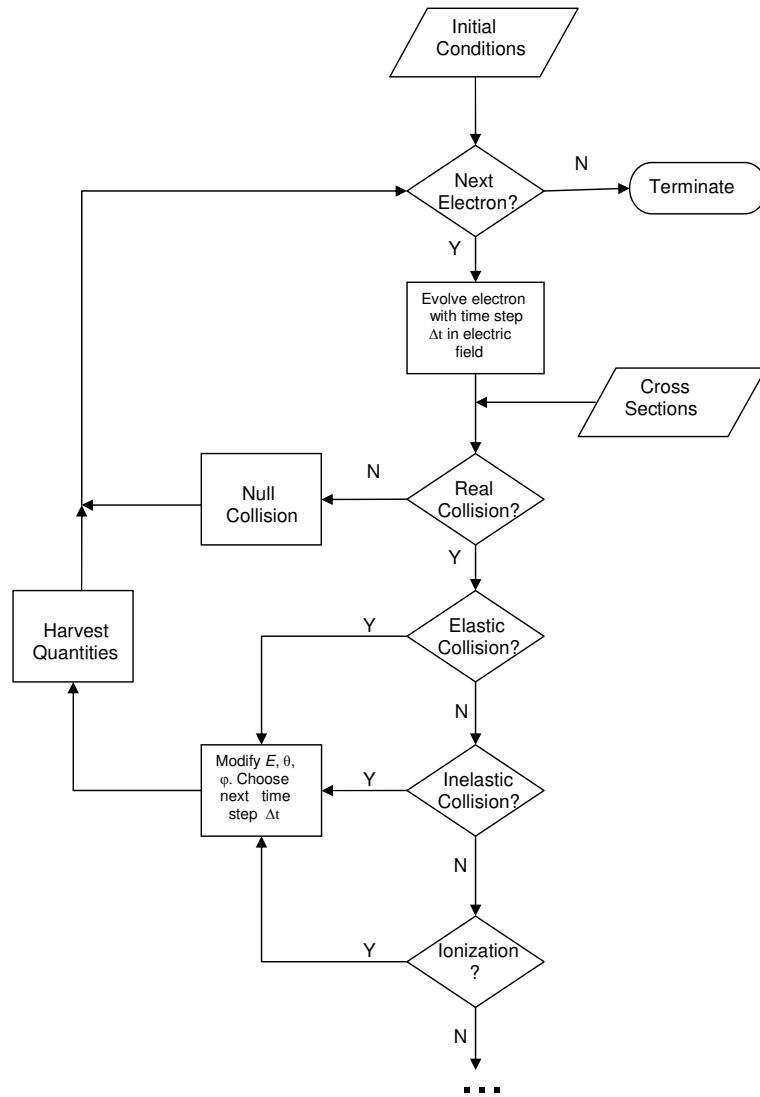


Figure 3.2: Simplified flow diagram for the electron transport code.

the electron drift speed as a function of field strength. Assuming statistical ergodicity⁷, this quantity is conveniently extracted from the asymptotic value of z/t by following a *single* electron in the simulation. Depending on the gas, this can be a time-consuming process since it can take up to 10^7 collisions before steady state is reached. The electron coordinates, direction and energy are recorded every 100 collisions. A temperature of 293 K and a pressure of 760 torr (*i.e.* the same gas density) are applied in all tests. It was verified that results are not dependent on initial positions and directions. Suitable values of K (§3.1.2) evaluated for the different gases, together with the maximum number of real collisions probed before the simulation is stopped, are shown in table 3.1. Cross sections were obtained from [42]. These are assumed to be identical for ^4He and ^3He in this work.

Gas	$K \times 10^{20} (\text{m}^3\text{s}^{-1})$	Max. collisions
Ar	3.32×10^7	1×10^7
CH_4	4.73×10^7	1×10^6
^4He	8.97×10^6	5×10^6
CF_4	7.41×10^7	1×10^6
80:20 ($^3\text{He}:\text{CF}_4$)	1.65×10^7	1×10^6
90:10 ($^3\text{He}:\text{CF}_4$)	3.03×10^7	1×10^6

Table 3.1: Values of K applied in the null collision algorithm for each gas, and the number of real collisions simulated until termination. Ar and ^4He converge slower, because elastic scattering is the dominant interaction below 10 eV in both gases.

3.2.1 Drift speeds at constant fields

Argon is an ideal specimen for ‘calibrating’ basic components of the MC, such as propagation and null collision algorithms, with the simplest interaction: elastic scattering. This interaction is the dominant one below 10 eV. In analogy to CF_4 , the Ar cross-section has a minimum⁸ at ~ 0.2 eV (fig. 3.3). Fig. 3.3 (right) shows the Ar drift speed calculation up to $\mathcal{E} = 800 \text{ Vcm}^{-1}$ compared with measurements. Beyond 800 Vcm^{-1} the electron energy can exceed 10 eV, and inelastic processes must be considered. The jaggedness of the simulated curve arises because the drift speed has not yet reached a stable value

⁷The electron-gas system is ergodic if, at equilibrium, the distribution of drift speeds from an ensemble of electrons at one point in time is equivalent to the drift distribution from only one electron, sampled at different points in time.

⁸Commonly called ‘*Ramsauer minimum*’.

when the simulation was stopped. From Eq. 3.8, the maximum fractional energy loss in an elastic collision with an Ar atom is only $\sim 7 \times 10^{-3} \%$, which means that convergence to an equilibrium drift speed is slow.

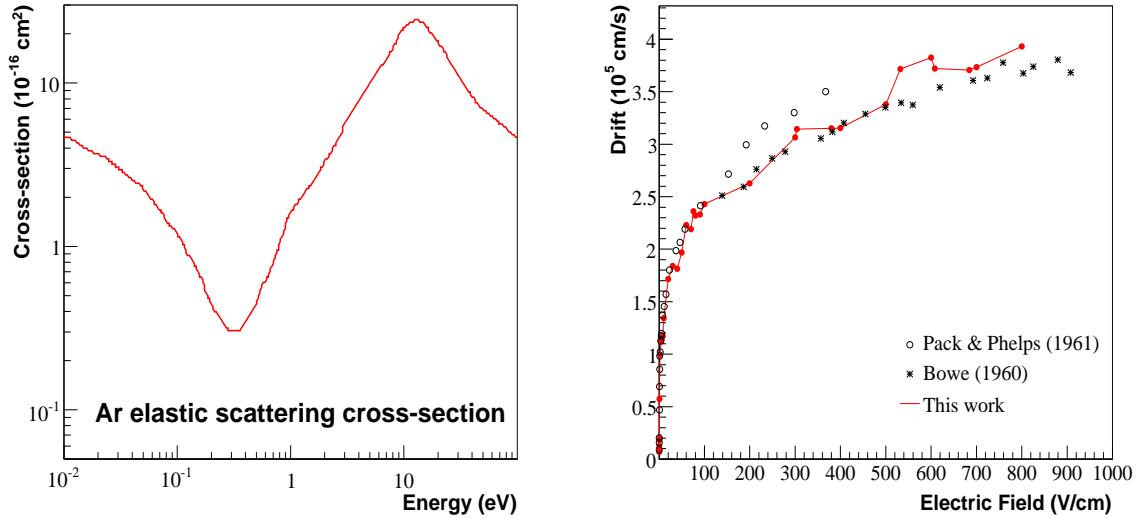


Figure 3.3: Left: Ar- e^- cross-section (elastic) from [42]. Right: Calculated drift speed in Ar compared with data from Pack and Phelps [49] and Bowe [50].

The implementation of more complex inelastic interactions is verified with CH_4 , which has two vibrational channels below 10 eV in addition to an elastic channel that also displays a Ramsauer dip (fig. 3.4). As opposed to Ar, convergence in this gas is much faster and the drift speed calculation agree well with Yoshida's data [51]. It is noted that all collision processes were assumed to be isotropic in CH_4 .

In NCD counters, the maximum and minimum electric fields are about $1.1 \times 10^5 \text{ Vcm}^{-1}$ and $1 \times 10^2 \text{ Vcm}^{-1}$, respectively. Computations in ^4He (fig. 3.5) are in very good agreement with data [30, 52] in the low field region of most relevance. At $1 \times 10^4 \text{ Vcm}^{-1}$ there seems to be as much as 10 % disagreement, but this corresponds to a radius of just $\sim 10a$, which is $\sim 1 \%$ of the counter radius. Therefore, the impact on drift times is negligible. Pure CF_4 results are shown in fig. 3.6, when the strongest vibrational inelastic channel (magenta curve) is treated both isotropically and anisotropically using the prescription in §3.1.4. There are sizeable changes in the drift curves, with the anisotropic case predicting higher velocities because of a higher probability of forward scattering, Eq. 3.13. Agreement with GARFIELD is good because the same cross-sections are used

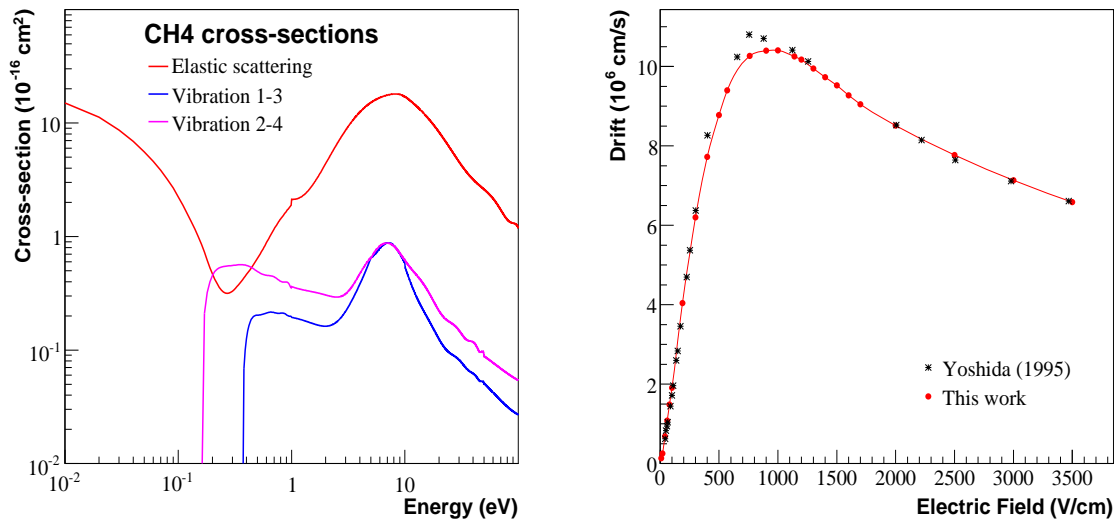


Figure 3.4: Left: $\text{CH}_4\text{-e}^-$ cross-sections from [42]. Right: Calculated drift speed in CH_4 compared with data from Yoshida [51].

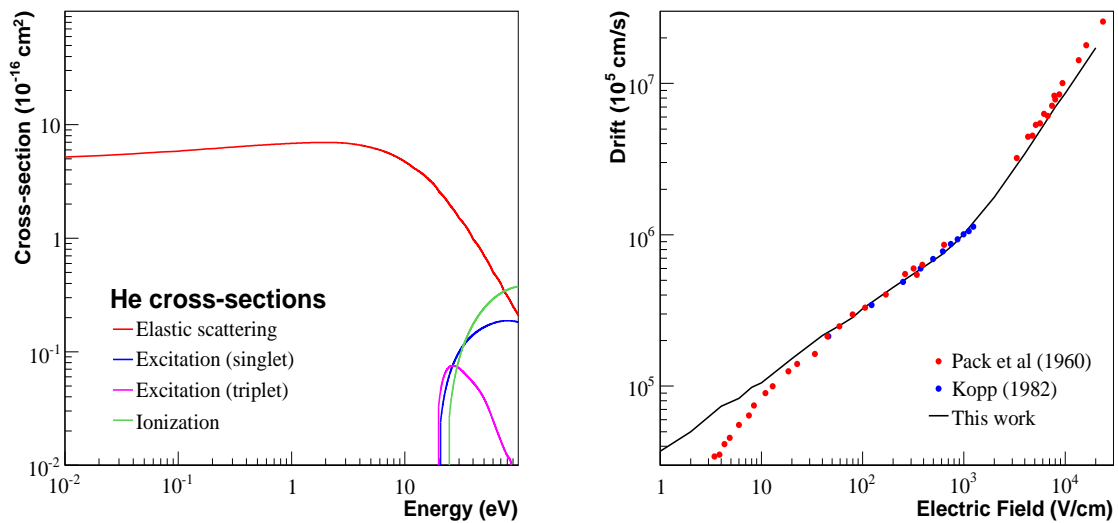


Figure 3.5: Left: Helium- e^- cross-sections from [42]. Right: Calculated drift speed in ^3He compared with data from Kopp [30] and Pack *et al.* [52].

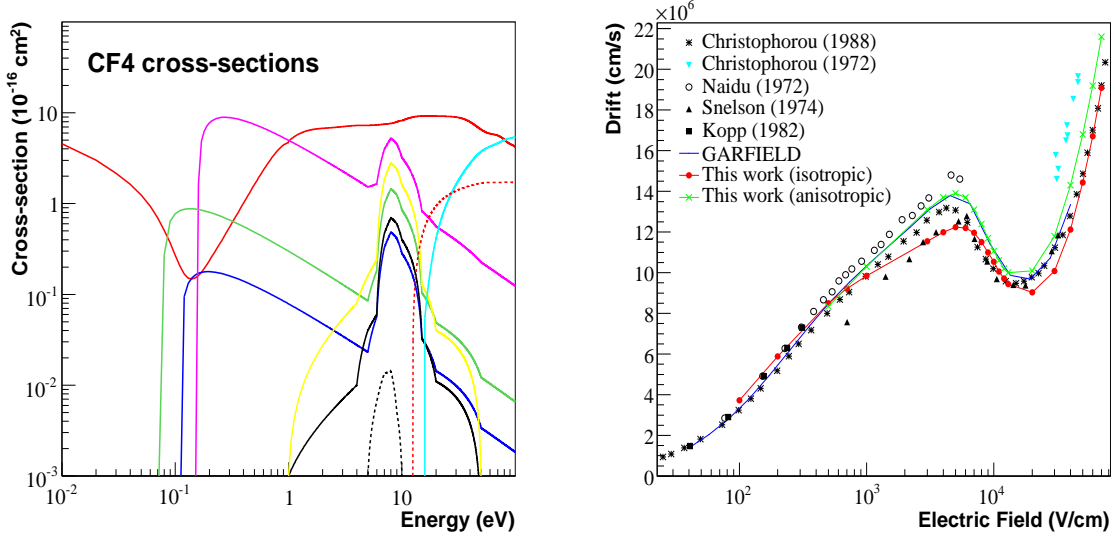


Figure 3.6: Left: $\text{CF}_4\text{-e}^-$ cross-sections [42]. Red: elastic; blue, green and magenta: vibrational; black and yellow: vibrational (harmonics); black dotted: attachment; red dotted: excitation; cyan: ionization. Right: Calculated drift speed in CF_4 compared with data from Christophorou [53, 54], Kopp [30], Naidu [55] and Snelson [56].

by MAGBOLTZ; both simulations appear to be consistent with data [30, 53, 54, 55, 56].

Calculations for 80:20 and 90:10 ($^3\text{He}:\text{CF}_4$) mixtures are displayed in fig. 3.7. In the 90:10 case, discrepancies of about 15 % at moderate electric fields ($1400\text{--}1600 \text{ Vcm}^{-1}$) are seen between two separate measurements [30, 54]. From this figure, it is observed that experimental uncertainties are of the order of $\pm 7\%$, although neither of the two papers quote any errors. The MC is consistent with both data sets, but also seems to be at variance by $\sim 15\%$ with [30] at similar field values in 80:20. No other independent drift measurements were found in the literature for this particular gas mixture. If one assumes crudely that experimental uncertainties in the 80:20 and 90:10 measurements from [30] are of the same magnitude (7 %), then it appears that data and the anisotropic MC differ by up to $\sim 2\text{-}\sigma$ at $2 \times 10^3 \text{ Vcm}^{-1}$ in fig. 3.7. However, good agreement is obtained with GARFIELD in 80:20, as in the pure CF_4 case.

3.2.2 Diffusion coefficients in ^4He and CF_4 at constant fields

Fick's first law of diffusion states that the diffusive flux of electrons, \mathbf{j}_e , is directly proportional to the electron concentration gradient:

$$\mathbf{j}_e = -D_e \cdot \nabla N_e \quad (3.14)$$

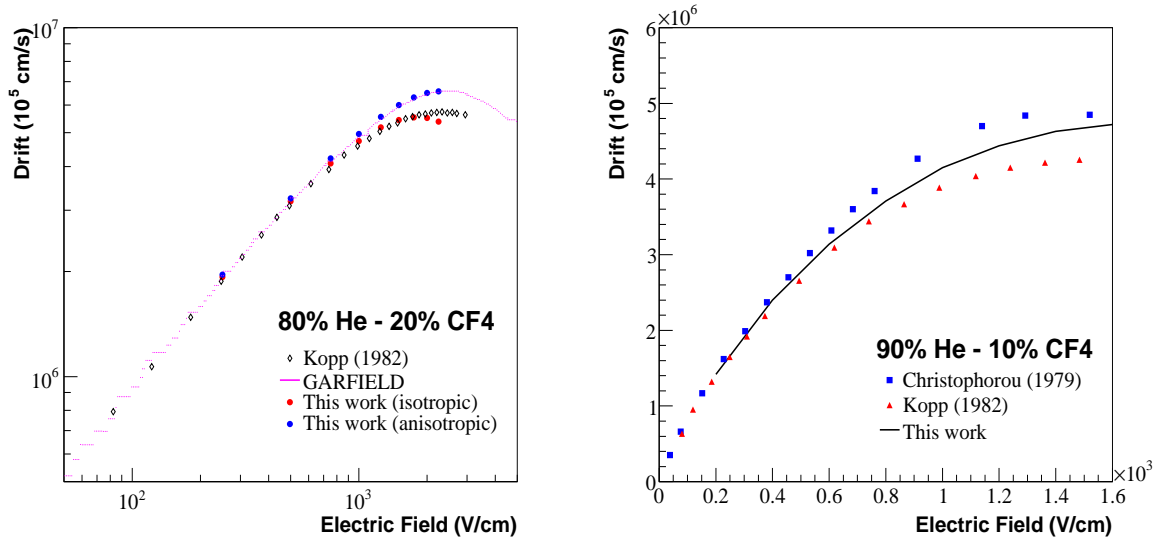


Figure 3.7: Left: Calculated drift speed in 80:20 (³He:CF₄) compared with GARFIELD and data from Kopp [30]. Right: Calculated drift speed in 90:10 (³He:CF₄) compared with data from Kopp [30] and Christophorou [54]. The two measurements differ by up to ~15 %. Uncertainties on the measurements were not reported.

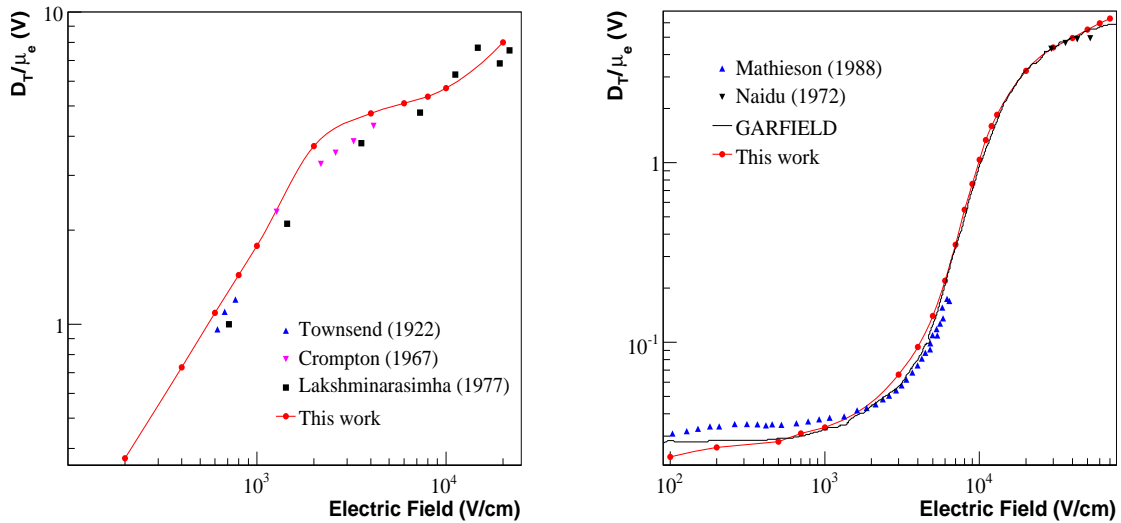


Figure 3.8: Right: D_T/μ_e in CF₄; data from [55, 57] and GARFIELD calculation from [39]. Left: D_T/μ_e in ⁴He; data from [58, 59, 60].

where D_e is the diffusion coefficient. In a plane perpendicular to \mathcal{E} , one can define a transverse diffusion coefficient D_T . The ratio $\frac{D_T}{\mu_e}$, where μ_e is the electron mobility⁹, is a commonly measured electron transport parameter. In analogy to drift speed calculations, D_T can also be evaluated at equilibrium, assuming ergodicity. If electron coordinates are sampled every n real collisions, D_T is given by the mean square distance of the electron in a plane perpendicular to the z -axis [38], which is antiparallel to the field direction:

$$D_T = \frac{1}{N_s} \sum_{i=1}^{N_s} \frac{(x_{i+1} - x_i)^2 + (y_{i+1} - y_i)^2}{4(t_{i+1} - t_i)} \quad (3.15)$$

In the above equation, i loops through each sample, N_s is the total number of samples and a value of $n = 100$ was adopted.

Fig. 3.8 shows calculations of $\frac{D_T}{\mu_e}$ at different field values, compared with data for the components of NCD gas. The MC reproduces the field dependence observed in the data, and agrees with the GARFIELD D_T result from [39].

3.3 Results

The series of tests discussed in §3.2.1 and §3.2.2 showed that MC calculations of drift speeds in the benchmark pure gases are consistent with data. The divergence at high fields in pure ^4He is not expected to affect drift time calculations. Concerning He-CF₄ mixtures, the MC is in good agreement with the 90:10 data, but differs from the 80:20 data by as much as $2\text{-}\sigma$ at some field values. However, there is very good agreement with GARFIELD.

In this section, the MC is used to compute electron transport parameters for pulse shape simulations (operating conditions are satisfied: cylindrical electric field, and a 85:15 mixture with the correct gas density). These are: the mean and RMS drift time of electrons as a function of radius (§3.3.1), and electron avalanche properties (§3.3.3 and §3.3.4).

3.3.1 Drift and time resolution in NCD counters

To calculate the mean drift time t_d and resolution $\sigma(t_d)$ due to diffusion as a function of radius, a large number of electrons are started at different radii (but same z position) in

⁹Mobility is defined as the drift speed to field ratio.

the counter. The arrival times for each position are Gaussian distributed, as expected from the Central Limit Theorem. The average is shown in fig. 3.9, and the standard deviation in fig. 3.11. GARFIELD results from [61] are included for comparison.

A fourth order polynomial fit to t_d was implemented in pulse calculations:

$$t_d = 121.3r + 493.9r^2 - 36.71r^3 + 3.898r^4 \quad (3.16)$$

with t_d in ns and r in cm. To check the consistency with existing drift measurements in He-CF₄ mixtures, data from Kopp *et al.*¹⁰ [30] was cubic-spline interpolated to produce a drift speed vs electric field curve for 85:15 mixtures. Assuming a crude, uniform experimental uncertainty of $\pm 10\%$ at all field values, the interpolated $\frac{dr}{dt}$ curve was then integrated to generate $1\text{-}\sigma$ and $2\text{-}\sigma$ allowed regions in t_d vs r space. The two regions are shown in cyan ($1\text{-}\sigma$) and green ($2\text{-}\sigma$) in fig. 3.9. Therefore, it appears that the MC is consistent with [30] if the measurements are accurate within $\pm 20\%$. This is not unreasonable, considering the discrepancy with [54], in 90:10 (§3.2.1).

As seen in fig. 3.9, the experimentally-allowed areas in t_d vs r space are rather broad. These regions can be constrained by examining alpha pulses from the counters. Fig. 3.10 shows *pw30*, the 30% amplitude width (defined in appendix D) of NCD pulses from the whole array, recorded during neutrino data-taking, between 0.2 and 6 MeV (left), and in the energy range 0.9–1.2 MeV (right). The widest recorded pulses were found to have a mean width at 30% pulse amplitude of ~ 3500 ns. These are wire alpha particle tracks that hit counter walls and have a radial extent of 2.54 cm. The drift curve passing through ($r = 2.54, t_d = 3500$) is shown as a dotted line in fig. 3.9. Because no wider physics events were observed, the t_d - r region above that line is excluded.

Another constraint can be obtained from the 5.3 MeV ²¹⁰Po alphas originating from the inner surface of the NCD walls. The maximum radial length of ²¹⁰Po alphas that deposit between 0.9–1.2 MeV in the counter is, on average, 0.12 cm [62], corresponding to an observed *pw30* of ~ 400 ns: ²¹⁰Po pulses appear as the dark lower band in fig. 3.10 (right). Therefore, if one allows for a broadening of ~ 100 ns by pulse reflection¹¹, the time difference between drift times of electrons starting at 2.54 cm and 2.42 cm cannot exceed

¹⁰Kopp *et al.* measured the drift speeds of electrons, as a function of electric field, in various He-CF₄ mixtures (but not at 85:15).

¹¹This is a conservative estimate, since the maximum separation between direct and reflected pulses in the shortest NCD string is about 160 ns.

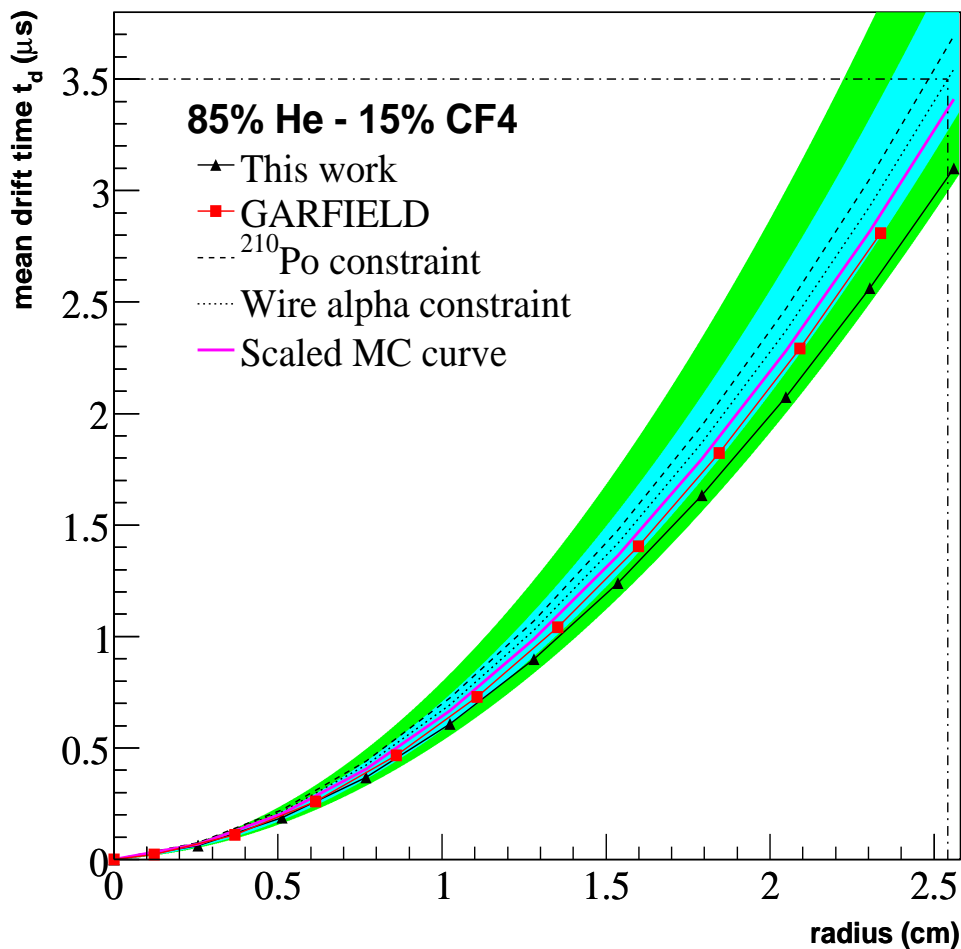


Figure 3.9: Mean electron drift time in NCDS as a function of radius. The cyan region is the set of possible curves, assuming that the 85:15 drift-field relation extracted from [30] has an uncertainty of $\pm 10\%$, while green and cyan combined assumes $\pm 20\%$. Regions above the dotted curve are disfavoured by wire α pulses, which require $t_d(r = 2.54 \text{ cm}) < 3500 \text{ ns}$ (denoted by the dash-dotted lines; see text). The dashed curve is a weaker constraint from low energy ^{210}Po events, and the purple curve is the actual function adopted in pulse simulations. GARFIELD calculations (red) kindly provided by [61].

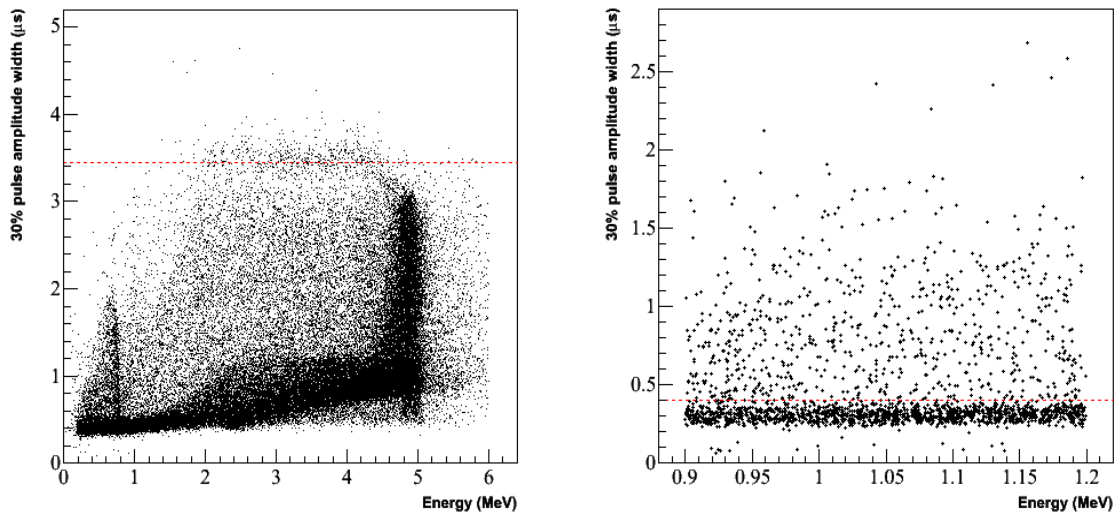


Figure 3.10: Left: Scatter plot showing the width of pulses at 30 % amplitude as a function of energy. The band with a mean of 3451 ns (red dotted line) results from wire alphas. Right: The FWHM of ^{210}Po pulses in the range 0.9–1.2 MeV does not exceed 400 ns (red dotted line).

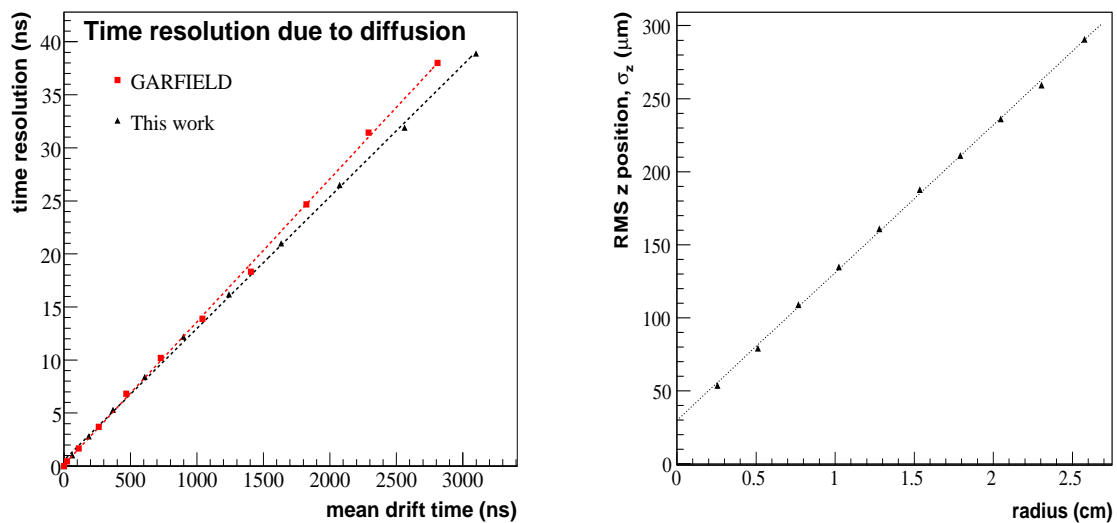


Figure 3.11: Left: The time resolution contributed by electron diffusion is linearly related to the average drift time. GARFIELD calculations kindly provided by [61]. Right: The z distribution of electrons collected at the wire in a single avalanche is Gaussian with an RMS that is linearly related to the starting radius.

300 ns. It is, on the other hand, very likely to be less than 300 ns, because pulses are significantly smeared and broadened by diffusion and electronics. The MC curve obtained in the present work was scaled, such that $t_d(r = 2.54 \text{ cm}) - t_d(r = 2.42 \text{ cm}) = 300 \text{ ns}$ is satisfied. This is shown as a dashed curve in fig. 3.9, and is a weaker constraint than the dotted function. One can, thus, state that SNO data restricts $t_d(r)$ curves to the region below the dotted line in fig. 3.9.

The RMS drift time (in ns) is linearly related to the mean drift (also in ns) as follows (fig. 3.11):

$$\sigma(t_d) = 0.0124t_d + 0.559 \quad (3.17)$$

The spread in electron arrival times implies that all ionization pulses are smeared in time. Since it is caused by the diffusion of electrons, this time resolution worsens with increasing radius. The implementation of other time smearing effects on pulses will be discussed in subsequent chapters.

Differences between this work and GARFIELD values in figs. 3.9 and 3.11 give an estimate of the size of the systematic error associated with the calculations: about $\pm 3 \%$ for t_d and $\pm 4 \%$ for $\sigma(t_d)$. Comparisons, with GARFIELD, of quantities evaluated at constant electric fields (figs. 3.6, 3.7 & 3.8) demonstrate very good agreement. Nevertheless, as pointed out at the beginning of this chapter, the motion of electrons in a cylindrical field is handled differently by the two programs. GARFIELD uses on diffusion constants and drift speeds pre-computed at constant fields values, while a direct propagation is attempted here. This is suspected to be the source of the discrepancy. A more complete estimation of systematic errors, which is not attempted here, requires the cross-sections for each process (figs. 3.5 & 3.6) to be varied within their error bars.

3.3.2 Corrected drift curve

The MC-calculated drift curve (Eq. 3.16) was initially used in pulse shape calculations. However, comparisons of simulated pulse width pdfs with data reveal biases resulting from MC pulses being too narrow. These differences might be due to a number of pulse-broadening mechanisms that are not related to e^- transport. Nevertheless, a scaling factor of $+10 \%$, obtained through studies of wire alphas, was used to scale Eq. 3.16 to account for the discrepancies. Wire alphas calculated using this scaling factor are shown in red in fig. 3.12, with the data (black) peaking at about $3450 \pm 140 \text{ ns}$. Assuming pulse widths

to be directly proportional to drift times, and given that the unscaled distribution (blue) peaks at 3150 ns, the uncertainty on the scaling factor is $\pm 4\%$. The purple function in fig. 3.9 is the final, corrected drift curve used in pulse simulations.

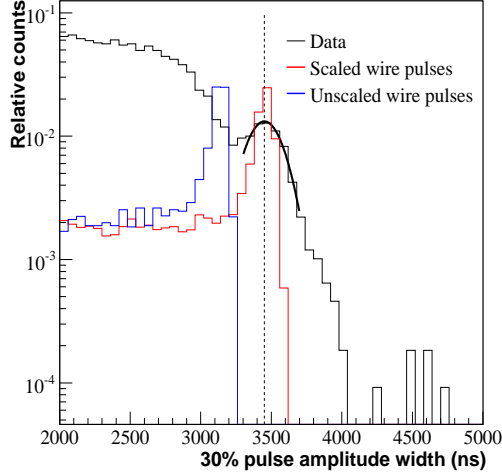


Figure 3.12: Projection of fig. 3.10 on the vertical axis (black) showing a mean maximum wire alpha width of 3500 ns. Wire pulses calculated with the unscaled drift curve (Eq. 3.16) result in the blue pdf. Eq. 3.16 is scaled by (+10 %) to match the peak in the data (red pdf).

3.3.3 z resolution

Because of diffusion, an electron starting at $z = z_0$ is collected at the wire at z_0 on average only. The z distribution at the anode is also observed to be Gaussian, with an RMS σ_z that varies linearly with the starting radius (fig. 3.11). At any r , σ_z can be decomposed into two components:

$$\sigma_z^2(r) = \sigma_{av}^2 + \sigma_{diff}^2(r) \quad (3.18)$$

where σ_{diff} is contributed by transverse diffusion, and carries the radial dependence entirely. σ_{av} has the same value at all r , and is the mean spread of an electron avalanche along z . A linear fit to $\sigma_z(r)$ gives $\sigma_{av} = 29.9 \pm 0.7 \mu\text{m}$, since $\sigma_{diff} = 0$ at $r = 0$.

3.3.4 Charge distributions

Detailed simulations of electron cascades (fig. 3.13) around the wire can be carried out with the same MC. In this section, some statistical aspects of the multiplication mechanism

are briefly discussed, so that ion clouds can be generated quickly if desired. A thorough investigation of avalanches in NCD gas requires the inclusion of Penning ionization and photo-ionization in the program. For simplicity, these processes have been left out of the present work.

(a) *Gas gain*

Single electron gas gain distributions are found to be approximately exponential, with a mean gain $\bar{G} \sim 100$. The exponential shape is expected [63], and agrees with GARFIELD [61, 64]. However, the average multiplication factor is significantly lower than reported by NCD gain measurements ($\bar{G} \sim 219$) [43, 65]. In [66], it was shown that such discrepancies can be explained by a ‘phenomenological quantification’ of the Penning effect.

(b) *Azimuthal spread*

The distribution of ϕ angles (fig. 3.1) of ionization events in an avalanche has an RMS of 16° . So, ions do not surround the wire in a typical cascade.

(c) *Ionization radii*

The distribution of starting radii of secondary ions can be parametrized as a sum of two exponentials, $Ae^{Br} + Ce^{Dr}$, with $A = 3.35$, $B = -1.86 \times 10^5$, $C = -2.06$, $D = -5.98 \times 10^4$. The average starting radius is found to be $33 \mu\text{m}$, and is a good measure of the typical radial spread of a cascade. From Eq. 3.16, one can deduce that the mean duration of an avalanche is ~ 0.1 ns.

(d) *z distribution*

As discussed in §3.3.3, the RMS width of an avalanche along z is about $30 \mu\text{m}$. The z profile of secondary ions from an electron starting at any initial position (r_0, z_0) can be generated rapidly. One first picks the average z position, knowing $\sigma_{diff}(r_0)$ (fig. 3.11). Then, the number of ions is chosen randomly from an exponential distribution with $\bar{G} = 219$. The final z position of each ion in the cascade is sampled from a Gaussian with an RMS of $\sigma_{av} \sim 30 \mu\text{m}$. Because of the exponential gain dependence, the z profile differs significantly from one electron to another for any given (r_0, z_0) . Example simulated charge distributions are shown in fig. 3.14. This

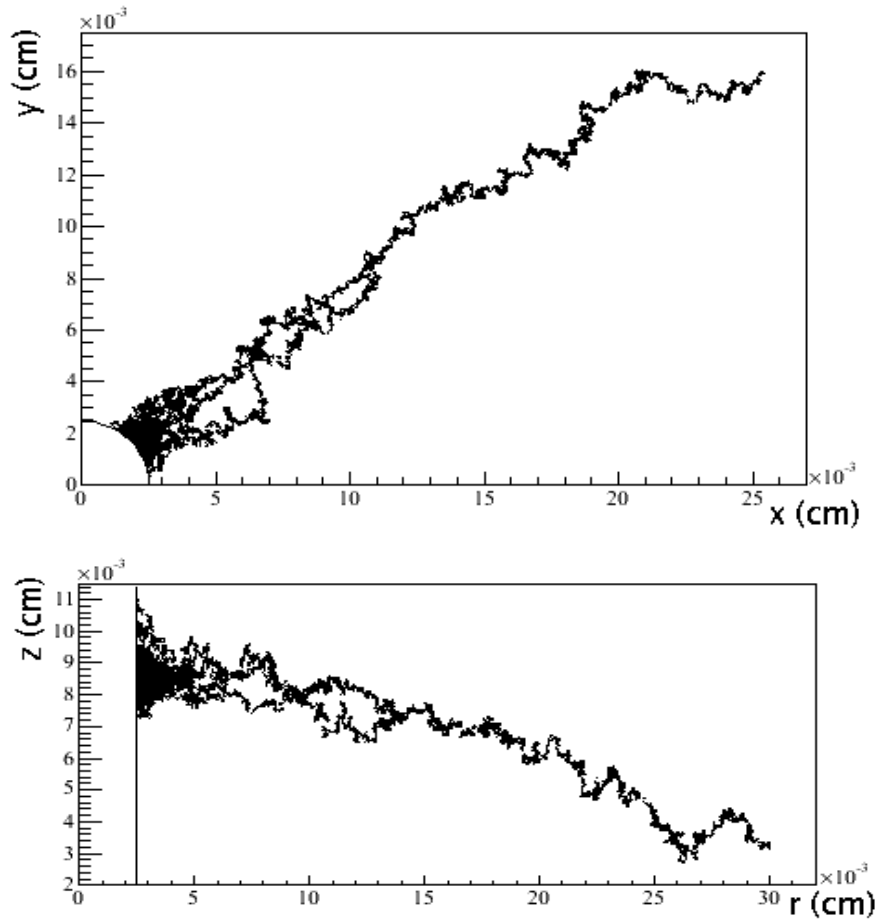


Figure 3.13: A typical electron avalanche resulting from an electron starting off at $r = 2.5$ cm and $z = 0$ cm in NCD gas, as simulated by the e^- transport MC. Top: the cascade in the radial plane; bottom: the same cascade viewed in the r - z plane. In this particular example, the electron diffuses a distance of ~ 85 μm perpendicular to the electric field, along z . As explained in the text, avalanche electrons start at a mean radius of ~ 33 μm . The mean angular spread of the cascade in the x - y plane is $\sim 16^\circ$, and the average width along z is ~ 30 μm .

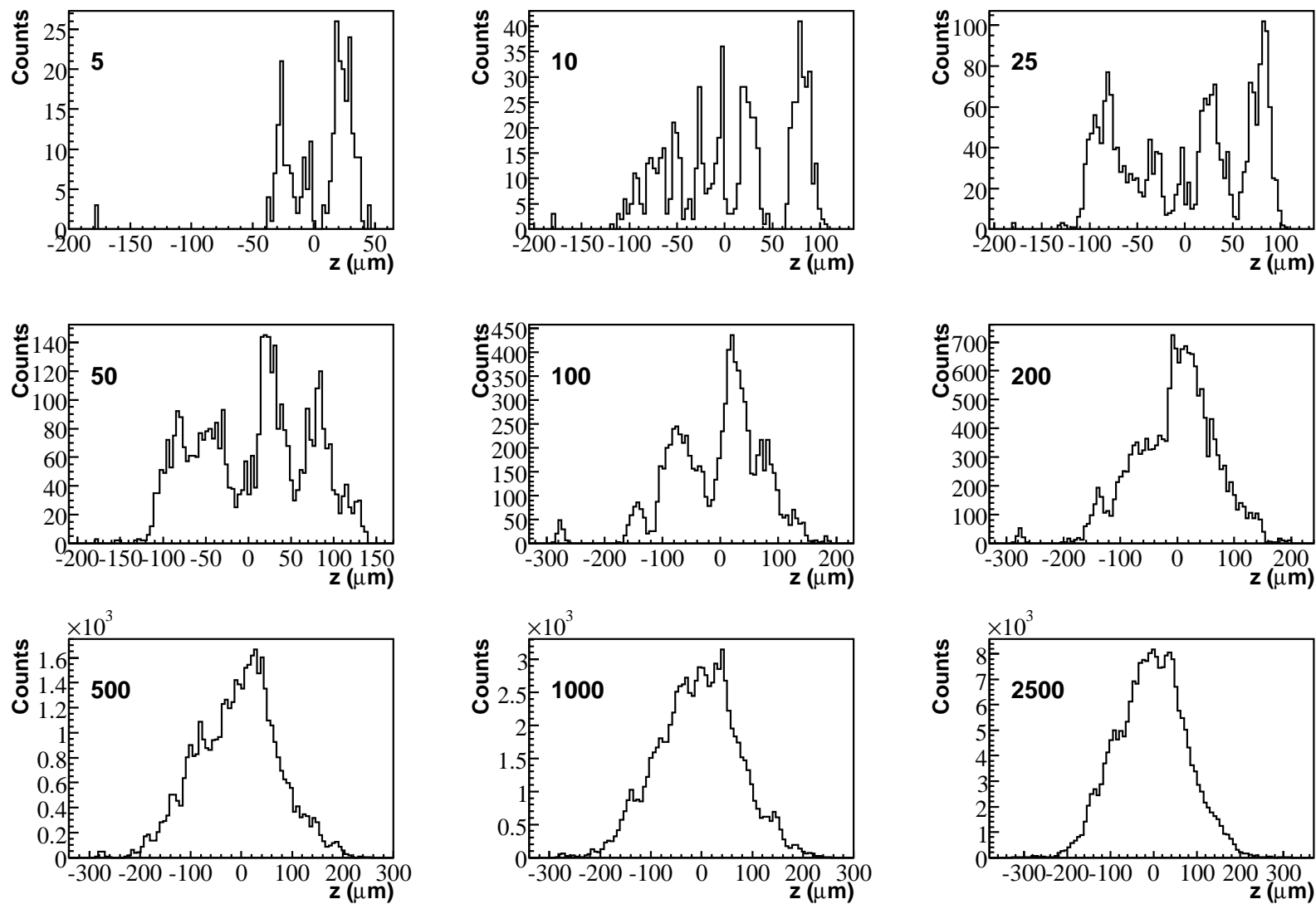


Figure 3.14: Calculated z positions of ions produced in avalanches resulting from 5, 10, 25, 50, 100, 200, 500, 1,000 and 2,500 electrons starting from the same radius and $z_0 = 0$. Because of diffusion, convergence to a Gaussian shape is slow.

shows charge distributions along the anode, calculated for 5, 10, 25...2,500 electrons starting at the same position. Convergence to a simple Gaussian shape occurs only in the limit of a very large number of incoming electrons. The very slow convergence is a result of the transverse diffusion of electrons and the exponential gas gain distribution.

It should be stressed that, when using these MC distributions, one has to assume that they are undistorted by Penning ionizations or photo-ionization. At thermal energies, ${}^3\text{He}$ ions move $\sim 0.2 \mu\text{m}$ during a typical discharge. Thus, it is likely that interactions involving excited ions occur within the dimensions given here.

3.4 Summary

This chapter explored proportional counter gas physics topics relevant to the computation of NCD pulses. A Monte Carlo simulation was used to calculate quantities that have not been measured directly: mean drift time (Eq. 3.16) and resolution (Eq. 3.17), diffusion along z (§3.3.3), avalanche sizes and ion distributions (§3.3.4). Several tests were carried out to ensure that the MC works properly. The drift time results are consistent with constraints set by SNO NCD pulses, and calculations carry a systematic error of about $\pm 3\%$. The width of pulses depends on other factors besides electron drift times. The t_d-r curve calculated in this work was scaled by $10 \pm 4\%$ to compensate for these effects. The results of this chapter are summarized in table 3.2.

Quantity	Symbol	Value
Drift time (in ns) from r ¶	$t_d(r)$	$(121.3r+493.9r^2-36.71r^3+3.898r^4)\times(1.10\pm 0.04)$
Time resolution (ns) †	$\sigma(t_d)$	$0.0124t_d + 0.559$
Mean avalanche radius	r_{av}	$\sim 33 \mu\text{m}$
Avalanche size along anode	σ_{av}	$\sim 30 \mu\text{m}$
Diffusion along wire (μm) ‡	$\sigma_{diff}(r)$	$\sigma_{diff}^2(r) = (101r + \sigma_{av})^2 - \sigma_{av}^2$
Avalanche azimuthal spread	ϕ_{av}	16°
Avalanche duration	t_{av}	$\sim 0.1 \text{ ns}$
Gain distribution	–	exponential
Mean gas gain ◇	\bar{G}	~ 100 (measured: 219)

Table 3.2: Summary of calculated e^- transport and avalanche properties in NCD gas. ¶: r is in cm; †: t_d is in ns; ‡: r is in cm, and σ_{av} in μm ; ◇: the discrepancy between the observed and measured values is explained in the text.

Chapter 4

Simulation of NCD Pulses

This chapter discusses the calculation of pulse shapes from any ionization event, as they would appear on the oscilloscopes. The computation of current waveforms requires the following questions to be answered: (1) What do ionizing particles do in NCD gas? (2) How do energy losses in the gas translate into signals on the anode?, and (3) What does the NCD hardware do to these signals?

In §4.1, a general numerical method for generating pulses is presented. All the major issues pertinent to (1)–(3) are then laid out and discussed in detail. These include: the ion current (§4.2), the stopping power, range, straggling, and track algorithms for protons, tritons, α particles, and electrons in NCD counters (§4.3 and §4.4), and the NCD hardware model (including reflections (§4.5.1), pulse propagation (§4.5.2) electronics (§4.5.3), and noise (§4.5.4)). The performance of the pulse simulation, its limitations, and the tuning of input variables are discussed in §4.6; improvements to the model are suggested. Non-standard α pulses originating from NCD wires and end-caps are discussed in §4.7.

The pulse calculation code is integrated within SNOMAN¹, the FORTRAN77-based, multi-purpose SNO simulation program. Details of the software implementation are given in appendix E.

4.1 Method

Regardless of track structure or particle type, all pulses are calculated using the same procedure. First, the charged particle trajectory is determined, and divided into N small *segments* of equal length l , each of which is approximated as a point charge. Next, the

¹SNO Monte Carlo and ANalysis.

energy and charge deposited inside each piece are computed. The total current resulting from the whole track at time t is, thus, a sum of individual currents from all point charges i , evaluated at t :

$$I_{track}(t) = \sum_{i=1}^N G_i \cdot n_{pair,i} \cdot I_{ion,i}(t - t_0) \quad (4.1)$$

where $n_{pair,i} = \frac{dE}{dx} \frac{l}{W}$ is the average number of electron-ion pairs in segment i . $W = 34$ eV is the mean energy required to produce an electron-ion pair². Stopping powers and the generation of trajectories for the different ionizing particles of interest are described in §4.3 and §4.4. The effects of lateral and energy straggling are discussed in §4.3.2 and §4.3.4, respectively. G_i , the effective amplification factor applied to i , can be calculated as the average of single-electron gas gains: $\frac{1}{n_{pair,i}} \sum_{j=1}^{n_{pair,i}} g_j$, where g_j is a random number sampled from an exponential distribution (see §3.3.4) with mean \bar{G}_i , and j loops through the individual electron-ion pairs in the segment. The value of \bar{G}_i differs from one segment to another, because of charge shielding by ions originating from earlier avalanches. This *space-charge* problem, and the calculation of appropriate values of \bar{G}_i , will be discussed in depth in the next chapter. t_0 is the difference between the drift times (calculated in chapter 3) of ionized electrons from the i^{th} segment, and the segment closest to the wire. $I_{ion,i}(t - t_0)$ is the induced current of a positive charge of magnitude e drifting towards the cathode. Its derivation is described in the next section. After evaluating the summation (Eq. 4.1), I_{track} subsequently needs to be convolved with the NCD hardware response. This is described in §4.5.

Looping through discrete time bins instead of segments, Eq. 4.1 can be expressed as a discrete convolution:

$$I_{track}(t) = \sum_{t > t_0} f_e(t) \cdot I_{ion}(t - t_0) = f_e \otimes I_{ion} \quad (4.2)$$

Thus, an efficient way of evaluating $I_{track}(t)$ is to first, calculate $f_e(t)$, the distribution of arrival times of electrons at the wire, then convolve with the ion current, $I_{ion}(t)$ (Eq. 4.5), using a Fast Fourier Transform (FFT) algorithm. $f_e(t)$ can easily be computed, knowing G_i , $n_{pair,i}$, and the drift time associated with each segment.

The speed of calculations depends, to a large extent, on the number of segments a trajectory is divided in. For computational accuracy, the size of segments is, by default,

²This value of W , measured by Oblath [65], is assumed to be the same for p , t , α and e^- in NCD gas, and to be constant over the energy range of relevance (0.2–9 MeV).

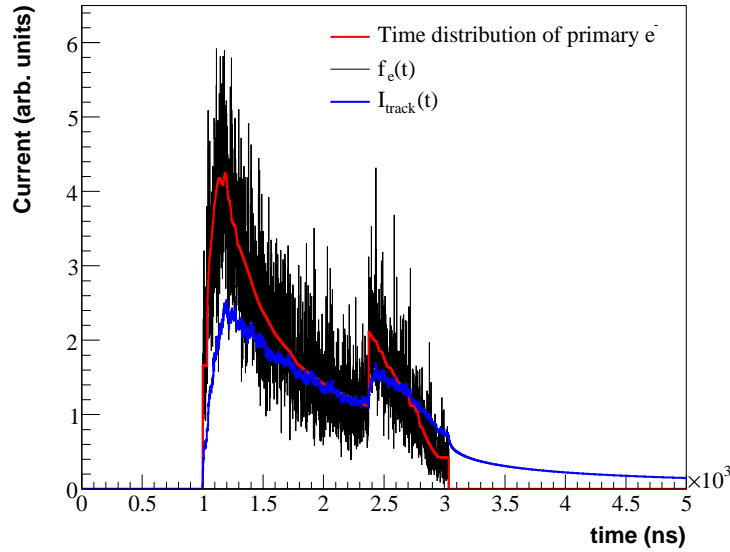


Figure 4.1: Steps in the calculation of I_{track} for a p - t track that is perpendicular to the anode. The start time has been shifted to $1 \mu\text{s}$ for clarity.

chosen to be $\sim 1 \mu\text{m}$ for all sections of the track, which amounts to $\sim 10,200$ divisions for a typical neutron pulse. The optimal segment length is governed by the bin width of recorded scope traces. It is desirable for electrons from two adjacent segments to reach the wire within a bin width (1 ns). The stringest requirement is set on tracks that are perpendicular to the wire and point radially inwards (or outwards), in which case the distance between two segments should not exceed $4.5 \mu\text{m}$.

The various steps in the calculation of I_{track} are illustrated in fig. 4.1, for a p - t track perpendicular to the anode, with the proton moving radially inwards. The red curve is the distribution of primary electron arrival times at the wire. The black curve is $f_e(t)$, while the blue pulse is $I_{track}(t)$. Fluctuations on $f_e(t)$, which are a result of randomizing the single-electron gas gains, are smoothed out after convolving with the ion tail. All curves are normalized to the same area.

The power of the numerical approach discussed here, is that *any* pulse can be computed, given the location and number of ionization electrons in the event. Fig. 4.2 illustrates representative current pulses I_{track} , from the three major classes of physics events: (1) a neutron capturing at $r = 1.29 \text{ cm}$, with the p - t track at 67° with respect to the wire, and the proton travelling outwards (top row), (2) a 5 MeV α starting at $r = 2.5 \text{ cm}$, travelling inwards, and almost perpendicular to the anode (middle row), and (3) a 5 MeV

electron starting at the edge of the gas (last row). Projections of particle trajectories in the radial plane are shown on the left column. Each event type displays characteristic shapes that are not easily reproduced by the other species:

Neutron pulses commonly contain two widely-separated crests arising from the proton Bragg peak and the ionization profile of the triton. p - t events that are parallel to the wire, and tracks that hit the counter walls do not share this property. In contrast, most α pulses in the neutron energy region are narrow and single-peaked, with the exception of distorted pulse shapes from counter ends. Low-energy ^{210}Po α pulses are characteristically narrower than bulk α events. Other classes of α pulses will be discussed later in this chapter, in §4.7.1 and §4.7.2.

The majority of β events produce low-amplitude pulses that do not result in *both* a MUX and a shaper trigger. These appear as shaper noise, and low-energy spiky pulses. However, on very rare occasions, a sufficiently high-energy MUX-shaper correlated pair might be produced. In these cases, it is likely that the resulting pulse has a ragged structure, owing to elastic scatters off the nickel, *e.g.* as in fig. 4.2 (bottom).

4.2 Current from point charges

In the last section, it was mentioned that I_{track} is evaluated as the sum of point charge currents $I_{ion,i}$ from a number of charge segments. The calculation of I_{ion} is now described in detail.

Any particle with charge q at radius r in the counter induces a charge on the anode, which by Green's reciprocity theorem, is given by [67]:

$$\Delta Q = q \frac{\ln(b/r)}{\ln(b/a)} \quad (4.3)$$

where b is the counter radius and a the anode radius. Thus, if the particle moves, the magnitude of the induced charge changes, and a current $I(t)$ can be read off the anode:

$$I(t) = \frac{d\Delta Q}{dt} = \frac{q}{V} \mathcal{E} v(\mathcal{E}) \quad (4.4)$$

where V is the anode voltage, and v is the drift velocity of the particle, which is a function of the electric field \mathcal{E} . For a positive ion drifting towards the cathode, assuming $v(\mathcal{E}) = \mu_i \mathcal{E}$ with a field-independent ion mobility μ_i , Eq. 4.4 reduces to Wilkinson's formula [67]:

$$I_{ion}(t) = -\frac{q}{2\ln(b/a)} \frac{1}{t + \tau} \quad (4.5)$$

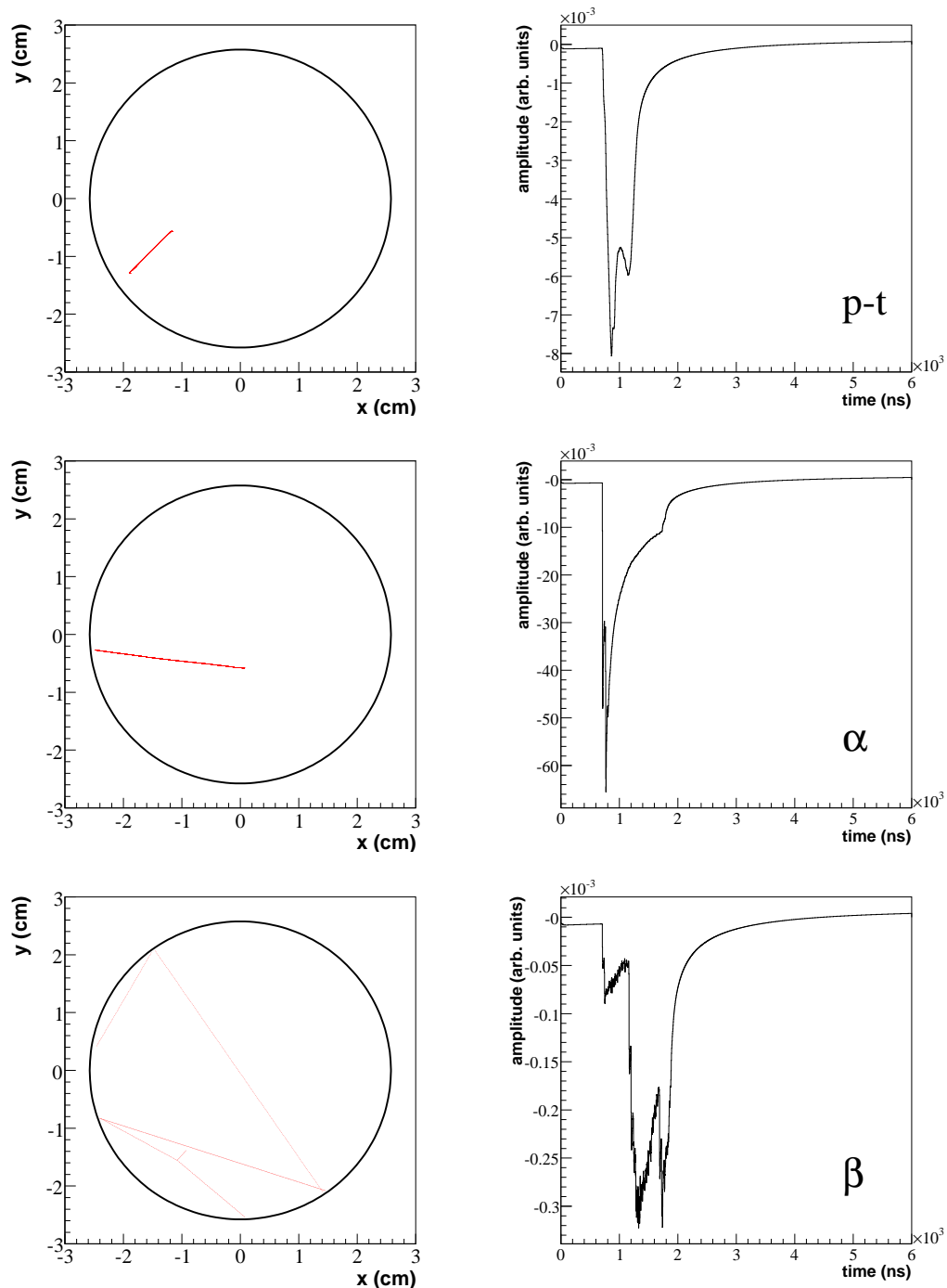


Figure 4.2: First row, left: a neutron capturing at $r = 1.29$ cm, with the proton going outwards and the p - t track at 67° with respect to the anode. Right: The resulting pulse shape; the first narrow peak is due to the triton. Second row: a 5 MeV α particle starting at $r = 2.5$ cm, and travelling inwards. Third row: A 5 MeV electron starting from the edge of the gas and scattering thrice on the walls before being absorbed in the nickel. A small δ -ray resulting from a M\"oller scatter can be seen at $(-1.2, -1.5)$. The resulting NCD pulse has a large width owing to the large radial span. This event does not trigger the detector.

where the ion constant $\tau = \frac{r_0^2 \ln(b/a)}{2\mu_i V}$, r_0 being the starting radius of the ion. An ion mobility of the order of $10^{-8} \text{ m}^2\text{V}^{-1}\text{ns}^{-1}$ yields an ion constant of a few ns. Note that when the voltage is altered, τ changes, and the tail decays faster or slower depending on the size of $r_0^2(V)$ with respect to V .

In the case of an electron, one can get an idea of the pulse shape to first order, by assuming $v \propto \mathcal{E}^{\frac{1}{2}}$ (this does not hold at high fields). Eq. 4.4 then becomes:

$$I_e(t) = \frac{2q}{3\ln(b/a)} \frac{1}{t - \tau_e}, \quad t < \tau_e \quad (4.6)$$

where $q = e$ and τ_e is the analogue of τ , for electrons. Clearly, the current starts slowly and rises rapidly until the electron is collected.

Now consider an electron-ion pair created at radius r . Since there is an avalanche of gain G close to the wire, the current due to the primary electron-ion pair can be neglected, so that the pulse presumably results from ions and electrons in the cascade. If both of these start at a mean distance $r_0 \sim 33 \mu\text{m}$ from the wire (as estimated in §3.3.4), electrons are collected in ~ 0.1 ns, while ions remain almost motionless. Therefore, induced charges at the wire, from both kinds of particles, are approximately equal and opposite (a small difference of ~ 4 % coming from the drift of electrons over $8 \mu\text{m}$ to the anode), and there is virtually no net current until all avalanche electrons reach the anode.

To summarize, NCD pulses should result mainly from the slow-drifting ions produced in avalanches near the wire. The formula for a single ion moving towards the wall is given by Eq. 4.5. The inductive effect of electrons cancel out with that of ions, because electrons and ions remain in close proximity until the cascade is over. This means that any electron current can be safely neglected.

4.3 Protons, tritons and alphas in NCDs

4.3.1 Stopping and range of ions in NCD gas

In this work, one is primarily concerned with protons, tritons and α particles starting off in NCDs with 191 keV, 573 keV, and 0.191–8.8 MeV, respectively. At these energies, radiative losses are negligible and the total stopping power S_t is the sum of the electronic stopping power, S_e , due to inelastic interactions with electrons, and the nuclear stopping

power, S_n , due to elastic collisions with nuclei in the gas:

$$S_t = S_e + S_n \quad (4.7)$$

S_e is expected to be the dominant contribution, except at very low energies. For α particles with a few MeV of kinetic energy, S_e can be accurately calculated using established theoretical prescriptions, such as the Bethe-Bloch formula, or the photoabsorber-interaction model from Allison and Cobb [68]. However, at lower energies one has to rely on semi-empirical fits to existing data. In this work, the empirical fits and programs (SRIM and TRIM³ [62]) of Ziegler, Biersack, Littmark (ZBL) and other collaborators are used. Their approach is briefly summarized below:

ZBL give S_n (in eV/(10¹⁵ atoms/cm²)) as [69]:

$$S_n = \frac{8.462Z_1Z_2M_1S_n(\epsilon)}{(M_1 + M_2)(Z_1^{0.23} + Z_2^{0.23})} \quad (4.8)$$

ϵ , the reduced energy, is defined as

$$\epsilon = \frac{32.53M_2E}{Z_1Z_2(M_1 + M_2)(Z_1^{0.23} + Z_2^{0.23})} \quad (4.9)$$

Z_1 , M_1 (a.m.u) and E (keV) denote the atomic number, mass, and kinetic energy of the projectile. Z_2 and M_2 are the corresponding quantities of the target nucleus.

For $\epsilon < 30$, in the presence of screening⁴ $S_n(\epsilon)$ takes the form

$$S_n(\epsilon) = \frac{\ln(1 + 1.1383\epsilon)}{2(\epsilon + 0.01321\epsilon^{0.21226} + 0.1959\epsilon^{0.5})} \quad (4.10)$$

For $\epsilon > 30$, assuming pure Coulomb potential,

$$S_n(\epsilon) = \frac{\ln(\epsilon)}{2\epsilon} \quad (4.11)$$

ZBL obtained an expression for S_e empirically:

$$\frac{1}{S_e} = \frac{1}{(A_1E^{A_2} + A_3E^{A_4})} + \frac{E^{A_6}}{A_5\ln\left(\frac{A_7}{E} + A_8E\right)}, \quad 25 \text{ keV} \leq E \leq 10 \text{ MeV} \quad (4.12)$$

$$S_e = E^{0.25}, \quad E < 25 \text{ keV} \quad (4.13)$$

³Stopping and Range of Ions in Matter, and TRansport of Ions in Matter.

⁴ZBL use of their own screening potential, which they derived through fits to the theoretical potentials of a large number of particle-target pairs.

The constants $A_1 \dots A_8$ for the passage of protons and α particles in all elements are tabulated in [70] and [71]. Their values, for protons travelling in C, F and He, are listed in table 4.1. The stopping power for the NCD gas mixture is obtained by applying Bragg's rule⁵, with suitable corrections [73]. The average distance travelled by an ion with energy E_0 is obtained by integrating the reciprocal of the total stopping power:

$$R = \int_{E_0}^0 S_t^{-1} dE \quad (4.14)$$

These calculations can be performed by SRIM. Its predictions of S_t and R for protons, tritons and α particles are shown in fig. 4.3, as a function of energy. The range of 573 keV protons in the NCD gas mixture is 0.73 cm, while that of 191 keV tritons is 0.28 cm.

Atom	A_1	A_2	A_3	A_4	A_5	A_6	A_7	A_8
He	0.489	0.0050512	0.86135	0.46741	745.38	1.04227	7988.39	0.033329
C	2.10544	0.0049079	2.08723	0.46258	1779.22	1.01472	2324.45	0.020269
F	1.30187	0.0051414	3.82737	0.28151	2829.94	1.02762	7831.3	0.02094

Table 4.1: Constants for the parameterization of S_e for protons passing through He, C and F.

4.3.2 Proton, triton and α particle tracks

A realistic simulation of proton, triton and α particle trajectories has to be implemented to account for any pulse shape distortions that might result from large-angle scatters. The method described in this section closely follows the one developed by ZBL for the TRIM Monte Carlo [69].

It is not practical to simulate every single interaction along the path of the particle. To draw tracks accurately and efficiently, the path length Δl is chosen such that the average deflection due to multiple scattering is sufficiently small. To achieve this, one can equate the energy loss for a deflection of $\sim 5^\circ$ in an elastic collision (from Eq. 3.8) to $\Delta l S_n$, with S_n given by Eq. 4.8. This gives Δl in cm:

$$\Delta l = \frac{0.02(1 + M_1/M_2)^2 \epsilon^2 + 0.1\epsilon^{1.38}}{4\pi N a^2 \ln(1 + \epsilon)} \quad (4.15)$$

⁵Bragg's rule states that the stopping power of an ion in a compound is given by a weighted sum of individual stopping powers for the constituent elements [72].

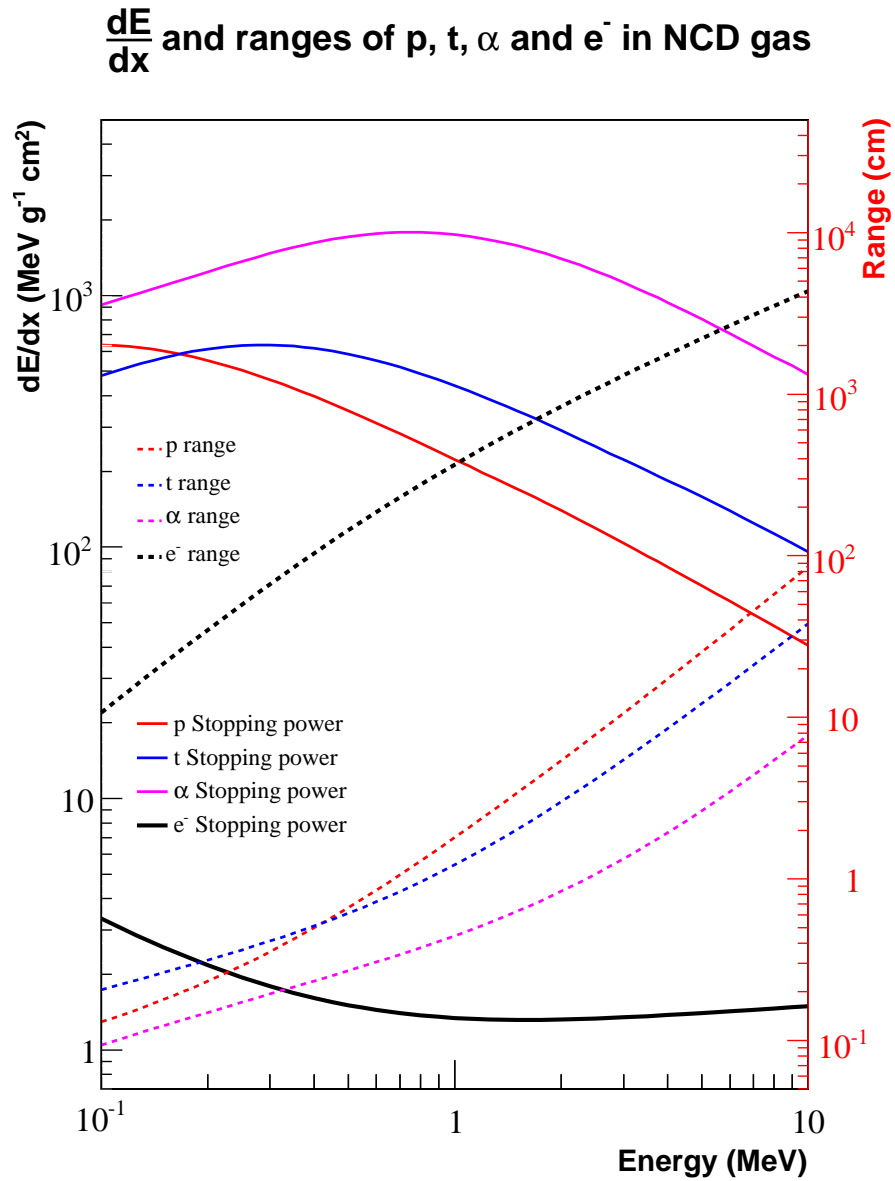


Figure 4.3: $\frac{dE}{dx}$ (solid lines) and stopping ranges R (dashed lines) of protons (red), tritons (blue), α particles (magenta) and electrons (black) in NCD gas. Calculations for protons, tritons and alphas are from SRIM [62]; those for electrons are from PEGS4 [74].

where $a = (0.4685 \cdot 10^{-8} / (Z_1^{0.23} + Z_2^{0.23}))$ cm and N is the number density in atoms per cm^3 . The procedure for randomizing the scattering angle (or equivalently, the impact parameter), based on the above value of Δl , is as follows. If p is the impact parameter, an interaction occurs in a volume of gas equal to $\pi p^2 \Delta l$. On average, the volume of a target is N^{-1} . The interaction volume can be assumed to be exponentially distributed, which means that the probability of a collision occurring with impact parameter p is $P = 1 - e^{-N\Delta l\pi p^2}$. Therefore, one can choose p randomly, given any Δl , by:

$$\pi p^2 = -\frac{\ln(R)}{N\Delta l} \quad (4.16)$$

where R is a random number between 0 and 1. Given p and ϵ , the scattering angle is determined using the recipe outlined by ZBL in [69]. Their method is essentially an analytic solution to the classical scattering integral. The energy loss in a track section Δl is the sum of the energy change due to elastic deflection Eq. 3.8, and through interactions with electrons. The *average* electronic energy loss is assumed to be continuous, and is given by $\Delta l S_e$, where S_e can be obtained in tabular form from SRIM, or evaluated using Eq. 4.12.

Fig. 4.4 shows 3,000 calculated p - t and 1 MeV α particle tracks in NCD gas, all starting off in the same initial direction (parallel to the vertical axis) from the origin. The deviation of the track end points with respect to the initial line of travel is referred to as *lateral straggling*. To check the track simulation, the RMS of the straggling distributions, which are approximately Gaussian, were compared with those from TRIM. Agreement between the two simulations is within 16 % for all particles and energy ranges concerned (see fig. 4.5 for alphas).

All tracks are assumed to appear instantaneously in the gas. For instance, a non-relativistic calculation yields mere flight times of ~ 2 ns for the proton and ~ 4 ns for the triton. Hence, any broadening effects on pulse shapes are negligible⁶. It is further assumed that all primary and secondary electron-ion pairs are created along the ion trajectory. According to Rudd *et al.* [75], the kinetic energy imparted to ionized electrons in helium by ~ 1 MeV protons is likely to be less than 1 keV in helium gas. The range of 1 keV electrons in counter gas is less than $60 \mu\text{m}$ [76], or at most only 0.5 % of the total length of a fully-contained p - t track. Consequences on pulse shapes, apart from a minor smearing

⁶The narrowest ionization pulses in the neutron energy window have a FWHM in excess of 200 ns.

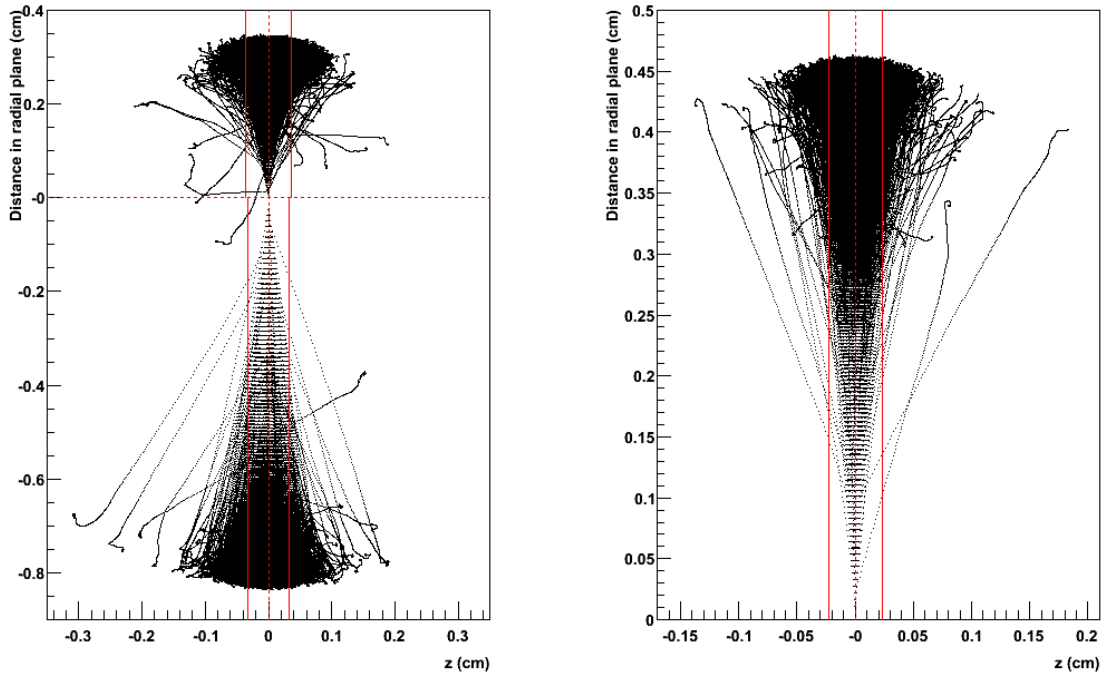


Figure 4.4: Simulation of particle trajectories in NCD gas, with the method described in §4.3.2. All particles start at the origin; a conical shape results from early scatters in particle tracks. Left: p - t tracks, with tritons directed upwards, and protons downwards; right: 1 MeV α tracks. $1\text{-}\sigma$ deviations from straight-line travel are shown in solid red lines. These are: 0.33 mm for 573 keV protons, 0.37 mm for 191 keV tritons, and 0.23 mm for 1 MeV alphas.

effect, are negligible.

4.3.3 Straight track approximation

As seen in fig. 4.4, the majority of p - t and α events result in quasi-straight tracks. When this is the case, a faster, semi-analytic pulse calculation can be devised. The algorithm is briefly described in appendix C. A straight line trajectory can be described by three variables (r_0, θ, ϕ) (see fig. 4.6), defined as follows: r_0 is the initial radius of the charged particle (for p - t tracks, this is the neutron capture radius). ϕ is the angle between the direction of travel of the ion and the radial vector pointing inwards, from the starting point of the track, to the anode. For neutron events, ϕ specifies the direction of the proton in the radial plane; the triton direction is then $\pi - \phi$. The third coordinate, θ is the angle of the track with respect to the vertical anode wire. This coordinate system is convenient, because particle tracks can be described without making any reference to the

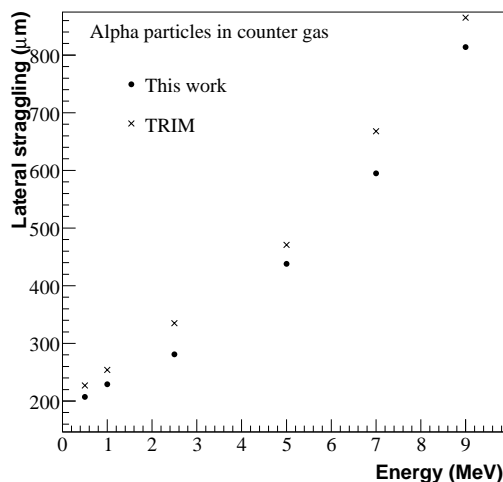


Figure 4.5: Lateral straggling of alpha particles in NCD gas in μm , as calculated by TRIM and the simulation presented here. The lateral straggling is calculated as the RMS spread of track endpoints in a plane perpendicular to the initial direction of travel.

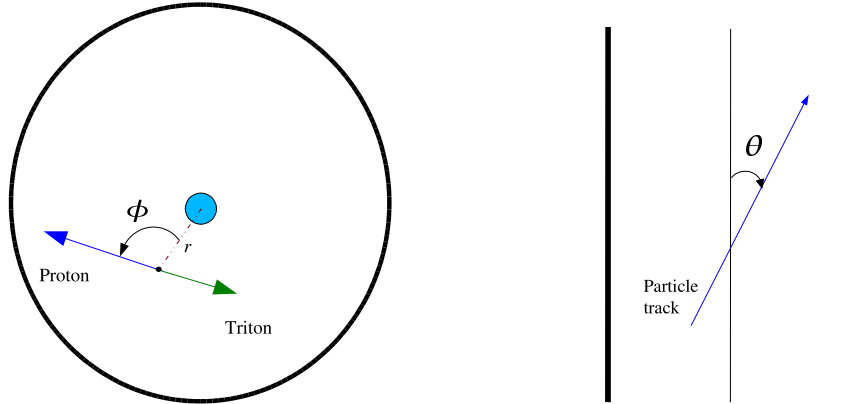
position of the NCD string in the array.

A neutron pulse shape is a function of four parameters (r_0, θ, ϕ, z) with z being the vertical position of capture on the string. Unlike neutrons, α particles originating from inside the nickel wall can start off in the gas with a range of energy values. Therefore, an alpha pulse shape is also a function of four parameters (E, θ, ϕ, z) , where E is the initial energy of the particle in the gas. A perfectly straight track at $\theta = 0^\circ$ effectively results in a point charge pulse. In general, pulses become wider with increasing θ , and for any given (r_0, θ) , the width is narrowest at $\phi = 90^\circ$.

4.3.4 Energy straggling of ions in NCD gas

In §4.3.2, a method for tracing particle tracks was described, where energy losses through interactions with electrons are not randomized. The effects of these fluctuations on pulse shapes are now discussed.

At any given speed, the energy loss distribution of a charged particle depends critically on the thickness of material it passes through. For neutron pulses, the average number of primary electron-ion pairs accumulated at the wire within 1 ns (the scope bin size) is ~ 21 , which corresponds to an energy loss of ~ 714 eV. Assuming a mean excitation energy of 50 eV for counter gas [76], this amounts to a average of ~ 14 collisions. The en-

Figure 4.6: Definition of r_0 , θ and ϕ .

ergy loss distribution that applies to this situation is unclear [77], but can be determined using Monte Carlo methods (see, for example, [78]).

Fluctuations on pulse shapes arising from energy straggling do not matter if the RMS baseline noise on NCD pulses is dominant. Indeed, to a large extent, they are washed out after propagation through the NCD anode, cables and electronic filters. To demonstrate this, a number of 573 keV proton pulses (at different track angles) were calculated in two different ways, using the procedure outlined in §4.1: (1) The number of primary electron-ion pairs collected within 1 ns is crudely assumed to be Poisson distributed. The mean is calculated using SRIM stopping power tables. (2) No Poisson fluctuation is applied. Differences between (1) and (2) are taken for all pulses, and found to be negligible compared with typical baseline noise RMS. It was therefore decided to neglect energy straggling in pulse calculations.

4.4 β particles

At any time, a large number of β particles wander around in NCD counters, on account of the Compton scattering of γ -rays, and the radioactive decay of impurities, both within and outside the detectors, *e.g.* ${}^3\text{H}$, ${}^{238}\text{U}$ and ${}^{232}\text{Th}$ chain isotopes. Any electron possessing over 200 keV of kinetic energy has a small chance of producing a scope-shaper event pair.

The propagation of electrons and gamma rays in NCD gas is handled by the EGS4⁷

⁷Electron Gamma Shower.

package [74], with a few routines added to retrieve the particle track structure for pulse calculations. The interactions of decay electrons with NCD gas in the energy range of interest can be classified in three main categories: (1) excitations and ionizations, (2) elastic interactions with electrons, *i.e.* Möller scattering, and (3) bremsstrahlung. The primary mode of energy loss is via inelastic collisions with gas particles, which can be evaluated using the Bethe-Bloch formula. The resulting range and stopping power curves, evaluated with the PEGS4 program [74], are shown in fig. 4.3. The low stopping power means that, in contrast to p , t and α particles, electron-ion pairs are not produced quasi-continuously along the track. To take into account this effect, it is assumed that the distance between primary electron-ion pairs, at a certain electron energy E , is exponentially distributed with mean $\lambda = W/\langle \frac{dE}{dx} \rangle$, where W is the average energy required to create an electron-ion pair.

The long electron mean free paths imply that β tracks in NCD gas are rather unperturbed. Typically, a large number of scatters on the nickel walls occur, extending the particle journey within the gas itself. Occasionally, Möller scattering produces δ -rays that complicate the pulse structure.

4.5 Hardware model

A simplified model of the NCD electronics chain (fig. 2.3), which has been shown to accurately represent the full DAQ system [29], is shown in fig. 4.7. This consists of: (1) the NCD string, delay line and cable, (2) a preamplifier unit, and (3) read-out hardware composed of a MUX, log-amplifier, two oscilloscopes, and shaper. This section discusses how ionization pulses transform at different steps in the chain.

4.5.1 Pulse reflections

Upon its creation on the NCD wire, a current pulse divides into two halves, which propagate in opposite directions. The downward-going part travels through an impedance-matched delay line (see fig. 2.1) and is reflected at the bottom of the string. Thus the total current I_T coming out from the top of a string is the sum of the direct (I_D) and reflected (I_R) components,

$$I_T = I_D + I_R \tag{4.17}$$

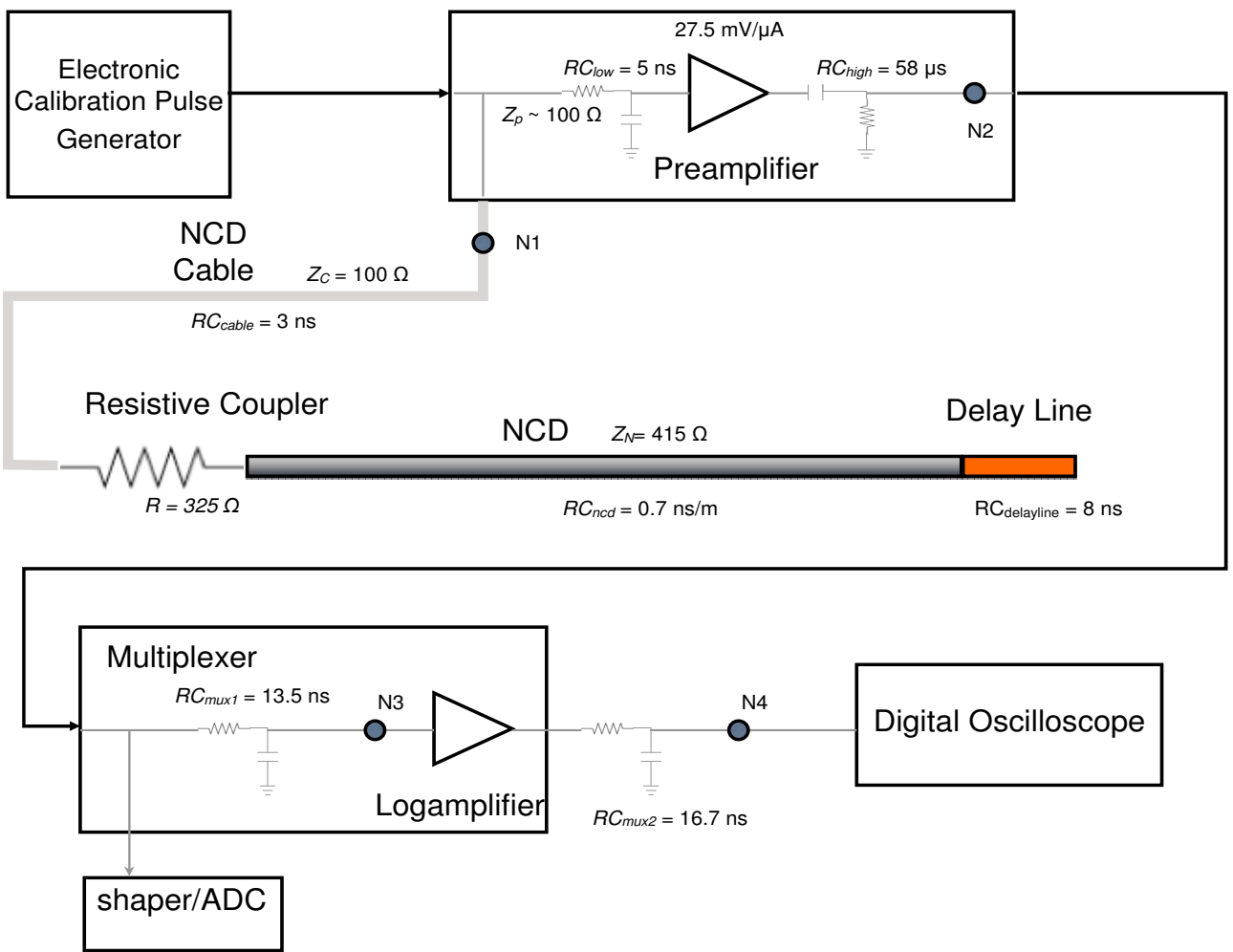


Figure 4.7: Simplified model of the NCD electronics and DAQ. Figure adapted from [79]

If an event occurs at a vertical position z in the counter with the origin situated in the middle of the gas region, the time lag δ between direct and reflected components is given as

$$\delta = \frac{1}{v_p} [L - L_D + 2z] + t_D \quad (4.18)$$

where the speed of propagation v_p in the wire has been measured by McGee to be $0.86c$ [80]. L is the length of the counter, and t_D is the time delay due to the delay line (~ 89 ns). $L_D \sim 16$ cm is the physical length of the delay line.

Further reflections can occur at other points in the chain, *e.g.* at the preamplifier, due to mismatches between the NCD cable and preamplifier input impedance. Such reflections are observed in micro-discharge events, which are very sharp current spikes originating from the delay line. The sharpness of these pulses allows the different reflective components to be resolved. Fig. 4.8 (red curve) is an averaged microdischarge pulse from string 27, showing: I_D (first peak), I_R (making up most of the second, lower-amplitude and broader peak), and the reflection of I_R off the preamplifier travelling to the top of the NCD string, and back through the preamplifier (third peak at ~ 200 ns). The corresponding reflection of I_D is combined with I_R to appear as the second peak.

A simulated micro-discharge pulse (black curve) is overlaid for comparison. The separation between the second and third peaks matches the NCD cable round-trip time of string 27. The two quantities that need to be adjusted in the simulation are: (1) the fraction $\frac{|I_D|}{|I_T|}$, (2) the transmitted pulse fraction at the preamplifier. These values have to be determined empirically from NCD pulses, because the extent of impedance mismatches are unknown. Based on studies of micro-discharge pulses from string 27, (1) and (2) have been tuned to 0.56 and 0.85, respectively⁸.

It is observed in fig. 4.8 that the data has a more prominent tail. This indicates that there might be reflections in the electronics chain that have not been simulated. Distributions of pulse shape variables that depend strongly on the tail of pulses can be biased as a result.

⁸String 27 is assumed to be representative of the array, due to the absence of micro-discharge pulses on most strings.

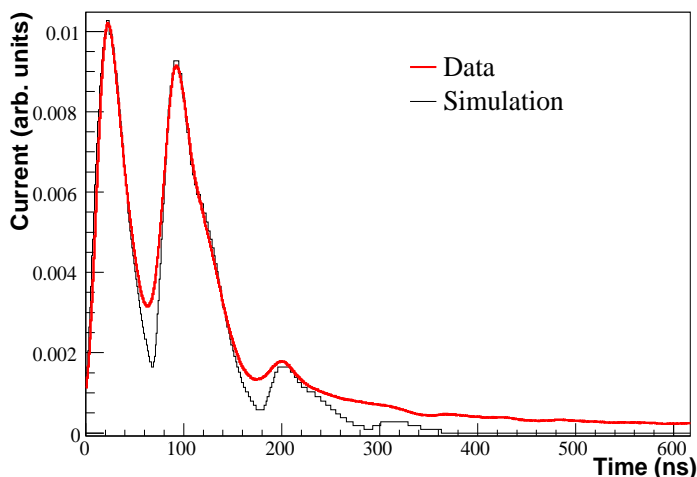


Figure 4.8: Average micro-discharge pulse from string 27 (red). The black curve is the simulated response of the string to a sharp impulse originating within the delay line. The second, broader peak is the reflected component at the bottom of the NCD, while the third, smaller peak results from the second peak being reflected off the preamplifier. The very small peak at ~ 320 ns is a second preamplifier reflection.

4.5.2 Propagation along NCD wires

In fig. 4.8, the first and second peaks have their own distinct shapes, owing to different degrees of attenuation and dispersion in the NCD wire. To first order, both the wire and delay line can be modeled as low-pass filters⁹. The pulse simulation makes use of a more detailed, lossy transmission line model developed by Oblath [65]. Inputs to this model were determined using test bench measurements at the University of Washington. The cables connecting the top of NCDs to the preamplifiers are also modeled as low-pass filters with $RC = 3$ ns.

4.5.3 Electronics and DAQ

The electronics model (fig. 4.7) used in pulse calculations closely follows the prescriptions of the NCD electronics calibration group¹⁰ [29, 82, 81]. In their model, the preamplifier, which has a gain of 27.5 mV/ μ A, acts as a low-pass filter ($RC = 3$ ns) and a high-pass filter ($RC = 58$ μ s) in series. Shapers are simulated simply by integrating pulses in a 6

⁹ RC values of 0.7 nsm⁻¹ for the NCD wire and 8 ns for the delay line have been proposed [81].

¹⁰The implementation of the electronics model and the MUX and shaper triggers within the pulse simulation code was carried out by Oblath, Deng and Prior.

μs time window. The 320 ns delay cable in the MUX box is modeled as a low-pass filter with $RC = 13.5$ ns. The log-amplifier acts on an input pulse V'_{in} as follows [29]:

$$V_{log}(t) = a \cdot \log_{10} \left| 1 + \frac{V'_{in}(t - \Delta t)}{b} \right| + c_{chan} + V_{PreTrig}^{ADC} \quad (4.19)$$

The parameters a , b , c_{chan} , Δt , and $V_{PreTrig}^{ADC}$ were determined during routine electronic calibrations, and stored in data banks. The circuitry between the log-amplifier and the scope is again simulated as a low-pass filter with time constant 16.7 ns. The final, log-amplified, amplitudes in each time bin are rounded off to the nearest integer to simulate digitization. Baseline noise is added using the method described in the next section. The various RC constants needed in this empirical model were measured by Huang, and are summarized in table 4.2. Preamplifier RC values are listed in table A.1 for each string.

Fig. 4.9 shows the transformation of I_{track} (the same pulse as in fig. 4.1) through the different steps in the electronics chain described briefly above. $I_T = I_D + I_R$ is in yellow, while the preamplified pulse is in magenta. The final, ‘observed’ log-amplified pulse is shown in grey, after the addition of baseline noise.

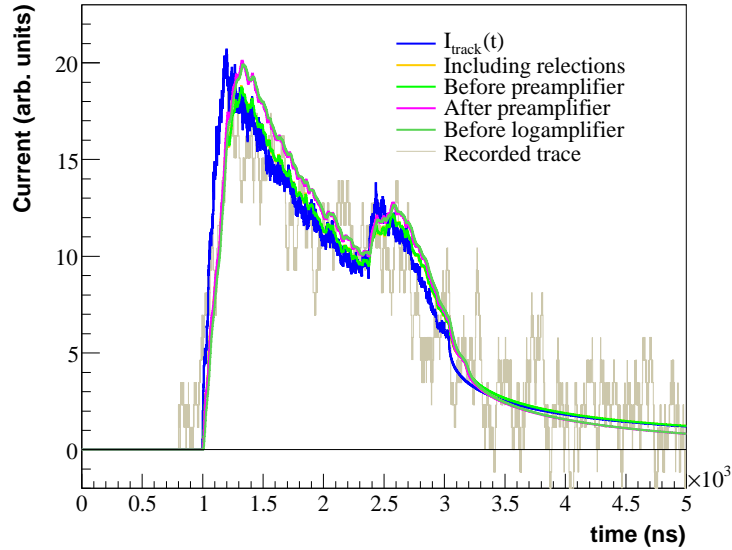


Figure 4.9: Effects of NCD electronics on I_{track} for a neutron event with $\theta = 90^\circ$ and $\phi = 0^\circ$.

Electronic Components	RC (ns)
Dispersion per metre	~ 0.7
Delay line	5.5 ± 0.7
low-pass filter before log-amp	13.3 ± 0.6
low-pass filter after log-amp	16.7 ± 1.8
Preamplifier (low pass)	3.27
Preamplifier (high pass)	58000
NCD cable	3

Table 4.2: Typical values of RC constants used in the electronics simulation [82].

4.5.4 Simulation of NCD baseline noise

It is essential to include noise with the appropriate RMS and frequency characteristics on simulated NCD pulses. The electronics chain being rather complex, it is difficult to build an accurate noise model from first principles. One such model can be devised by adding a Gaussian noise source between each low-pass filter in the electronics chain, *e.g.* at N_1, N_2, N_3 and N_4 in fig. 4.7 [79]. The contributions of each noise source are then varied, such that a reasonable fit to the observed noise power spectrum is obtained. This yields good agreement with typical NCD spectra up to frequencies of ~ 50 MHz, but the spectral shape at higher frequencies is not explained by the simplified electronics model in fig. 4.7.

A rather different method was developed to generate NCD noise directly from observed power spectra. This technique is based solely on simple statistical arguments, and does not require detailed knowledge of the NCD hardware itself. Therefore, no assumptions need to be made about the nature, location, and magnitude of individual noise sources.

4.5.4.1 Method

Consider the noise power spectrum Ω . At the i^{th} frequency, Ω_i is the square of the real (X_i) and imaginary (Y_i) parts of the i^{th} Fourier amplitude,

$$\Omega_i = X_i^2 + Y_i^2 \quad (4.20)$$

If the following conditions are satisfied: (1) X_i, Y_i are independent random variables, *i.e.* the phase $\Phi_i = \tan^{-1}(Y_i/X_i)$ is randomly distributed between $-\frac{\pi}{2}$ and $\frac{\pi}{2}$, and (2) X_i, Y_i are Gaussian distributed around zero with the same standard deviation σ_g , then Ω_i is exponentially distributed with mean μ_e given by:

$$\mu_e = 2\sigma_g^2 \quad (4.21)$$

Therefore, once the average noise power spectrum is determined (*i.e.* the values of μ_e at all frequencies), one can randomly generate the real and imaginary components of all frequency amplitudes. After Fourier-inverting the series, a noise sample sharing the same frequency properties, and having the same RMS as the data, is obtained.

4.5.4.2 Proof of $\mu_e = 2\sigma_g^2$

Let $Z_i = X_i^2$. If the probability distribution $P(X_i)$ is a Gaussian with mean $\mu_g = 0$ and standard deviation σ_g , $P(Z_i)$ is of the form

$$P(Z_i) = P(X_i) \frac{dX_i}{dZ_i} \propto \frac{e^{-Z_i/2\sigma_g^2}}{2\sqrt{Z_i}} \quad (4.22)$$

Now, if X_i and Y_i are independent, $P(\Omega_i) = P(X_i^2) + P(Y_i^2)$ is proportional to the convolution

$$P(\Omega_i) \propto \int_0^\infty \frac{e^{-Z_i/2\sigma_g^2} e^{-(\Omega'_i - Z_i)/2\sigma_g^2}}{\sqrt{Z_i(\Omega'_i - Z_i)}} dZ_i \quad (4.23)$$

$$\propto e^{-\Omega_i/2\sigma_g^2} \sin^{-1} \left(\frac{2Z_i}{\Omega'_i} - 1 \right) \Big|_0^\infty \propto e^{-\Omega_i/2\sigma_g^2} \quad (4.24)$$

The integral is finite because $\frac{Z_i}{\Omega'_i} = \cos^2 \Phi_i$ always lies between 0 and 1, and $\lim_{Z_i \rightarrow \infty} \frac{Z_i}{\Omega'_i} = 1$. Thus, $P(\Omega_i)$ is exponentially distributed with mean $2\sigma_g^2$.

4.5.4.3 Suitability of method for NCDs

It is now demonstrated that the two conditions outlined in §4.5.4.1 are satisfied approximately by NCD noise, and that $\mu_e = 2\sigma_g^2$ holds. A single string was picked at random for convenience. The present study concerns $\sim 2,000$ linearized pulses (mostly neutrons) from string 29, recorded during the AmBe source calibration runs 50074 and 50076. The last 4,096 bins of each pulse are taken as a noise ‘event’.

(a) Independence of X_i and Y_i

Fig. 4.10 shows no evidence of any correlation between real (X) and imaginary parts (Y) of frequency amplitudes for neutron pulses from string 29. The top two figures (A and B) illustrate the behaviour of these two variables at a single frequency (10 MHz) for a large number of noise events. It is observed that the phase Φ_i is uniformly distributed in the range $(-\pi/2, \pi/2)$, and the correlation coefficient between X and Y fluctuates randomly around 0 at the 80 frequencies investigated (from 10 to 150 MHz). In this particular example, the average correlation coefficient for all frequency values is slightly positive at 0.007, with an RMS of 0.05.

(b) X_i and Y_i are Gaussian-distributed around 0, with the same standard deviation

Fig. 4.10D shows the distributions of X_i (blue histogram) and Y_i (black histogram) at a frequency of 10 MHz, fitted to Gaussian functions. The χ^2 fit probabilities are 0.05 and 0.15, respectively. The means are consistent with 0, and the standard deviations agree within fit errors. Fig. 4.10E shows the equivalence of σ_p obtained from Gaussian fits to both $P(X_i)$ and $P(Y_i)$ over a wide range of frequencies (10–150 MHz). Thus, X_i and Y_i can be sampled from the same distribution.

(c) $P(\Omega_i)$ is exponential with mean $2\sigma_g^2$

Fig. 4.10F is an example of the typical exponential form of $P(\Omega_i)$. Again, a frequency of 10 MHz is used as an illustration. As a result of (a) and (b) above, the relation $\mu_e = 2\sigma_g^2$ is approximately satisfied across a wide frequency range, as shown in fig. 4.11.

Therefore, the method described in §4.5.4.1 is applicable to NCD noise.

4.5.4.4 Stability of NCD noise

Electronics calibration runs were used to extract the average noise power spectra for each string, from April 2005 to the end of 2006 [79]. Strings connected to the same MUX box are found to share approximately the same power spectrum, with box 4 differing significantly from the others because of a different baseline at the log-amplifier input (fig. 4.12).

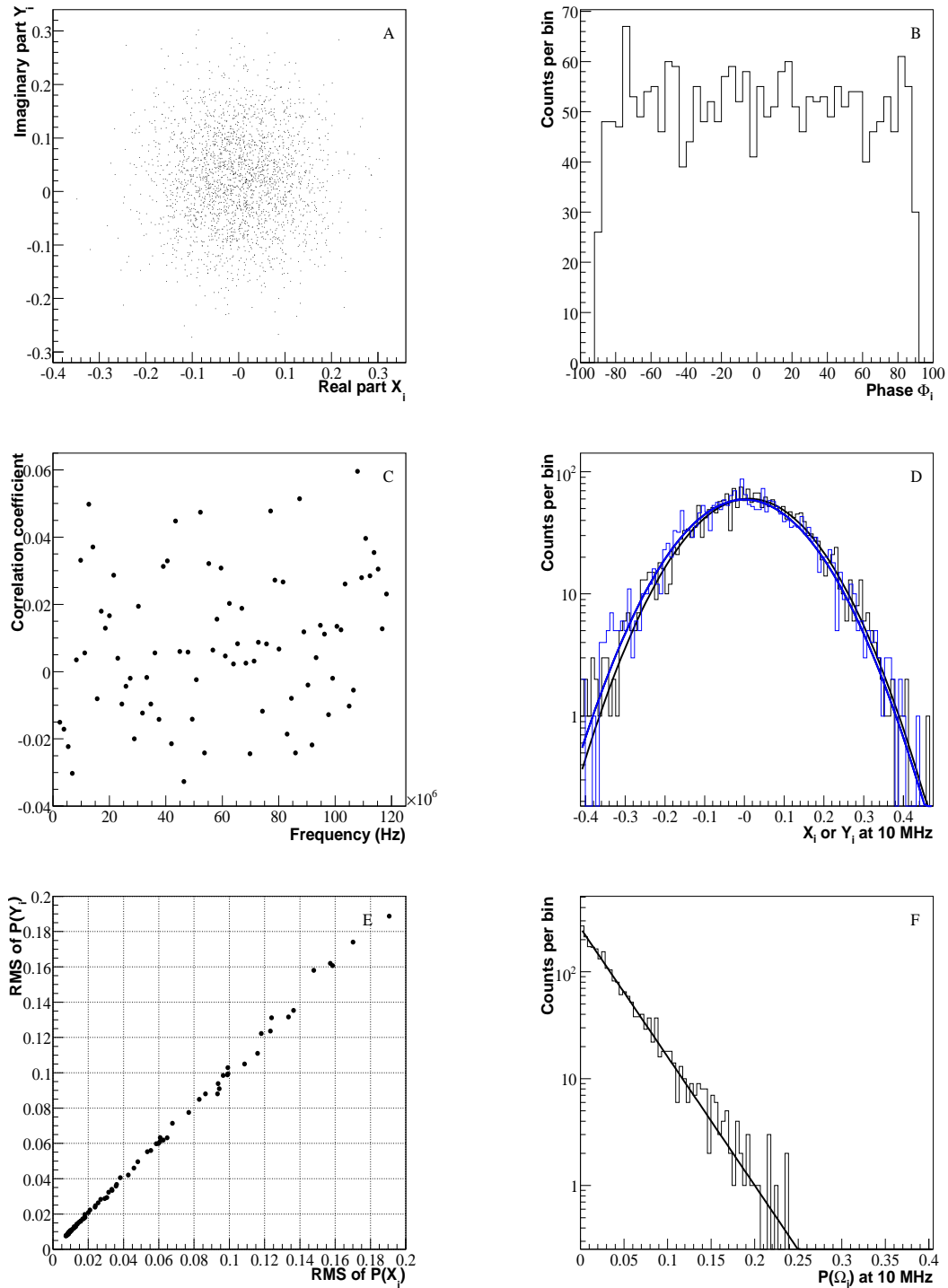


Figure 4.10: A: Scatter plot of X_i vs Y_i at 10 MHz. B: Distribution of the phase angle $\Phi_i = \tan^{-1}(Y_i/X_i)$ at 10 MHz. C: Correlation coefficient between X_i and Y_i as a function of frequency. D: Distributions of X_i (black) and Y_i (blue) fitted to Gaussian functions. E: Equivalence of the RMS of $P(X_i)$ and $P(Y_i)$ in the range 10–150 MHz. F: $P(\Omega_i)$ at 10 MHz fitted to an exponential distribution. The noise traces used for generating these plots come from string 28 in runs 50074 and 50076.

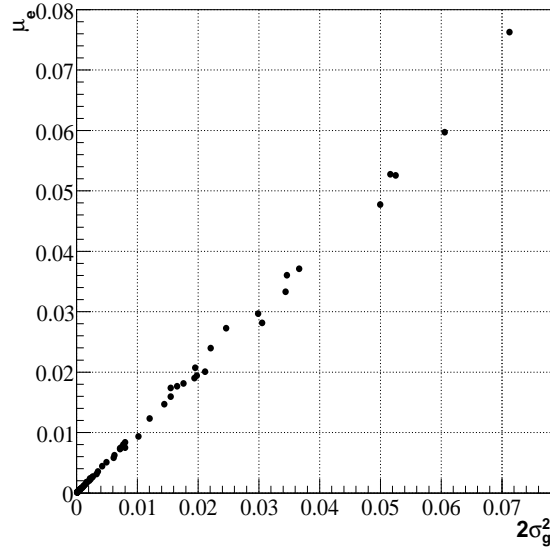


Figure 4.11: At any frequency i , the power $P(\Omega_i)$ is exponentially distributed with mean μ_e , while the real and imaginary parts are Gaussian-distributed around 0 with standard deviation σ_g . This figure shows the approximate equivalence of μ_e and σ_g over the frequency range 10–150 MHz.

It was verified, by means of Kolmogorov-Smirnov (K-S) tests, that power spectra from strings connected to the same MUX boxes retain a consistent shape throughout the experiment. Power spectra from each MUX in 10-day periods were compared to the average spectra from the rest of the data-taking (see fig. 4.12, right). Fig. 4.13 (right) shows the probability (p -value) of spectra, for each 10-day period and from each MUX, being compatible with the average shapes, as a function of time. On a few occasions (7 %) the p -value is less than 0.05. This is consistent with expected fluctuations for the 214 data points shown in this figure.

It was also observed that the noise RMS, calculated using the last 4,000 bins of scope traces, is stable throughout the experiment. Fig. 4.13 (left) shows the time evolution of RMS noise on pulses from each multiplexer box inside the neutron energy window. Dotted lines are RMS values resulting from the default power spectra used in pulse calculations. Pulses from box 4 are noticeably less noisy, compared to those from other boxes.

Thus, the power spectra and RMS of baseline noise on NCD pulses are stable throughout the data-taking period.

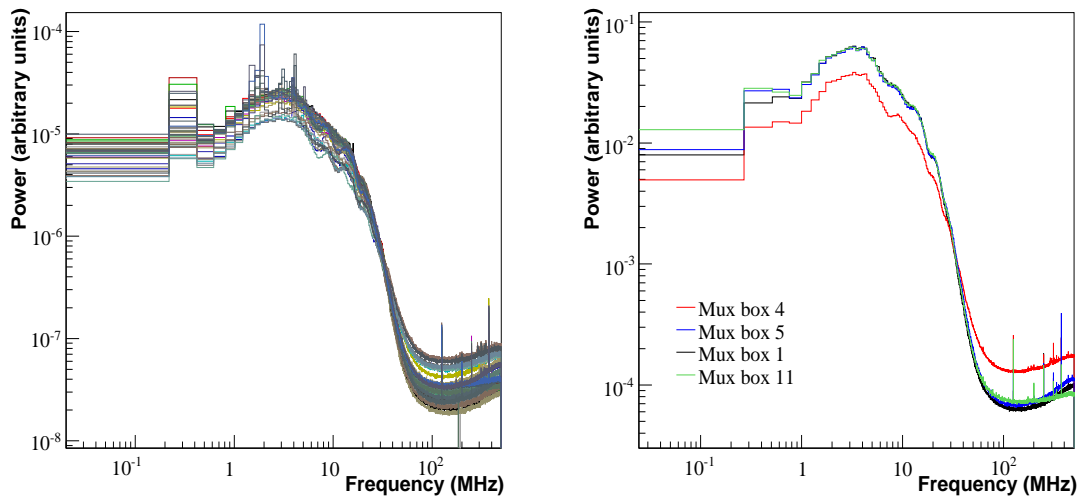


Figure 4.12: Left: Baseline noise power spectra from the 40 NCD strings, averaged over electronic calibration runs. Data kindly provided by A. Cox-Mobrand. Right: Noise power spectra from pulses, grouped by MUX.

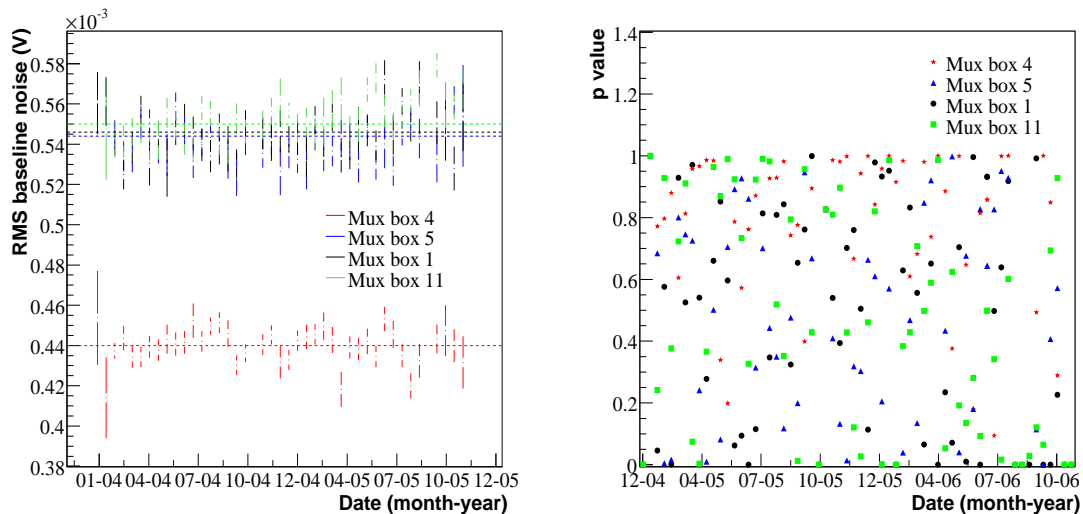


Figure 4.13: Left: the variation of noise RMS with time, on pulses in the neutron energy window that pass the data cleaning cuts. Right: K-S probability of noise power spectra (evaluated for 10-day periods) being compatible with the average shape for the whole data-taking period.

4.5.4.5 Implementation

The method discussed above has been validated for linearized NCD baseline noise. This implies that noise generated from such spectra has to be added to the simulated pulse at point N_3 in the electronics chain (see fig. 4.7). However, the pulse linearization process, which is a simple inversion of Eq. 4.19, does not deconvolve the effects of the $RC = 13.5$ ns filter present after the log-amplifier. In other words, the simulated noise injected at N_3 has already been filtered. Therefore, simulated pulses are log-amplified and passed through the 13.5 ns filter, then linearized before noise is added. The combined pulse is subsequently log-amplified, and the filter skipped before digitization and file output.

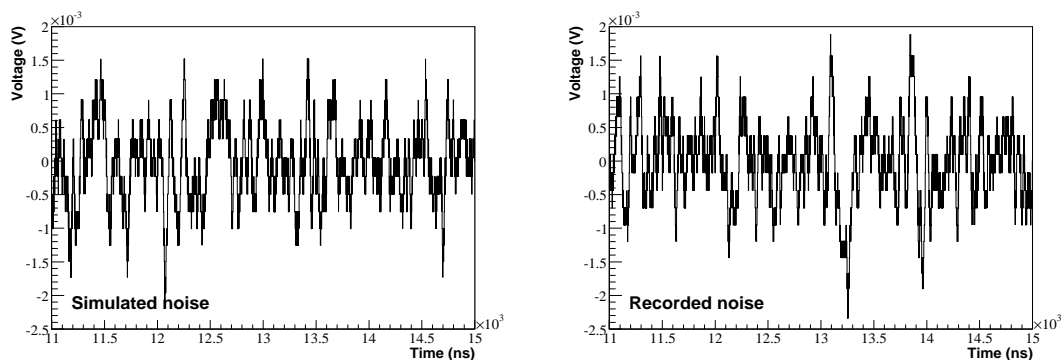


Figure 4.14: Left: Example simulated NCD baseline noise, using the technique developed in this work. Right: linearized baseline noise sample from a recorded α pulse.

Fig. 4.14 shows a simulated 4 μ s noise train (left) compared with a real baseline noise sample (right) from an α pulse. It should be noted that the power spectrum sampling technique described here breaks down, if there were a significant noise source after the log amplifier (*i.e.* at N_4 in fig. 4.7). Should this be the case, noise close to the crest of high amplitude pulses would be different from baseline noise.

4.6 Data-Monte Carlo comparisons

The full NCD Monte Carlo is a rather complex simulation that takes in a large number of input parameters, many of which were not originally known. Assessment of the pulse Monte Carlo performance is an integral part of the code development, because systematic differences between data and Monte Carlo mean at least one of three things:

- (1) Some physics or hardware model is lacking, or deficient.
- (2) There is a coding bug.
- (3) One (or more) input parameter is out of tune.

Direct, pulse-by-pulse comparisons between data and simulation are not feasible. Instead, large samples of pulses are calculated, and a number of pulse parameter distributions, such as those described in appendix D, are extracted. These are then compared with pdfs generated from: (1) ^{24}Na calibration source data (for neutrons), and (2) ^4He string data (for α events).

Identifying and correcting the source(s) of discrepancies between data and simulation can be very time-consuming. A simple rule of thumb for mitigating data vs MC differences in any pulse parameter distribution is as follows. The program is first revised for any coding mistakes. If nothing suspicious is found, input variables that have a clear and strong impact on the pulse parameter, are varied within reasonable bounds. If the same disparities are still apparent, the model itself is to blame, and new features will probably have to be introduced.

As an example, fig. 4.15 (A–F) shows Monte Carlo calculations of the neutron pulse parameter $pw50$ (or FWHM), at different stages of the code development, compared to data (in red). The effects of successive model upgrades on this parameter are shown, with results from the final code version in F and columns 3 and 4.

4.6.1 Neutron pulse shape parameter distributions

The performance of the latest code version is illustrated in figs. 4.15 (F and columns 3 & 4) & 4.16. Most of the Monte Carlo generated neutron pulse parameters compare well to data. All quantities demonstrate biases to some extent, although differences are more pronounced for variables such as $irt50$, $irt70$, $pw70$ and pulse mean. Possible explanations are given below:

- (1) *Tail of pulses*

The tail of pulses is currently not well understood. Real pulses decay slower than predicted by the simulation. As mentioned in §4.5.1 (see also fig. 4.8), some pulse reflections might be missing in the model. Variables that involve pulse integrals over

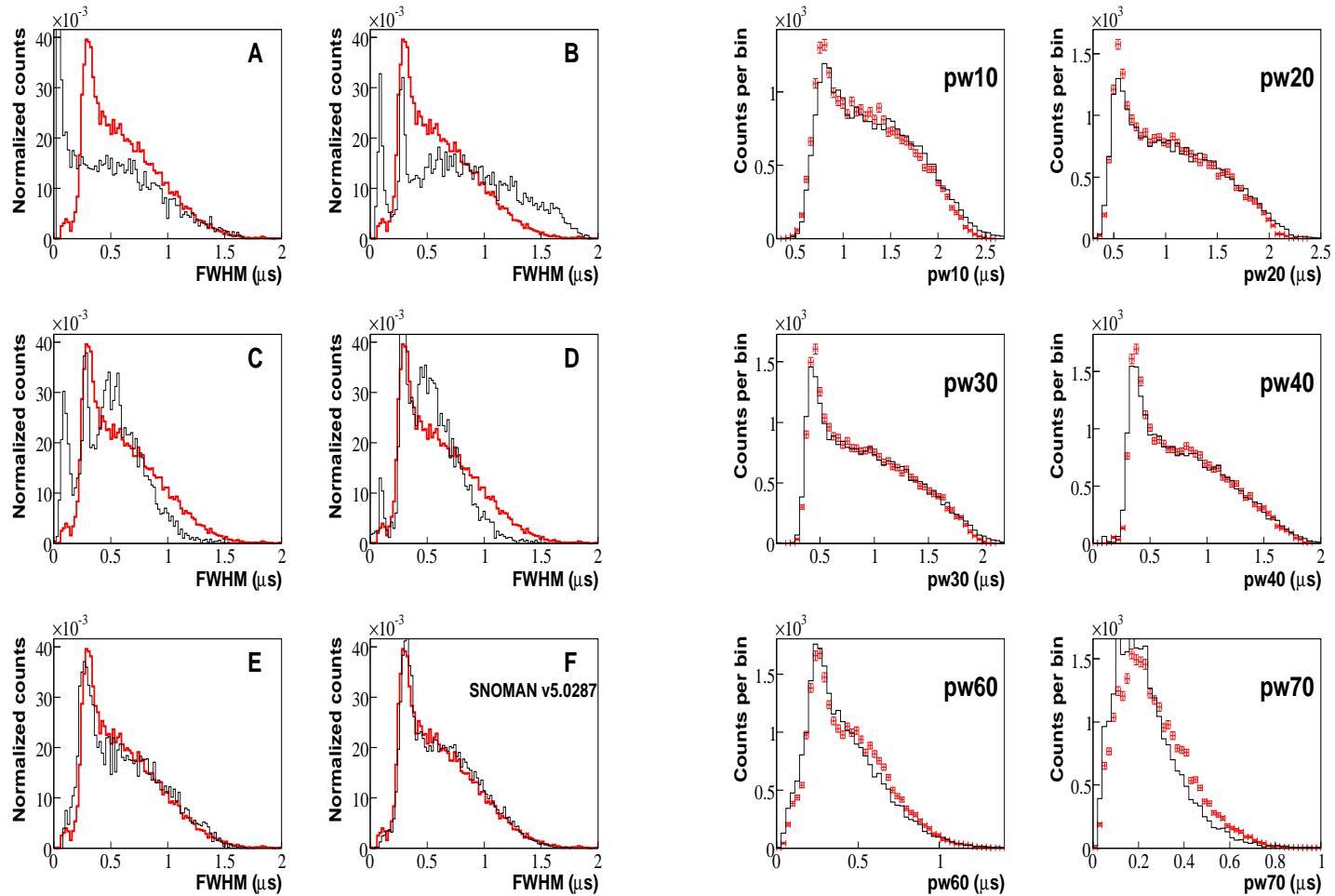


Figure 4.15: First two columns: comparisons of Monte Carlo generated neutron $pw50$, or FWHM distributions (black) with ^{24}Na calibration data (red) at different stages of the Monte Carlo development. **A**: raw pulses with no ion tail and with a drift curve supplied by [43]; **B**: addition of delay line reflection and electronics; **C**: addition of noise; **D**: addition of electron diffusion; **E**: drift curve adjustment and multiple scattering of p - t pairs; **F**: introduction of preamplifier reflections. Columns 3 and 4 show other width fractions calculated with the latest code version. Discrepancies become more significant near the top of pulses.

long time intervals, such as the pulse mean and integral rise-times (*irt50*, *irt70*), are affected as a result. As seen in fig. 4.16, the longer the time interval, the worse the disagreement. These discrepancies were not further investigated because most analyses focus on the main part (*i.e.* the first $\sim 2 \mu\text{s}$) of pulses.

(2) *Noise near pulse maxima*

Differences between data and MC in *pw70* are likely to be caused by the noise close to the crest of pulses not having the same RMS and frequency properties as baseline noise¹¹. Noise has a significant impact on pulse widths, as can be seen in fig. 4.15C.

(3) *Hardware modelling*

Systematic differences appear in pulse moments and widths, *e.g.* the Monte Carlo *m3* (pulse skewness) distribution appear distorted compared to data. These are caused by the different electronic properties of one particular MUX (box no.4), compared to the other boxes. MUX differences are currently not properly accounted for in the simulation. Monte Carlo predictions, in general, lie between the typical shapes for box 4, and the other boxes. Fig. 4.17 illustrates the disparities between box 4 and boxes 1, 5, 11 in pulse moment and width variables.

Empirical corrections can be rather straightforwardly applied to the MC pdfs of a number of pulse shape parameters. Improvements to the pulse simulation itself, however, will require more detailed studies of the issues discussed above.

4.6.2 Low energy α pulse shape parameter distributions

In principle, the calculation of α pulses in the neutron energy range should be as accurate as for neutrons, *i.e.* one naively expects the same level of agreement as in figs. 4.15 & 4.16, including issues (1)–(3) pointed out in the last section. However, further complications arise for the following two reasons:

(1) *A variety of α event types*

Simulated pulse parameter distributions for each α event class have to be mixed in the correct proportions in each string, before comparing with data. The relative

¹¹This also affects the acceptance of some data reduction cuts when applied to the MC [65].

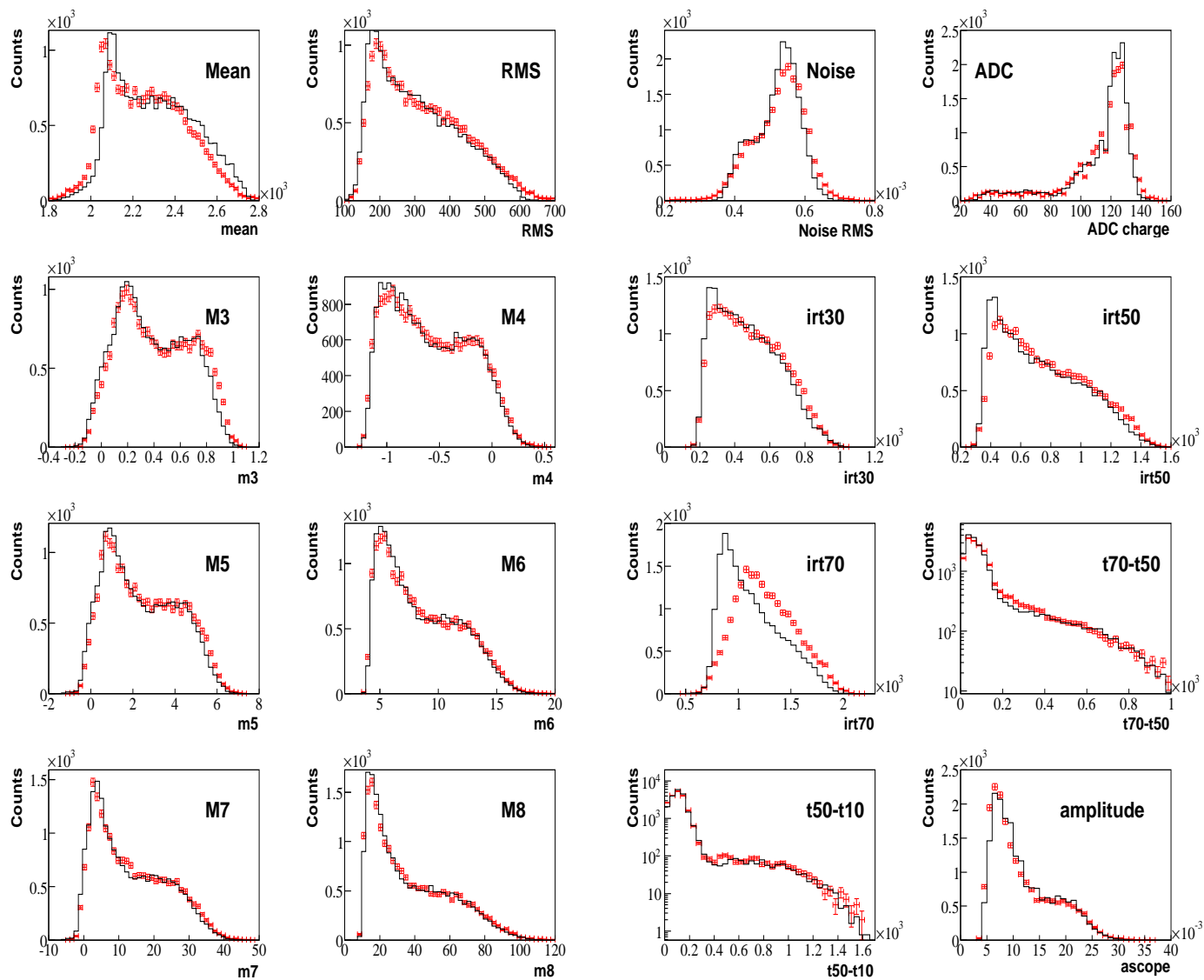


Figure 4.16: Simulated neutron pulse parameter distributions (black) compared to ^{24}Na calibration neutrons (red). Parameters are defined in appendix D. Possible reasons for biases are discussed in the text.

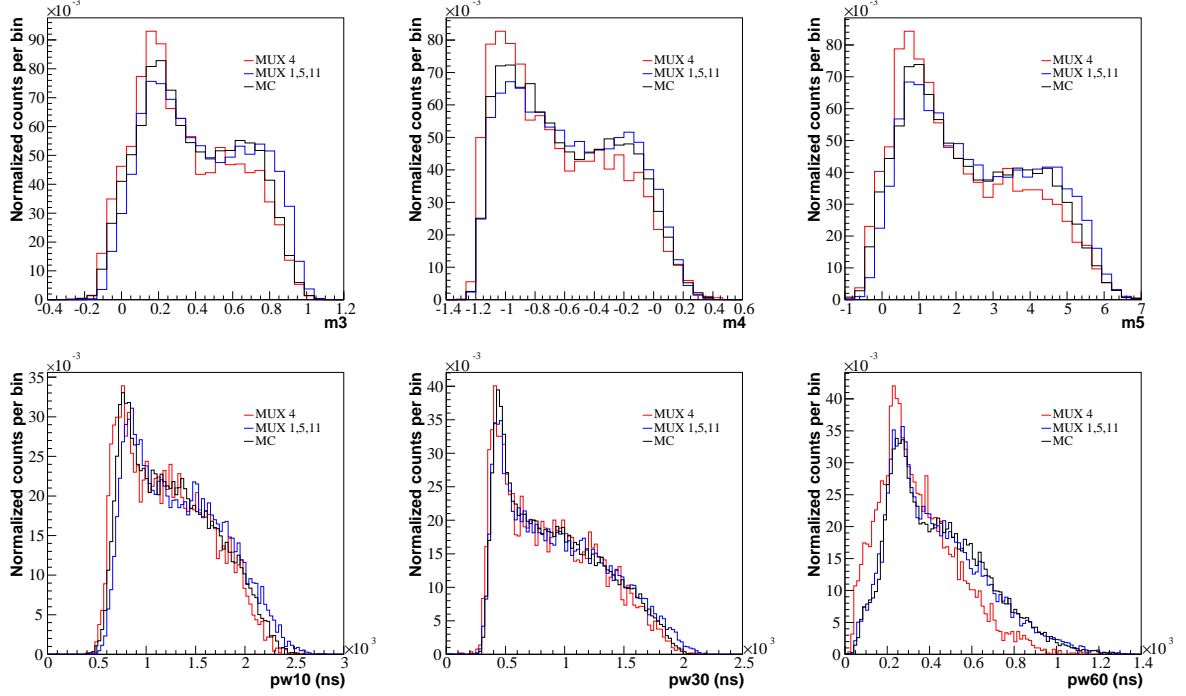


Figure 4.17: First row: biases on neutron pulse moment distributions arising from the different electronic properties of the four MUX boxes. Blue: Boxes 1,5 and 11. Red: Box 4. Black: Monte Carlo. Box-by-box differences are not accounted for in the simulation, and all four boxes in the Monte Carlo produce distributions close to the black curves. Second row: MUX biases on pulse widths.

fractions of the main α species (^{210}Po , ^{238}U , ^{232}Th) can be estimated, for example, by fitting energy spectra.

(2) *Non-uniformity of α -emitting impurities in nickel*

The energy distributions of α particles entering the gas depends strongly on how impurities are distributed in the walls. If bulk impurities are concentrated towards inner NCD surfaces, on average, alphas exit counter walls with more energy, resulting in a large number of narrow pulses in the neutron energy window. Thus, one has to characterize these impurity distributions, and estimate their mean depths \bar{d} .

The impact of \bar{d} uncertainties on the shape of α pulse parameter distributions is overwhelming. For example, fig. 4.18 shows the change in shape of the skewness and FWHM distributions of ^{238}U alphas appearing in the neutron energy window with \bar{d} , assuming an exponential impurity depth profile for convenience. An increment of just $1 \mu\text{m}$ has a significant impact on the shape of m_3 at low \bar{d} . Therefore, in order to

reach a satisfactory level of agreement with α data, a reliable pulse calculation scheme is not sufficient: accurate values of \bar{d} , as well as ^{238}U , ^{232}Th and ^{210}Po α fractions, are also required for *each* string. An alternative way of representing certain α distributions, which does not require any knowledge of \bar{d} , is discussed in detail in chapter 6. Data-MC comparisons will then be made using that representation.

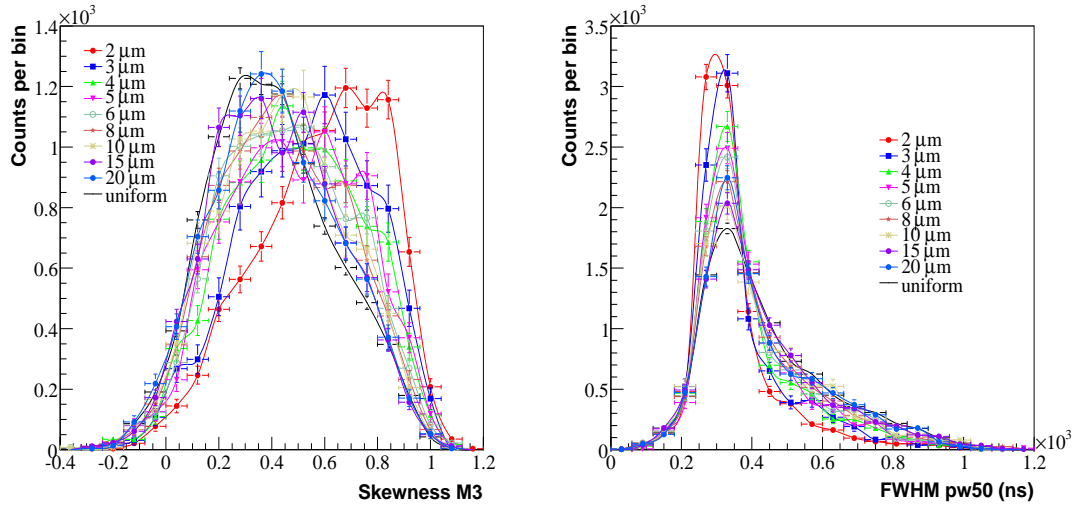


Figure 4.18: Change in shape of ^{238}U $m3$ (right) and $pw50$ (left) distributions with mean impurity depth \bar{d} .

4.7 Non-standard α pulses

4.7.1 Wire α events

Comparisons of simulated pulse width-energy space to data (*e.g.* fig. 4.23) led to the identification of wire α events. A number of α particles originating from NCD anodes produce pulses that have distinctly different shape parameters (*e.g.* skewness, kurtosis and higher moments) compared to other known classes. In particular, the width of these pulses at some fraction of the amplitude can be much larger than the other types, because more charge is being collected towards the end of the pulse. One such event, observed in the data, is displayed in fig. 4.19 (left). The back of the pulse is clearly elevated compared to an α particle emanating from the wall (middle figure). A simulated wire α event that reproduces this peculiar waveform is shown on the right.

Estimates of the percentage content of wire α events in each string have been made,

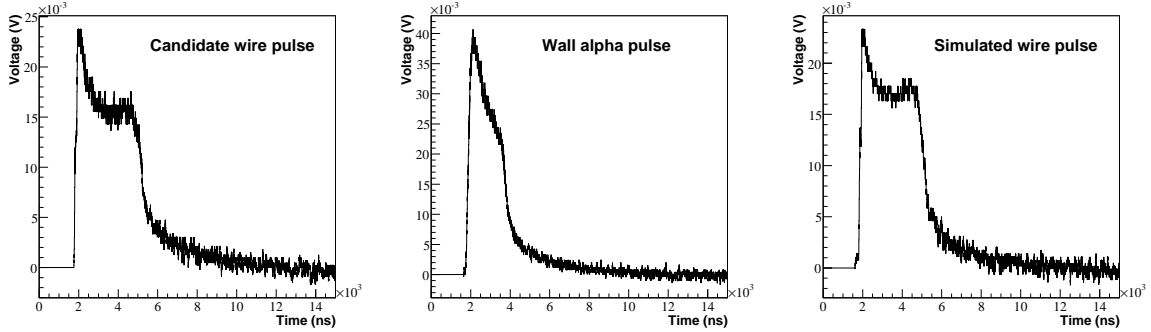


Figure 4.19: A 4.58 MeV wire α candidate (left) observed on string 35 (in run 50362, GTID 88620), compared to a typical wall α candidate (middle), and a simulated surface ^{210}Po wire α (right).

using a simple pulse width cut. It is found that around 2 % of all alphas from the array come from the NCD wires. Since this considerably exceeds any expected activity from ^{238}U and ^{232}Th daughters within the wire material (Cu), one has to assume that these alphas originate from the decay of impurities deposited on the anode surface. MC simulations of pulse width-energy space strongly suggest that wire alphas are predominantly from the decay of surface ^{210}Po . For example, in fig. 4.23 (right) it is seen that MC ^{210}Po wire alpha events (in green), can be identified with the candidate wire events (above 3000 ns), in the data (fig. 4.23, left). Bulk ^{238}U or ^{232}Th wire alpha events, on the other hand, do not produce a band at 4.8 MeV.

4.7.2 End-effect α events

The electric field inside NCDs is assumed to be perfectly cylindrical, although distortions are present at the ends of each counter. The purpose of the silica wire connectors (fig. 2.1) is to create multiplication-free regions in areas where field distortions are the most severe. A number of neutron and α pulses are affected by this setup. The respective fractions can be estimated by means of a simple geometric calculation. Fig. 4.20 shows the equipotential lines near a counter end-cap, calculated for a wire connector of length 2.69 cm [83]. The red line is the electron drift line reaching the end of the quartz connector. This is approximated by a straight line of gradient m in the (r, z) plane for simplicity. Assuming a p - t track length of ~ 1.2 cm, all neutrons capturing in zone A will not be observed, whereas those in D (and beyond) will be observed as normal pulse shapes. Neutrons capturing in zones B or C can produce tracks with a number of electrons drifting onto

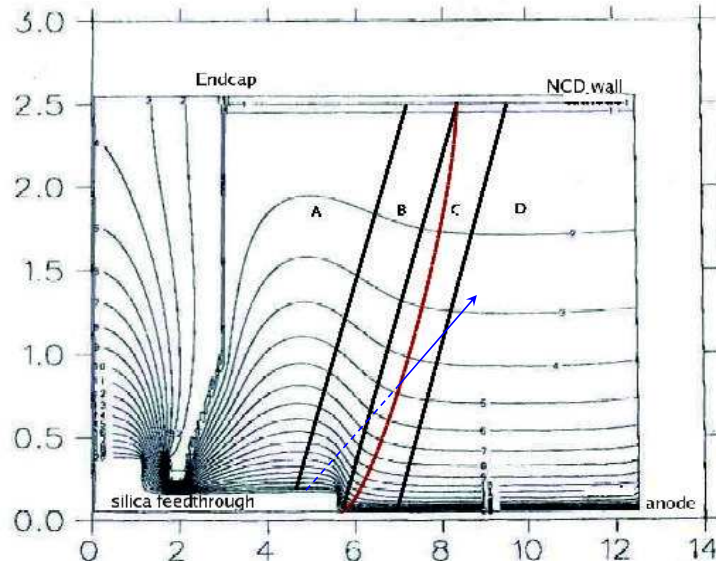


Figure 4.20: Field map near counter endcaps. The vertical axis is the radial distance (cm) from the wire, while the horizontal axis denotes z position (cm) (Picture and field calculation courtesy of A. Poon).

m	0.0	0.6	1.2	1.8
invisible	2.68 ± 0.08	3.55 ± 0.05	4.11 ± 0.10	5.20 ± 0.11
distorted	0.46 ± 0.03	0.50 ± 0.03	0.68 ± 0.04	0.90 ± 0.05

Table 4.3: Expected percentages of invisible and distorted neutron events in the NCD array.

the wire connector, resulting in non-standard pulse shapes.

Table 4.3 shows the expected percentage of all NC neutrons events in the whole array that are not observed, or produce a distorted pulse. A value of $m \sim 1.2$ seems to be closest to the red line in fig. 4.20. A negligible percentage ($< 1\%$) of neutron pulses are predicted to have a non-standard shape, while $\sim 4\%$ of neutrons ionize the gas, but are not expected to produce any detectable signal (*i.e.* they are ‘invisible’). Uncertainties quoted in the table are statistical only.

Rough estimates of the percentages of invisible and distorted α events were also computed, as a function of the initial α energy in counter gas (fig. 4.21). Events are assumed to be uniformly distributed along z , and a string of average length is adopted in calculations. Results are expected to vary by $\pm 5\%$ from string to string because of differing lengths. It is seen that the fraction of distorted events rises with energy on

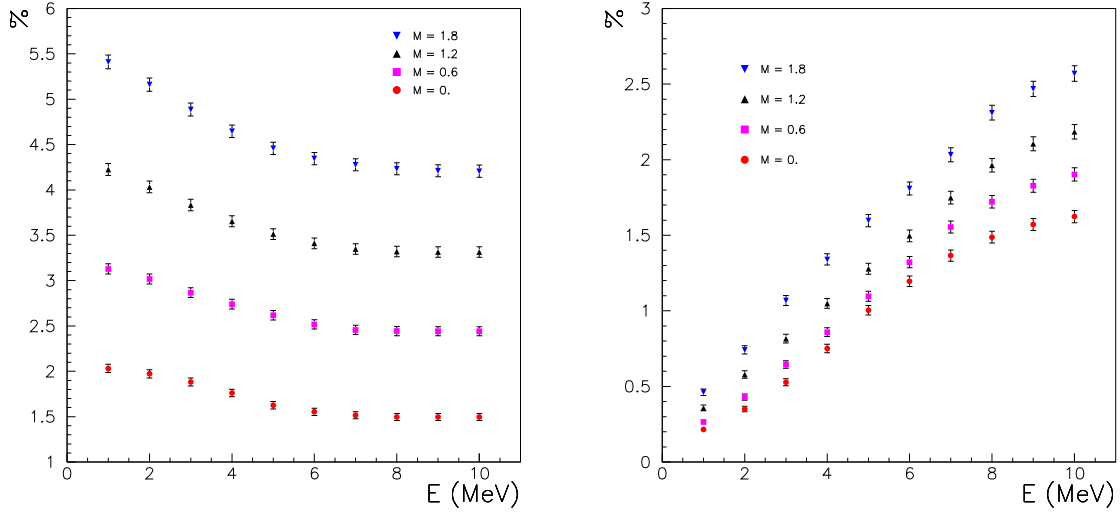


Figure 4.21: Percentage of invisible (left) and distorted (right) α events in the average NCD string, as a function of the initial energy in the gas. Impurities are assumed to be uniformly distributed along the z direction.

m	0.0	0.6	1.2	1.8
invisible ^{238}U	1.78	2.82	3.82	4.93
invisible ^{232}Th	1.75	2.78	3.77	4.87
invisible ^{210}Po	1.62	2.63	3.57	4.60
distorted ^{238}U	0.50	0.59	0.74	0.98
distorted ^{232}Th	0.56	0.67	0.81	1.06
distorted ^{210}Po	0.82	0.92	1.01	1.39

Table 4.4: Estimated percentages of invisible and distorted ^{238}U , ^{232}Th and ^{210}Po α events in an NCD string of average length. Statistical uncertainties are of the same order as in table 4.3.

account of longer particle tracks. This implies that fewer tracks are fully-contained in regions A and B combined, resulting in a decrease in the percentage of invisible events with energy.

After folding in appropriate energy spectra, the expected fractions of end-cap ^{238}U , ^{232}Th and ^{210}Po α events are straightforwardly obtained (table 4.4¹²). Again assuming $m \sim 1.2$, it is estimated that $\sim 1\%$ of all α events have some of their ionization electrons collecting on the quartz. A number of these events can have very distinctive features. Because part of the track is not observed, in some cases, the resulting pulse might look

¹²The calculations assume non-embedded ^{210}Po , and uniformly distributed ^{232}Th and ^{238}U impurities.

like that of a lower energy α particle starting off in the middle of the counter. This produces very low rise-time events that cannot be produced otherwise. An example is shown in fig. 4.20: the blue line is a high energy α starting from the quartz connector. The first section of the track (dotted blue line) is invisible, which means that the resulting pulse would look like a wire alpha event, but with the leading peak missing. Fig. 4.22 displays a candidate quartz connector α pulse, observed on string 16.

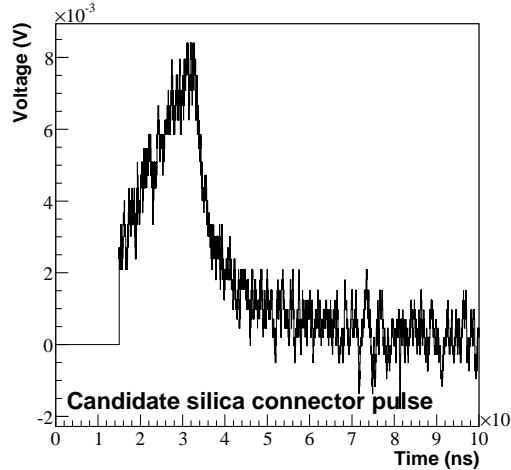


Figure 4.22: An α event (GTID 16027), with an energy of 1.16 MeV, suspected to originate from one of the silica wire connectors on string 16.

In addition, end-cap pulse shapes are expected to be significantly broadened, since drift times are extended because of lower field strengths (examples of these pulses can be seen in appendix H). Events might also be shifted down in energy because of reduced gas gains in non-cylindrical fields. Such complications make these distorted events, which can mimic neutron pulse shapes¹³, very difficult to simulate accurately.

4.8 Summary

This chapter described the various steps in the numerical simulation of NCD pulses: (1) generation of particle trajectories and ionization electrons, (2) calculation of the induced current on the anode, (3) the effects of NCD hardware, and (4) the inclusion of baseline noise. The method for calculating the pulses applies to any ionization event. Comparisons

¹³Data taken with high-rate α sources led to the belief that a background-free neutron region exists in width-energy space [84]. Over time, however, this region becomes peppered with distorted α events.

with data are made, and very good agreement is achieved in the case of neutrons. These comparisons allows one to identify wire and end-cap alphas. Distorted α events, which constitute around 1 % of all alphas, are at present not simulated properly. The different species of ionization events are illustrated in fig. 4.23, which shows how neutrons, and the known classes of alpha backgrounds populate the $pw40$ -energy parameter space, across the entire energy range.

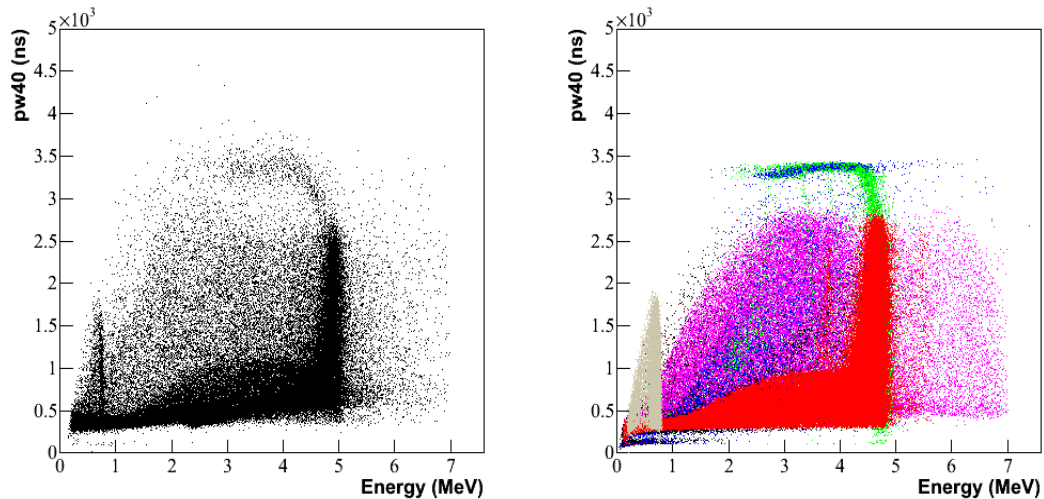


Figure 4.23: Scatter plots of $pw40$ vs energy for neutrons, and the different classes of α events. Right is MC, and left is data. Magenta: bulk alphas; red: wall ^{210}Po alphas; grey: neutrons; blue: wire ^{238}U alphas; green: wire ^{210}Po alphas; black: bulk alphas in the end-cap region.

Chapter 5

Simulation of NCD Energy Spectra

The computation of ${}^3\text{He}$ proportional counter neutron, α and β spectra is now addressed. This is not merely a matter of integrating simulated pulse shapes. To accurately calculate the measured energy of any NCD ionization event, careful consideration has to be given to the following problems:

- (1) What is the energy of the particle as it enters the gas? (*i.e.* how much energy did it lose *before* entering the gas?)
- (2) How much energy is lost in the gas itself? (see §4.3.1)
- (3) How does the energy deposited in the gas relate to the measured energy?

Given accurate stopping power tables, the initial particle position in the gas¹, and a robust track-tracing algorithm, the second problem can be solved fairly easily, and will not be discussed further. This chapter focusses on the major issues governing (1) and (3), including: the distribution of Po, U and Th impurities in NCD walls (§5.5.1, §5.5.2), energy resolution (§5.3), and the simulation of space charge effects (§5.2), after a brief discussion of the mean NCD gas gain (§5.1). Characteristics of NCD neutron and ${}^{210}\text{Po}$ alpha energy spectra, such as peak skewness and ledge-shaped features, are explained quantitatively using the space charge model (§5.2.4). Calculated α energy spectra are compared to data and used to estimate the background contents of NCD strings (§5.6). Simulated β energy spectra are also presented (§5.7), with estimates of β event rates given in §5.7.1.

¹Neutrons: capture positions in NCDs are calculated with the MCNP code [85]; alphas and β particles: these start at the edge of the gas.

5.1 Gas gain

The mean NCD gas gain \bar{G} is well described by the Diethorn formula:

$$\ln \bar{G} = C \frac{\lambda \ln 2}{2\pi\epsilon_0 \Delta V} \ln \left[\frac{\lambda}{2\pi\epsilon_0 a E_{min}} \right] \quad (5.1)$$

where ΔV denotes the mean ionization energy, E_{min} the minimum electric field to start an avalanche, λ the anode charge density, a the anode radius and C is a constant. The Diethorn model assumes a simple doubling process in the avalanche mechanism. Fig. 5.1 illustrates the very good agreement between the NCD gain (in green markers) and Eq. 5.1, with a suitable value for C .

For 85:15 $^3\text{He-CF}_4$, the Diethorn parameters were measured by Hime [86] to be $\Delta V = 34$ eV and $E_{min} = 48750$ Vcm $^{-1}$. An effective avalanche radius r_{av} can be defined from E_{min} as follows²:

$$r_{av} = \frac{V}{\ln(b/a) \cdot E_{min}} = 57.9 \mu\text{m} \sim 2a \quad (5.2)$$

where the anode voltage $V = 1950$ V. This is of the same order as the e $^-$ transport MC prediction, which is 33 μm (see §3.3.4).

5.2 Simulation of space charge effects

5.2.1 Motivation

Under operating conditions (1950 V), the gas gain is high enough so that the shielding effects of ions formed in electron avalanches close to NCD anodes are non-negligible. The local electric field is attenuated, resulting in lower amplifications and pulse shape distortions³.

The impact of these *space charge effects* on energy distributions is very significant. Some of the main consequences are:

(a) Skewed peaks

²Strictly speaking, r_{av} , as defined in Eq. 5.2, is the maximum radius at which charge multiplication can occur.

³One only needs to consider avalanche ions created in the *same* event. Since ions collect at the cathode within ~ 1.1 ms, and given the low total event rate of 0.15 Hz, previous ionization events do not have any bearing.

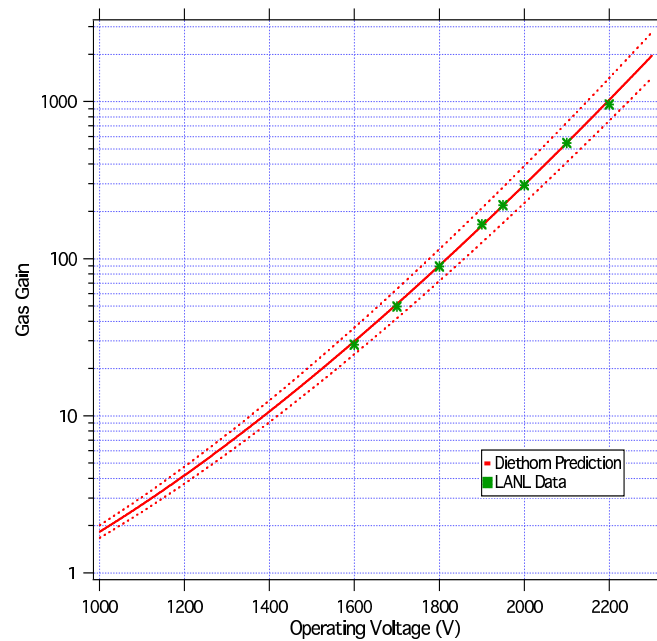


Figure 5.1: Scaled Diethorn formula (solid red curve) compared to NCD data (green markers). Figure kindly provided by K. Rielage.

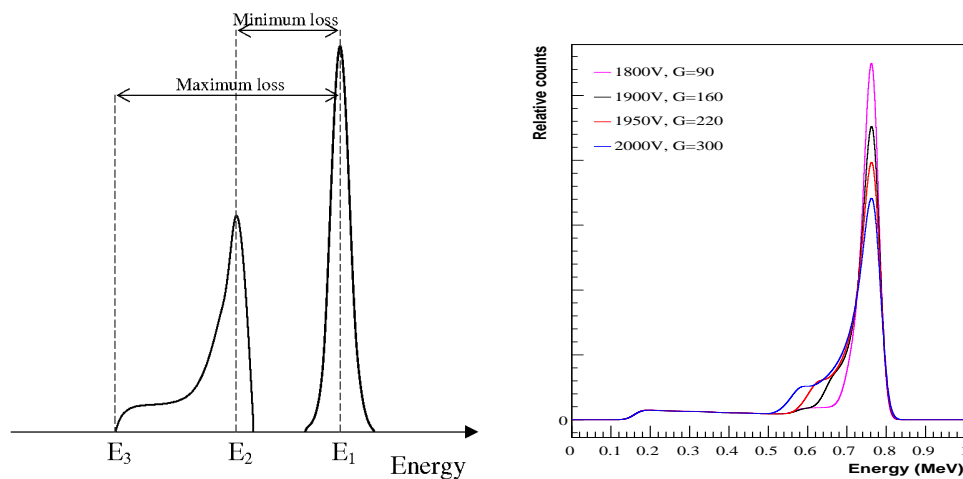


Figure 5.2: Left: Effects of space charge on mono-energetic spectral peaks. In the presence of space charge, a symmetric peak at E_1 is shifted down to E_2 . The peak becomes skewed, and a ledge at E_3 appears, marking the point of maximum gain loss. For neutrons, E_2 is *calibrated* to 764 keV and $E_3 \sim 600$ keV. For ^{210}Po alphas, using an energy scale calibrated with the neutron peak, $E_1 = 5.3$ MeV, $E_2 = 4.8$ MeV, and $E_3 \sim 2.3$ MeV. Right: Simulation of the effects of increasing the anode voltage (or gas gain) on the shape of the neutron energy spectrum (all peaks are scaled to 764 keV). The neutron peak is distorted as in the figure on the left.

All mono-energetic peaks are skewed towards lower energies (*e.g.* the 764 keV neutron peak), the more so if the anode voltage is increased. Conversely, as the gain is reduced, the peak becomes more symmetric. This is illustrated in fig. 5.2.

(b) *Spectral distortions*

It is observed that the energy spectrum of neutron events contains a step-like feature at ~ 600 keV (figs. 2.4 and 5.2). Similarly, the ^{210}Po alpha energy spectrum has a ledge at 2.3 MeV⁴. It is shown in §5.2.4 that these peculiarities are indicative of the *maximum* gain change of fully-contained *p-t* and 5.3 MeV ^{210}Po alpha tracks at 1950 V, as a result of space charge effects⁵.

(c) *Non-linearity of energy scale*

The energy scale appears non-linear, when the calibration of shaper-ADC bins is done by using neutron energy spectra. The ^{210}Po peak is observed to be shifted from 5.3 MeV down to ~ 4.8 MeV by 9.4 %. This occurs because the *minimum* gain change due to space charge effects does not vary linearly with energy.

(d) *Low-energy background spectra*

Predicted energy distributions of alpha particles from the nickel demonstrate a high number of counts at low energies, which are not observed in the data (see a rough analytic derivation in appendix F, and also fig. 6.3 of [87]). Bulk α energy spectra calculated with a tuned space charge model do not exhibit this feature.

Space charge effects in ^{210}Po alphas events stand out very strongly with the parameter $\frac{m_5}{m_6}$ ⁶, which separates tracks that hit the counter walls from fully-contained ones. Fig. 5.3 (left) shows $\frac{m_5}{m_6}$ plotted against energy, for background events between 1 and 6 MeV. The dense band in the red box are ^{210}Po events where the alpha particle run into the cathode, while the band in the blue box are events that are fully-contained. The prediction of a Monte Carlo simulation of pulse shapes, in the absence of space charge

⁴This was first pointed out by McGee.

⁵Wall effects produce plateaus in pulse height distributions [63], and one can be tempted to think that the ~ 600 keV step in the neutron spectrum is a corollary. It will be demonstrated in §5.2.4 that this is not the case.

⁶ m_5 and m_6 are the 5th and 6th moments of the pulse, respectively. Formal definitions of pulse parameters are given in appendix D. The value of $\frac{m_5}{m_6}$ is large at high θ , where space charge effects are sizable.

effects, is shown in fig. 5.3 (middle). The corresponding simulation that includes space charge effects, is shown on the right. The appearance of fully-contained events (where 5.3 MeV worth of charge is deposited), in the energy range 2.3–5 MeV, offers compelling evidence for a gain loss mechanism.

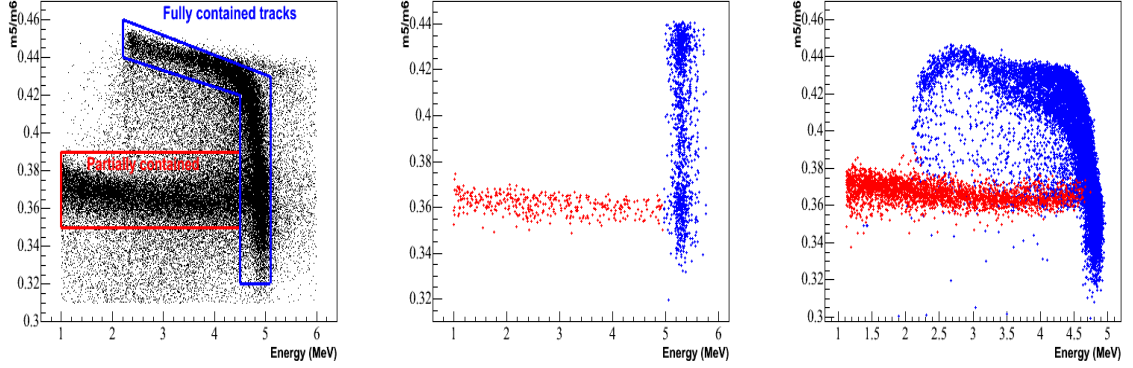


Figure 5.3: $\frac{m_5}{m_6}$ for background events above 1 MeV. Left: data, with ^{210}Po events forming the dense bands. Middle: Monte Carlo simulation of ^{210}Po alpha pulse shapes, without space charge effects. Fully-contained tracks are shown in blue, while those incident on the walls are in red. Right: simulation, with space charge effects included.

Thus, the inclusion of space charge effects is essential to properly model pulses and their integrated charges.

5.2.2 Simulation method

A two-parameter model that accounts quantitatively for the phenomena (a)–(d) discussed in the previous section was developed and integrated within the pulse simulation. This model builds on the Diethorn formulation, which is a good description of the NCD gas gain (§5.1).

Consider a cluster of ions of total charge q formed in an electron cascade close to the wire, located at a mean radius \bar{r} . The charge induced by these ions on the anode modify the wire charge density locally. From Eq. 5.1, the change in gas gain δG resulting from a change in wire charge density $\delta\lambda(\bar{r})$ is

$$\delta G \propto \bar{G} \left(\ln \bar{G} + \frac{C \lambda \ln 2}{\Delta V 2\pi \epsilon_0} \right) \frac{\delta\lambda(\bar{r})}{\lambda} \quad (5.3)$$

$$\propto \bar{G} \ln \bar{G} \frac{\ln[b/a]}{2\pi \epsilon_0 V} \left(1 + \frac{1}{\ln[r_{av}/a]} \right) \delta\lambda(\bar{r}) \quad (5.4)$$

with r_{av} defined in §5.1. $\delta\lambda$ is obtained by dividing Eq. 4.3 by a characteristic shower width \mathcal{W} , which, for simplicity, is assumed to be constant:

$$\delta\lambda(r) = \frac{q \ln(b/\bar{r})}{\mathcal{W} \ln(b/a)} \quad (5.5)$$

Electrons originating from some segment of a particle track also see the density changes $\delta\lambda_j$, brought about by ions formed in previous electron cascades. Each of these ion clusters moves slowly towards the cathode while the primary electrons are being collected. In the presence of many ion clusters, the total change in the anode charge density at time t , suffered by the i^{th} track segment is therefore:

$$\delta\lambda_i = \frac{e}{\mathcal{W}} \sum_{j=1}^{i-1} \frac{\ln[b/\bar{r}_j(t)]}{\ln[b/a]} G_j n_{pair,j} + \frac{e \ln[b/\bar{r}]}{\mathcal{W} \ln[b/a]} n_{pair,i} \quad (5.6)$$

where $n_{pair,j}$ is the number of electron-ion pairs formed in the j^{th} segment, and j loops over all the previous ion clusters, which have moved to different radii $\bar{r}_j(t)$ at time t . $\bar{r}_j(t)$ is solved by integrating the relation $\frac{dr_j}{dt} = \mu_i \mathcal{E}$:

$$\bar{r}_j^2(t) = \frac{2\mu_i V t}{\ln[b/a]} + r_{av}^2 \quad (5.7)$$

where μ_i is the ion mobility and \mathcal{E} denotes the electric field.

A charge segment cannot impact significantly on the gain of another segment if their avalanches are far apart. An electron shower centered at a position z_0 on the wire is only affected by segments collecting within the limits $z_0 - \mathcal{W} < z < z_0 + \mathcal{W}$. For those which do, the common distance between cascades is calculated and the induced charge density weighted by an overlap factor ξ . As an example, a group of electrons collecting at $z_1 < z_0$, with $z_1 + \mathcal{W}/2 > z_0 - \mathcal{W}/2$ has an overlap factor of $(\mathcal{W} + z_1 - z_0)/\mathcal{W}$. Eq. 5.6 should then be rewritten as:

$$\delta\lambda_i = \frac{e}{\mathcal{W}} \sum_{j=1}^{i-1} \frac{\ln[b/\bar{r}_j(t)]}{\ln[b/a]} G_j n_{pair,j} \xi_j + \frac{e \ln[b/\bar{r}]}{\mathcal{W} \ln[b/a]} n_{pair,i} \quad (5.8)$$

The mean gas gain of the i^{th} track segment is, therefore:

$$\bar{G}_i = \bar{G} - \delta G_i \quad (5.9)$$

with the measured mean gain $\bar{G} = 219$. δG_i is evaluated with Eq. 5.3, using Eq. 5.8 as input. As mentioned in §4.1, the actual charge multiplication factor, G_i , applied to the

i^{th} segment is obtained by randomizing the single-electron gas gains using an exponential distribution⁷ with mean \bar{G}_i .

It is implicitly assumed that ions produced in avalanches induce a image charge of uniform density along the wire. Furthermore, it is assumed that \mathcal{W} does not vary with radius. These are crude, but economical and efficient approximations. More realistic charge distributions, such as those discussed in §3.3.4, can be implemented, but at great computational cost and additional complexity.

In this simple numerical model, the two variables that need to be optimized are: (1) the constant of proportionality in Eq. 5.3, which will hereafter be referred to as η , and (2) the avalanche width \mathcal{W} . These two quantities share a strong inverse correlation. The optimization of η and \mathcal{W} is described in the next section. Other required physics input parameters, such as G , μ_i , ΔV and r_{av} , have been constrained independently (see table 5.1).

variable	symbol	value	Ref.
Mean gas gain	G	219	[43]
Ion mobility	μ_i	$1 \times 10^{-8} \text{ cm}^2 \text{ ns}^{-1} \text{ V}^{-1}$	[65]
Mean ionization energy	ΔV	34 eV	[86]
Avalanche radius	r_{av}	58 μm	§5.1

Table 5.1: Space charge model fixed input values.

5.2.3 Model optimization

The parameters \mathcal{W} and η are scaled according to these three observations, which are strongly dependent on space charge effects:

- (1) The ^{210}Po peak position relative to the neutron peak
- (2) The position of the space charge feature in ^{210}Po spectra relative to the ^{210}Po peak
- (3) The shape of the neutron spectrum

To account for (1)–(3), different values of \mathcal{W} and η had to be used for neutrons and ^{210}Po alphas, which implies that at least one of the two parameters varies with energy.

⁷In accordance with the charge distribution simulations presented in §3.3.4.

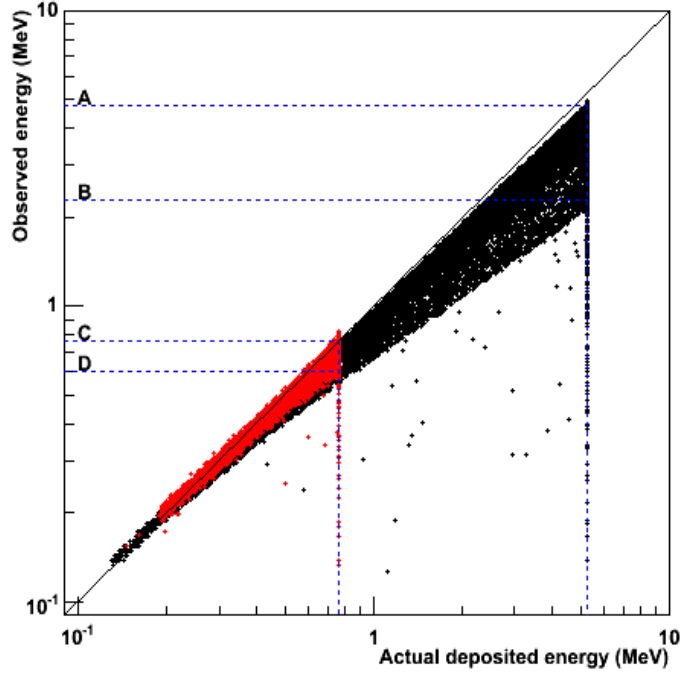


Figure 5.4: Simulation of shaper energy as a function of actual energy loss for neutrons (red), and ^{210}Po alphas (black). The values of A , B , C and D are known from the data (see text). The space charge parameters \mathcal{W} and η are scaled such that $A/C = 6.4$, $B = 2.3$ MeV and $D \sim 600$ keV.

Here, η is fixed, while all the energy dependence is assigned to \mathcal{W} . The following set of values, found through a grid search, satisfy (1)–(3):

$$\mathcal{W} = 154E + 782 \quad , \quad \eta = 1.5 \quad (5.10)$$

with E in MeV. The result of this optimization process is illustrated in fig. 5.4, which is a scatter plot showing a simulation of the ‘recorded’ energy of neutron (red band) and ^{210}Po (black band) events, as a function of the actual energy lost by the particles in NCD gas. The dotted lines, A , B , C and D are the ^{210}Po peak (4.83 ± 0.16 MeV), ^{210}Po space charge ledge (2.3 ± 0.1 MeV), neutron peak (0.761 ± 0.02 MeV), and neutron shoulder (0.60 ± 0.02 MeV) positions observed in the data.

Systematic uncertainties on \mathcal{W} and η can be estimated by looking at how much the ‘recorded’ energies of neutron and ^{210}Po events undergoing maximum gain shift (*i.e.* at a track angle of $\theta = 90^\circ$), vary with these parameters. A change in \mathcal{W} of ± 100 produces $1\text{-}\sigma$ energy shifts in B and C (extracted from the data as ± 0.1 and ± 0.02 MeV, respectively).

An increment of ± 0.1 in η has the same effect. These translate to uncertainties of ± 31 and ± 120 in the gradient and offset of Eq. 5.10.

5.2.4 Model predictions

Some implications of the space charge model, in relation with observations (a)–(c) in §5.2.1, are now discussed. It is first necessary to understand the dependence of space charge effects on track parameters. To quantify space charge effects on a current pulse, one can use the fractional loss

$$\Delta Q = \frac{Q - Q'}{Q} > 0 \quad (5.11)$$

where Q is the total charge of the pulse without space charge, and Q' the total charge with space charge.

It is found that, for both neutrons and alphas, the dominant parameter is the angle of the track with respect to the anode, θ . The effects of other track variables, such as the azimuthal angle ϕ , and the neutron capture radius r_0 , are merely a perturbation around $\Delta Q(\theta)$. In the model, this θ dependence originates from imposing a limited region of influence, $(z_0 - \mathcal{W} < z < z_0 + \mathcal{W})$, to all avalanches along the wire. At high θ , as the track becomes more perpendicular to the anode, there is a high degree of overlap along z between all cascades, so that $\delta\lambda$ is increased greatly, especially for electrons that reach the wire at later times. The weak (r_0, ϕ) dependence is driven by the slow motion of ions: ΔQ is highest for (r_0, ϕ) values that minimize the collection times of electrons. Thus, if ϕ is close to 90° , the track becomes a chord in the radial plane, which means that ions are clustered together radially, maximizing $\ln[b/\bar{r}_j(t)]$ in Eq. 5.6.

Fig. 5.5 (left) is a scatter plot showing the typical dependence of ΔQ as a function of θ for neutrons, for the trial values $\mathcal{W} = 500 \mu\text{m}$ and $\eta = 1$. An approximate, analytic expression for $\Delta Q(\theta)$ can easily be derived. Assuming perfectly straight particle paths, the projection of a track on the wire is proportional to $\cos\theta$. ΔQ increases when avalanches overlap more with each other, that is, if $\cos\theta$ decreases. Ignoring the small variations with other track parameters, one can therefore state:

$$\Delta Q(\theta) \approx \frac{1}{p_1 \cos(p_2\theta)} \quad (5.12)$$

where the parameters p_1 and p_2 are constants. The red curve in fig. 5.5 shows Eq. 5.12 with suitable p_1, p_2 values. This relation implies that mono-energetic peaks should be

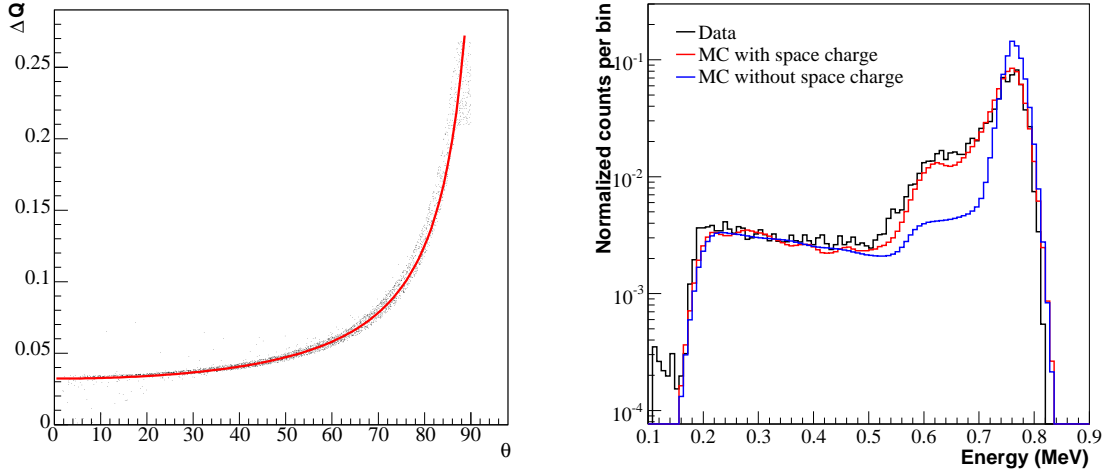


Figure 5.5: Left: the fractional charge loss ΔQ as a function of θ for fully-contained neutrons tracks. Black dots are from a Monte Carlo simulation of pulse shapes with the model discussed in §5.2.2. The tight black band indicates that variations of ΔQ with respect to r_0 and ϕ are small compared to θ . The red line is an analytic approximation (Eq. 5.12) that only assumes θ dependence. Right: calculated neutron spectra with (red), and without the space charge model (blue), compared with data (black). All peak positions are scaled to 0.764 MeV. The same trial parameters \mathcal{W} and η as in the curve on the left were used in the model. It is clear that the wall effect does not account for the shoulder-like feature at ~ 600 keV in the data.

skewed. One can demonstrate this explicitly by deriving an approximate functional form for mono-energetic peaks in the presence of space charge. The following should be true:

$$P(\Delta Q(\theta))d(\Delta Q(\theta)) = P(\theta)d\theta \quad (5.13)$$

where, for instance, $P(\theta)d\theta$ is the probability of getting a pulse between θ and $\theta + d\theta$. Assuming isotropicity⁸ (*i.e.* $P(\theta) = \cos(\theta)$), and differentiating Eq. 5.12, one arrives at the following expression for the gain change distribution:

$$P(\Delta Q) = \frac{1}{p_1 p_2 \Delta Q^2} \frac{\sin(\cos^{-1}(\frac{1}{p_1 \Delta Q})/p_2)}{\sin(\cos^{-1}(\frac{1}{p_1 \Delta Q}))} \quad (5.14)$$

To get the neutron peak function in keV, one substitutes ΔQ by $764(1 - \Delta Q)$. Eq. 5.14 is a skewed function that can be used to fit neutron peaks after convolving a Gaussian to account for energy resolution.

The minimum fractional charge loss ΔQ_{min} for the particular set of (unoptimized) parameters used in generating fig. 5.5 is $1/p_1 \sim 3\%$, and occurs at $\theta = 0^\circ$, when the

⁸The angular distribution of events with fully-contained p - t tracks is not strictly isotropic.

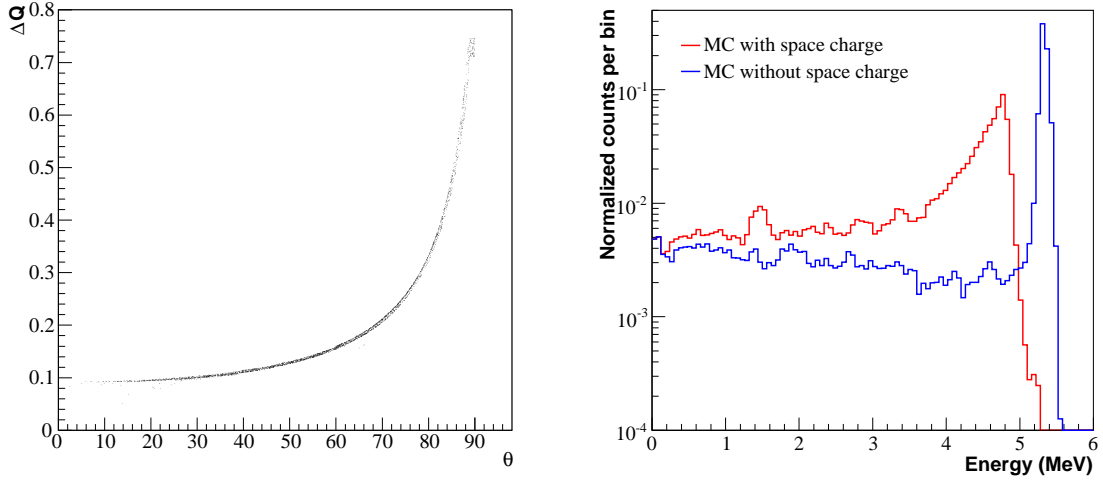


Figure 5.6: Left: the fractional charge loss ΔQ as a function of θ for fully-contained 5.3 MeV alphas, using a Monte Carlo simulation of pulse shapes with the model discussed in §5.2.2. Right: calculated 5.3 MeV alpha spectra with (red), and without the space charge model (blue). The same trial parameters \mathcal{W} and η as in the left figure were used in the model. The leftward shift of the ^{210}Po peak is clearly seen.

track is parallel to the anode. The maximum loss occurs at $(\theta = 90^\circ, \phi \sim 90^\circ)$, and is $\sim 25\%$. This means that one expects to see a threshold in the neutron energy spectra at $(0.97 \times 0.75 \times 764) \sim 560$ keV, below which there should be no fully-contained p - t tracks. This is the origin of the step-like feature mentioned in §5.2.1, and can clearly be seen in fig. 5.5 (right). Also shown for comparison in this figure, is a Monte Carlo generated spectrum without space charge effects (blue). The plateau from ~ 573 keV upwards is caused by ‘wall effect’ tracks with the proton going inwards, and does not explain the feature at 600 keV in the data, as first pointed out in §5.2.1.

Fig. 5.6 (left) is the corresponding plot of ΔQ as a function of θ for fully-contained 5.3 MeV alphas. For the values of \mathcal{W} and η used here, the minimum and maximum fractional charge losses are $\sim 9\%$ and $\sim 75\%$. As seen in fig. 5.6 (right), this results in the ^{210}Po peak to appear at $0.91 \times 5.3 = 4.8$ MeV. One would also expect a threshold at $\sim 0.25 \times 5.3 = 1.3$ MeV, below which there are no fully-contained ^{210}Po tracks. This results in a feature at ~ 1.5 MeV, which is the analogue of the shoulder-like shape at 600 keV in fig. 5.5. In the data, the threshold is observed at 2.3 MeV, while the downward peak shift is around 6.5% (fig. 5.3). The search for a suitable set of values (\mathcal{W}, η) that reproduces these observations was described in the last section.

To summarize, the origins of the spectral features (a)–(c) in §5.2.1 have been explained by the simple space charge model described in §5.2.2.

5.3 Energy resolution

The total energy resolution $\sigma_T(E)$ of NCDs at a given energy E can be expressed as:

$$\sigma_T = \sigma_e + \sigma_p(E) \quad (5.15)$$

where σ_e is the contribution from electronics, which is assumed to be a constant at all energies, and $\sigma_p(E)$ is the energy-dependent component contributed by fluctuations in physics processes in the counters. Values of σ_e were extracted by Prior [88], for each string, from electronic calibration runs.

Following [63], $\sigma_p = C\sqrt{E}$, with the constant C dependent on the statistical details of the ionization and charge multiplication processes, *e.g.* quantities such as the Fano factor⁹. Rather than performing a first-principles calculation of C , it is preferable to determine C empirically. By measuring σ_T and σ_e at the neutron peak, one can infer σ_p , and fix C . The width of the ^{210}Po peak can therefore be predicted. For alpha particles, the resolution is further worsened by passage through nickel, as discussed in the next section. Counter-by-counter gain variations also broaden mono-energetic features considerably in certain strings. These fluctuations have been estimated using neutron sources deployed at different z positions along each string [80], and are included in the simulation.

5.4 Straggling of α particles in nickel

α spectra might be smeared considerably because of energy straggling in the NCD walls. Comfort *et al.* [89] and Sykes *et al.* [90] measured the variance of energy distributions of α particles after passing through thin nickel and copper foils, using 8.78 MeV and 5.486 MeV sources, respectively. In this work, their FWHM values are expressed as a function of the mean fractional energy loss, and fitted to a polynomial curve (fig. 5.7). The resulting RMS energy straggling (in MeV) is:

$$\sigma(E) = \frac{0.001}{2\sqrt{2\ln(2)}}(-27.74 + 28.59E - 3.202E^2 + 0.2064E^3 - 7.561\times 10^{-3}E^4 + 1.642\times 10^{-4}E^5 - 2.082\times 10^{-6}E^6 + 1.417\times 10^{-8}E^7 - 3.985\times 10^{-11}E^8) \quad (5.16)$$

⁹The Fano factor quantifies the deviation of ionization fluctuations from pure Poisson statistics [63].

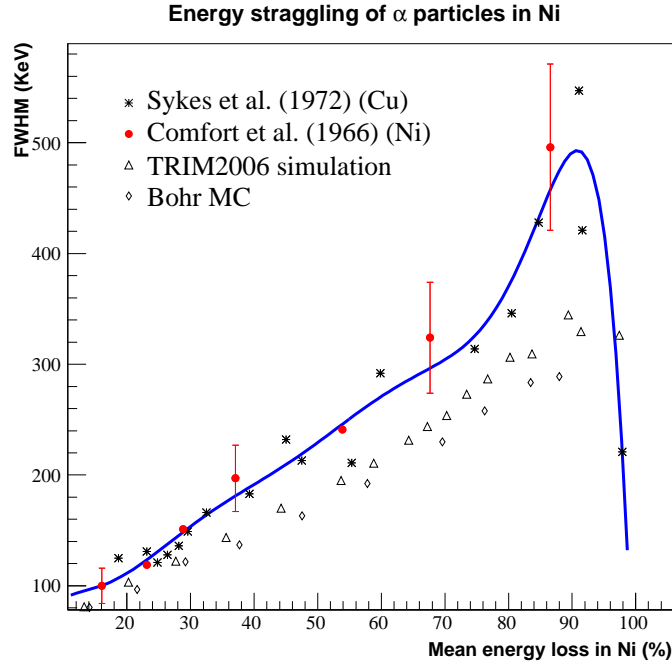


Figure 5.7: Energy straggling of α particles in nickel. The blue line is a polynomial fit to the Comfort and Sykes data, used in pulse calculations.

where E is in MeV. The energy straggling can be as large as 500 keV for a 5 MeV α particle losing 4.5 MeV in the walls. For embedded daughters, the distribution of α particle energies coming out of the nickel is rather flat. Thus, straggling in nickel should not impact on the shape of bulk α energy distributions significantly. On the other hand, sharp spectral features are toned down, *e.g.* if 5.3 MeV ^{210}Po α particles are not exactly on the NCD wall surfaces, but travel through a thin layer of nickel before exiting into the gas.

A robust theory of energy loss fluctuations of light ions in matter at low energies (below 1 MeV) does not yet exist [77]. Fig. 5.7 shows the TRIM 2006 and Bohr straggling [91] predictions for nickel, which both fall below the measured values. The lack of a reliable theoretical prediction justifies the use of the empirical equation, Eq. 5.16, in energy spectrum calculations.

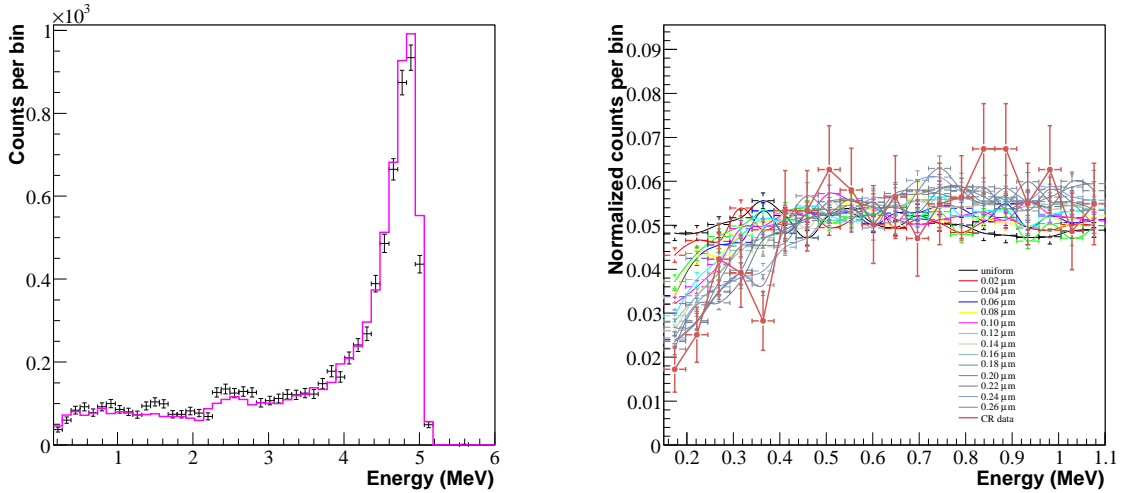


Figure 5.8: Left: alpha spectrum from a high purity ^{210}Po alpha sample (black markers) taken in the SNO control room, compared to the MC ^{210}Po simulation at a mean depth of $0.1\ \mu\text{m}$ (in magenta). Optimized space charge parameters are applied. The plot on the right shows the decrease in counts at low energies (data is in brown markers). This decrease is dependent on the mean depth of ^{210}Po nuclei inside the wall.

5.5 Alpha energy spectra

5.5.1 ^{210}Po spectrum

A high purity ^{210}Po alpha sample is available from test bench data taken in the SNO control room, providing an excellent test of the space charge model in particular. This data¹⁰ comes from a single, undeployed NCD counter. Although the experimental setup involved shorter cables and did not contain any delay line, the charge spectrum itself should closely resemble ^{210}Po spectra from strings in the NCD array.

It was found that calculated ^{210}Po energy pdfs compare better with the data when MC alphas pass through a thin nickel layer. This suggests that ^{210}Pb and ^{210}Po isotopes are not located exactly on inner counter surfaces, but slightly embedded. The mechanism by which this occurred is unclear. Several possibilities, which will not be investigated in this work, have been proposed: diffusion of Rn into NCD surface cracks; side effects of electropolishing; ^{210}Pb or ^{210}Po migration, and nuclear recoil.

An exponential distribution is a convenient and economical one-parameter function to describe embedded ^{210}Po . The parameter in question is, of course, the mean impurity

¹⁰Data taken by McGee.

depth \bar{d} . In the limits $\bar{d} \rightarrow 10 \mu\text{m}$ ¹¹ and $\bar{d} \rightarrow 0$, the uniform and pure surface cases are recovered, respectively. Fig. 5.8 (left) shows the ²¹⁰Po sample compared with a spectrum generated for ²¹⁰Po nuclei whose spatial profile in the wall is exponential, $\frac{1}{\bar{d}}e^{-(x-b)/\bar{d}}$, with a mean depth $\bar{d} = 0.1 \mu\text{m}$. The optimized values of η and \mathcal{W} (§5.2.3) are used. The number of counts decreases at low energies, the more so with increasing \bar{d} (right), because fewer alphas come out at large azimuthal angles. This means that they are less likely to hit the wall as soon as they emerge. The surface case ($\bar{d} = 0$) produces a spectrum (shown in black) that does not display a decline in counts at low energies, to the same extent as the data. Moreover, the 4.8 MeV peak for $\bar{d} = 0$ was observed to be too narrow. If impurities are embedded, the 5.3 MeV alphas straggle in nickel before emerging in the gas. This worsens the energy resolution, as mentioned previously in §5.4.

The best value of \bar{d} for the NCD array cannot be extracted from the test bench ²¹⁰Po alpha sample alone. One can optimize \bar{d} if a pure ²¹⁰Po sample from the NCD array were available, which is unfortunately not the case. For simplicity, a value of $\bar{d} = 0.1 \mu\text{m}$ will be hereafter assumed in all strings.

5.5.2 Bulk spectra

Comparisons of MC generated neutron and ²¹⁰Po spectra with data give confidence that mono-energetic lines are being adequately computed at 0.764 and 5.3 MeV. If the extrapolation in fig. 5.4 holds, energy spectra should be correctly predicted at all other energies. This is a fundamental assumption in the calculation of bulk alpha spectra, where a continuous distribution of initial alpha energies in the gas has to be dealt with. To calculate this initial energy distribution, one has to find:

- (1) The starting alpha energies in nickel (see appendix B).
- (2) The energy loss in the walls.

The second problem is more difficult to address. The energy deposited in the walls depends not only on the stopping power, straggling, directions and paths of alphas, but also on the spatial distribution of impurities.

It is now argued that ²³⁸U and ²³²Th chain isotopes are not uniformly distributed in NCD walls. The following observations were made:

¹¹The range of ²¹⁰Po alphas in nickel is $\sim 10 \mu\text{m}$.

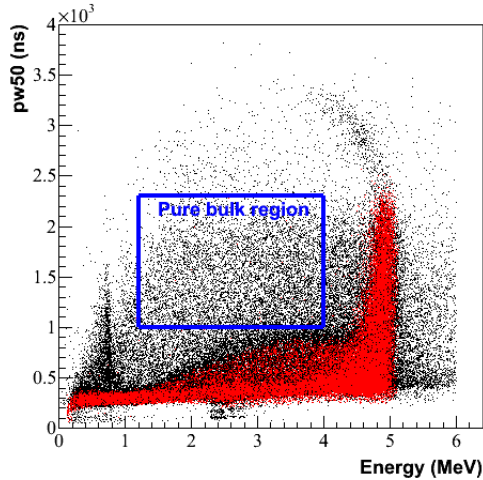


Figure 5.9: Selection of bulk α events (blue box) in $pw50$ vs Energy space. Red: MC ^{210}Po alphas; black: data.

- (a) Drift times of electrons in NCD tubes are stable, as demonstrated by pulse width distributions in neutron calibration data. A $1000 \text{ ns} < pw50 < 2300 \text{ ns}$ cut on alpha pulses eliminates the majority of wall and large-width wire ^{210}Po events in the energy range $E < 4 \text{ MeV}$ (see fig. 5.9); neutrons are removed by imposing $E > 1.2 \text{ MeV}$. By applying these cuts and looking at the projection onto the horizontal axis, it is possible to make string-by-string comparisons of high purity bulk α energy pdfs. It is observed that the peaks of these distributions are not consistent across the array (see the top four figures in fig. 5.10 for strings 10, 12, 30 and 37). These discrepancies could not be explained by combining MC generated ^{238}U and ^{232}Th pdfs, computed using the method discussed in previous sections, and assuming (a) *radioactive equilibrium*, (b) a *uniform spatial distribution* in the nickel.
- (b) String-by-string energy fits, without any FWHM cuts, show that the best-fit bulk energy pdfs calculated using a flat spatial distribution in the walls do not compare well to the data. The bottom left of fig. 5.10 shows the sum of all the string fits compared to the array spectrum. It is seen that the MC overestimates the number of alpha events in the neutron energy region. Clearly, if bulk spectra in NCD strings were, on average, peaked at higher energy than in the MC, better agreement would be obtained.
- (c) ^{220}Rn and ^{216}Po events in the ^{232}Th chain can be identified owing to the short time

delay between them (fig. B.2). The extracted energy pdfs of 6.8 MeV ^{216}Po and 6.3 MeV ^{220}Rn alpha candidate events from NCD walls are not consistent with simulation, if a uniform spatial distribution is assumed for these isotopes. The selection of ^{220}Rn and ^{216}Po coincidence events is described in appendix G. Fig. 5.10 (bottom right) shows the MC ^{216}Po spectrum (red) compared with the extracted ^{216}Po spectrum (black). The candidate ^{220}Rn spectrum is also shown in blue, and peaks at lower energy, as one would expect. The peaks in the data on the right edge of the spectra suggest that ^{220}Rn and ^{216}Po nuclei might be more concentrated towards the inner surface of NCD walls.

Therefore, bulk spectra vary from string to string, in a way that is not accountable by ^{232}Th and ^{238}U pdfs calculated assuming spatial uniformity. Indeed, the peaks of bulk distributions appear to be shifted to higher energies relative to the MC. The possibility of radioactive equilibrium causing (a)–(c) was briefly examined, using the scenario described in [87]: Ra isotopes are preferentially removed by the CVD process during NCD manufacture, breaking the chains in two components. The lower parts¹² of both ^{238}U and ^{232}Th chains peak at higher energies than the upper parts, and it is speculated that combinations of four pdfs ($^{232}\text{Th}_{low}$, $^{232}\text{Th}_{up}$, $^{238}\text{U}_{low}$, $^{238}\text{U}_{up}$) might explain the varying shifts in bulk spectra. Yet, it was found that differences between the full chain pdfs and the lower parts for both ^{232}Th and ^{238}U are marginal. Chain disequilibrium does not perturb the bulk pdfs sufficiently to explain the variations described in (a). This, however, does not exclude the possibility of the chains being in disequilibrium indeed.

A natural explanation for observations (a)–(c) is that ^{238}U and ^{232}Th impurities are not uniformly distributed in the nickel walls, but instead, more concentrated towards the inner surface¹³. If this is the case, on average, alphas pass through less nickel, resulting in more energy deposited in the gas. The spatial profile could differ from string to string, causing the observed differences in the shapes of bulk pdfs.

The actual impurity distribution is unknown. It was suggested to decouple ^{238}U and ^{232}Th α backgrounds into surface, and uniformly distributed bulk components [92]. The surface components would then be described by exponential distributions, as in the

¹²The isotopes in each chain are listed in table 6.1 of [87].

¹³For instance, a thin layer of Al_2O_3 , from the aluminium mandrel used in the nickel CVD process, could be present.

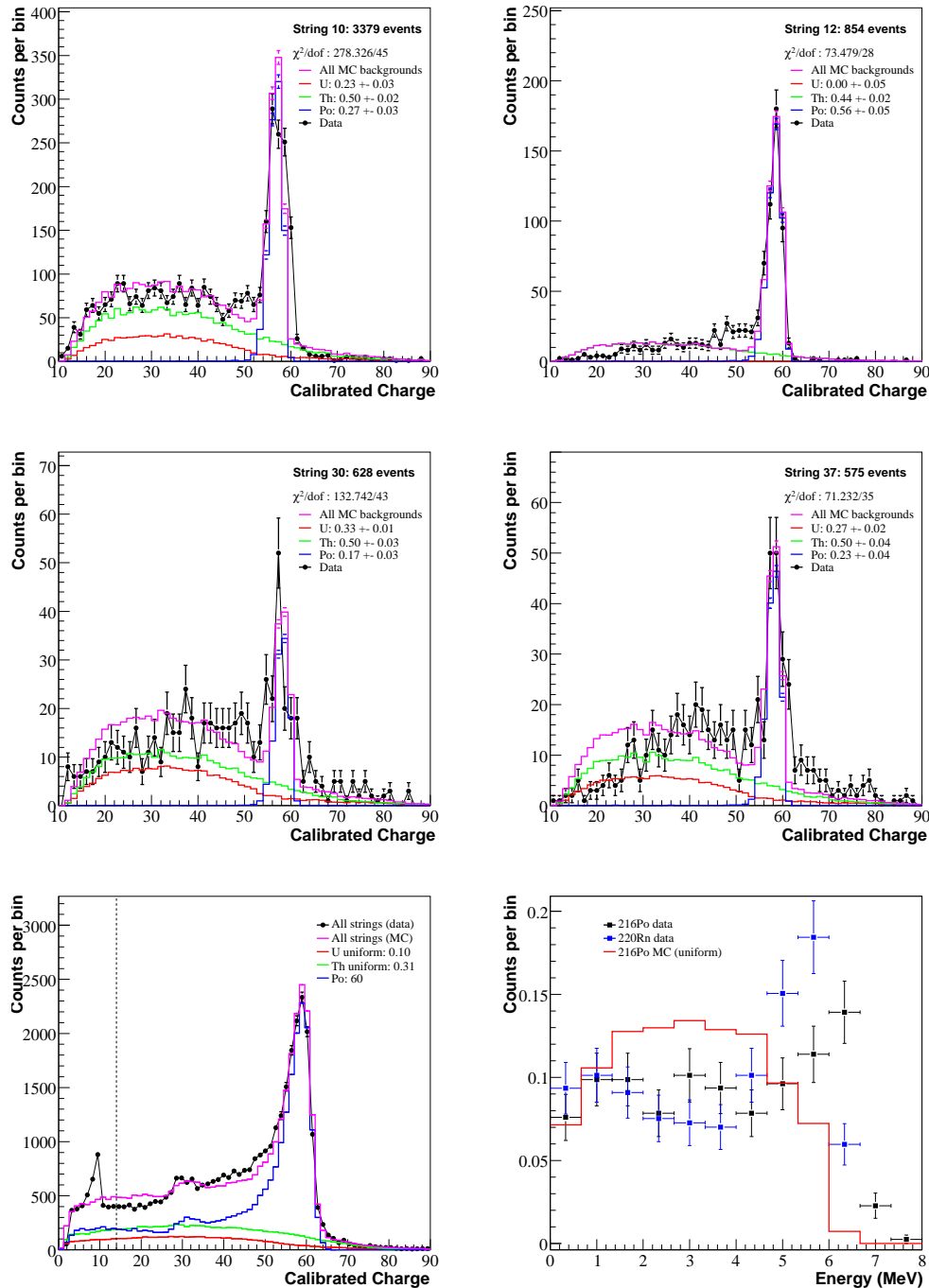


Figure 5.10: Evidence for non-uniformity of bulk impurities. Top four figures: Energy spectra of four NCD strings with a cut $1000 \text{ ns} < \text{FWHM} < 2300 \text{ ns}$. The region with calibrated charge < 50 should be free of ^{210}Po events, and is a good indication of the shape of bulk spectra. Also shown are the MC best-fit predictions (blue: Po, red: U, green: Th, magenta: total), assuming impurities are uniformly distributed in the walls. It is clear that the peaks of bulk distributions shift from string to string. Bottom left: Sum of energy fits to NCD strings, assuming uniformly distributed impurities. Bottom right: ^{232}Th double coincidence spectra (black: ^{216}Po , blue: ^{220}Rn), compared with the MC generated ^{216}Po spectrum in red.

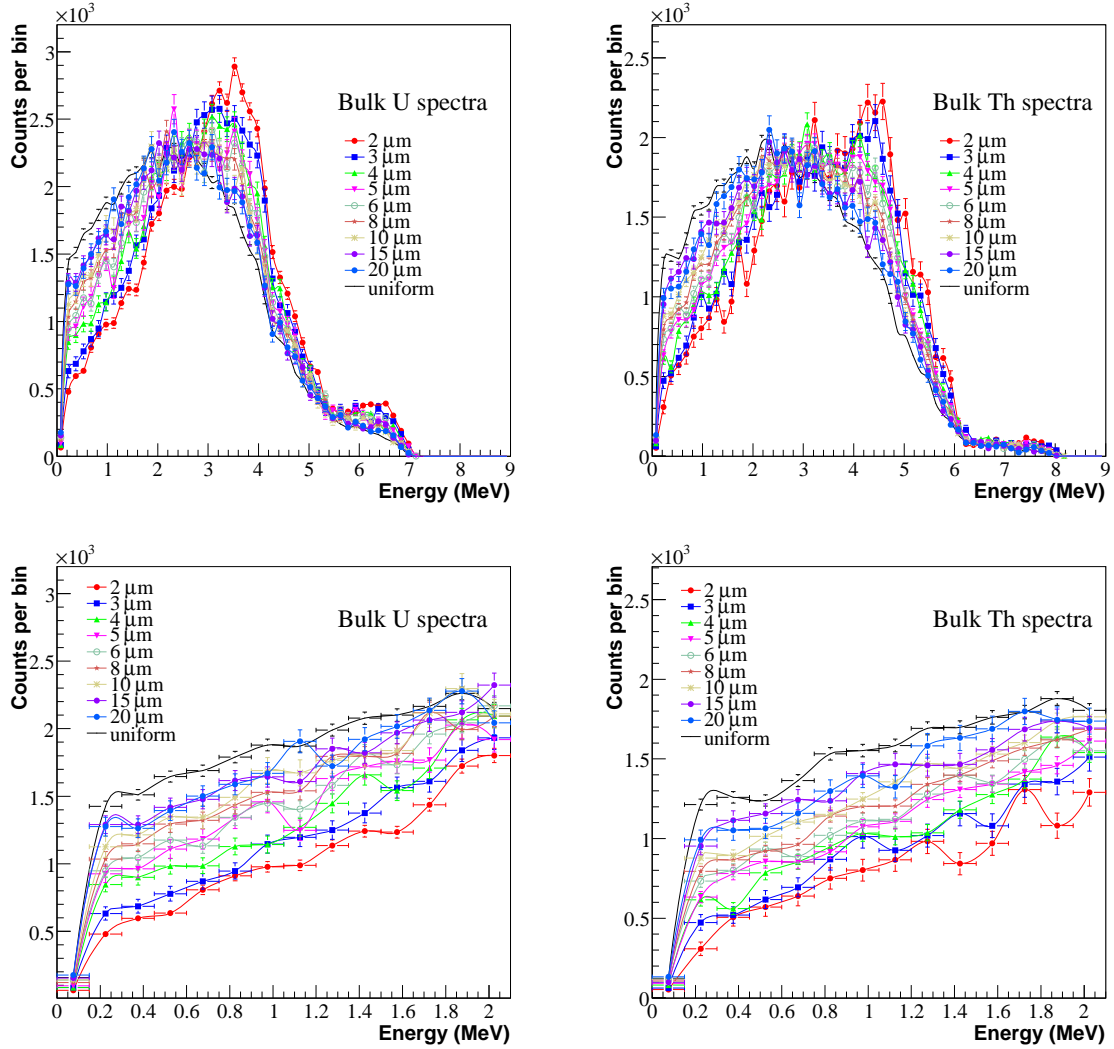


Figure 5.11: Dependence of the ^{238}U (top left) and ^{232}Th (top right) spectral shapes on mean impurity depths, assuming exponential distributions for the spatial profiles. The expected number of events in the neutron region decreases, and the peak of bulk distributions shift towards higher energies as impurities become more concentrated towards the inner wall. Bottom left: shapes of low energy ^{238}U spectra at various values of \bar{d} . Bottom right: low energy ^{232}Th spectra at various values of \bar{d} .

^{210}Po case. However, this means that at least two more variables need to be introduced to describe NCD alpha spectra. For simplicity, in this work, a single exponential depth distribution is assumed for each decay chain. Fig. 5.11 shows how ^{238}U (left) and ^{232}Th (right) pdfs change as a function of the mean depth \bar{d} . As expected, these become more peaked towards higher energies with decreasing \bar{d} .

Predicted shapes of ^{238}U and ^{232}Th spectra as a function of \bar{d} , below 2 MeV, are shown in the bottom panels of fig. 5.11. The full energy curves are normalized to the total number of events under the black line (uniform case) from 0 to 9 MeV. The expected rate in the neutron region goes down with decreasing \bar{d} , because alphas exit the nickel at higher energies on average.

5.6 Background content of NCD strings

In this section, MC generated energy α spectra are used to determine the fractional ^{210}Po , ^{238}U and ^{232}Th contents of each string. The mean U and Th impurity concentrations of NCD nickel are then derived.

Binned maximum likelihood fits to string energy distributions were performed. A calibrated charge interval of 14–80 was used, corresponding to an energy range of 1.2–6.5 MeV. Calibrated charge was preferentially chosen as the fit variable, because of some problems with the energy scale on some strings after a hardware upgrade in February 2006. The MC charge scaling [65] and energy resolution are not perfect, and thus, corrections were first applied to align simulated and observed ^{210}Po α peaks on each string.

The fit statistic is defined as [93]:

$$\begin{aligned}\chi_{\bar{d}}^2 &= 2 \sum_{i=0}^N D_i \ln \left(\frac{D_i}{M_{i,\bar{d}}} \right) + M_{i,\bar{d}} - D_i \\ M_{i,\bar{d}} &= n_u U_{i,\bar{d}} + n_{po} P_i + (1 - n_u - n_{po}) T_{i,\bar{d}}\end{aligned}\quad (5.17)$$

where N is the number of bins (60), D_i is the data, and $M_{i,\bar{d}}$ is the MC prediction at a mean U/Th depth \bar{d} . $M_{i,\bar{d}}$ consists of ^{210}Po ($P_{i,\bar{d}}$), ^{238}U ($U_{i,\bar{d}}$), and ^{232}Th ($T_{i,\bar{d}}$) pdfs, which are similar in shape to those found in figs. 5.8, 5.11 (top left) and 5.11 (top right). A mean ^{210}Po depth of $0.1 \mu\text{m}$ is assumed in all strings. There are only two fit parameters: the ^{238}U and ^{210}Po fractions, n_u and n_{po} . To find the optimum U and Th impurity depth in a given string, the fit is repeated at 9 discrete intervals of \bar{d} : 2, 3, 4, 5, 6, 8, 10, 15, 20 μm .

The mean depths of U and Th chain impurities are assumed to be equal in all strings. A depth of 20 μm is almost identical to the uniform case, because all ^{238}U and ^{232}Th alphas beyond 22 μm either range out in the nickel, or exit in the heavy water. A cubic curve is fitted to the χ_d^2 vs \bar{d} space, and the value minimizing the curve is picked. Uncertainties on the estimated depth are found by searching for values of \bar{d} increasing χ_d^2 by one unit. Results are shown in the 6th column of table 5.2. The mean ^{238}U and ^{232}Th depth across the whole array was found to be $\sim 7 \mu\text{m}$.

Columns 3, 4 and 5 of table 5.2 give the derived fractional ^{238}U , ^{232}Th and ^{210}Po contents in each string. The fitted proportions of ^{238}U and ^{232}Th alphas are highly correlated, and roughly equal. Bulk and surface fractions in some strings can be mis-estimated in the presence of counter gain mismatches. Such cases result in rather bad χ^2 , *e.g.* strings 35 and 10. Given a total NCD length of 396 m, and 60,519 alphas observed in 385 live days [37] above calibrated charge 14¹⁴, the ^{238}U and ^{232}Th fractions translate to concentrations of 6.6×10^{-12} gTh/gNi and 2.1×10^{-12} gU/gNi in the 22 μm nickel layer adjacent to the live NCD region. This is comparable to results from *in-situ* radio-assay techniques: 3.4×10^{-12} gTh/gNi and 1.8×10^{-12} gU/gNi [36]. The inferred flux of ^{210}Po and bulk alphas from the strings included in this analysis are, roughly, $1.5 \text{ m}^{-2}\text{day}^{-1}$ and $1 \text{ m}^{-2}\text{day}^{-1}$, respectively. The number of β events from bulk impurities is estimated in the next section.

Column 7 shows wire alpha fractions, obtained by counting the number of events with a FWHM of more than 2300 ns on each string. In each case, the percentage is expressed relative to the number of alpha events observed above calibrated charge 14. According to the MC, assuming surface wire activity only, 49.6 % of wire events are wider than 2300 ns. All other alpha types have a narrower FWHM. The strings with the dirtiest anodes were identified to be 1, 4 and 35. It is estimated that, of all alphas observed in the array, about 2 % are wire alphas, amounting to an average flux of about 50 surface ^{210}Po alphas per m^2 of Cu per day. This is significantly higher than the estimated flux of ^{210}Po alphas from inner NCD surfaces, which were electropolished and chemically treated.

The sum of fitted spectra from each string can be seen in fig. 5.12 (magenta curve), with data shown in black. The constituent ^{238}U , ^{232}Th and ^{210}Po spectra are shown in red, green and blue, respectively. Fig. 5.12 can be compared with the uniform impurity

¹⁴Excluding strings 18, and the ^4He strings.

string	χ^2/dof	^{238}U	^{232}Th	^{210}Po	d (μm)	Wire %	Note
0	69.82/57	0.18±0.04	0.08±0.04	0.74±0.01	9±5	1.3	¶
1	49.03/57	0.00±0.07	0.64±0.08	0.36±0.03	5±2	5.4	¶
2	76.23/57	0.11±0.04	0.12±0.05	0.77±0.02	8±5	1.1	
3	72.88/57	0.29±0.03	0.23±0.03	0.48±0.01	2±1	2.1	◇
4	46.25/57	0.20±0.05	0.31±0.06	0.48±0.02	8±3	10.0	
5	60.31/57	0.29±0.08	0.27±0.09	0.43±0.04	2±1	1.9	
6	48.31/57	0.27±0.01	0.10±0.05	0.63±0.05	2±12	2.9	
7	68.94/57	0.14±0.09	0.25±0.10	0.61±0.03	2±2	1.7	
8	61.25/57	0.34±0.04	0.00±0.06	0.66±0.07	2±1	1.7	¶
9	78.93/57	0.15±0.02	0.00±0.03	0.85±0.04	12±5	0.5	
10	287.18/57	0.49±0.01	0.01±0.01	0.50±0.01	10±3	2.1	‡,◇
11	64.66/57	0.37±0.09	0.08±0.10	0.55±0.04	2±4	3.0	
12	102.82/57	0.25±0.01	0.03±0.02	0.72±0.01	9±2	1.6	
13	37.32/57	0.30±0.03	0.00±0.02	0.70±0.04	10±4	1.6	
14	49.59/57	0.22±0.10	0.21±0.10	0.57±0.02	5±4	0.9	
15	62.35/57	0.15±0.11	0.21±0.12	0.64±0.04	8±5	0.3	
16	57.03/57	0.24±0.05	0.12±0.06	0.64±0.03	9±3	2.6	
17	78.08/57	0.38±0.02	0.00±0.02	0.62±0.03	6±4	0.1	
18	N/A	N/A	N/A	N/A	N/A	2.7	§,¶
19	72.82/57	0.19±0.03	0.00±0.02	0.81±0.04	20±7	2.0	
20	N/A	N/A	N/A	N/A	N/A	2.5	§,◇
21	92.74/57	0.00±0.58	0.35±0.58	0.65±0.03	9±4	1.1	
22	89.51/57	0.32±0.03	0.13±0.04	0.54±0.02	6±4	1.4	
23	133.63/57	0.25±0.03	0.00±0.02	0.75±0.02	5±3	2.0	
24	68.34/57	0.45±0.05	0.01±0.06	0.54±0.03	8±2	2.1	
25	109.97/57	0.39±0.03	0.00±0.02	0.61±0.04	10±2	0.4	
26	53.22/57	0.03±0.08	0.42±0.08	0.55±0.02	20±10	1.8	¶
27	52.01/57	0.11±0.12	0.27±0.12	0.62±0.04	10±6	2.6	
28	72.43/57	0.25±0.14	0.53±0.16	0.22±0.08	3±3	3.6	
29	56.15/57	0.33±0.02	0.00±0.02	0.67±0.03	10±4	4.0	
30	82.44/57	0.08±0.07	0.76±0.07	0.16±0.02	3±2	2.8	◇
31	115.48/57	0.17±0.02	0.05±0.02	0.78±0.02	8±2	3.9	¶
32	100.77/57	0.26±0.05	0.03±0.05	0.71±0.02	6±3	2.0	
33	53.88/57	0.12±0.03	0.33±0.02	0.55±0.04	2±4	4.0	
34	68.31/57	0.27±0.06	0.03±0.06	0.70±0.03	10±3	3.1	
35	215.61/57	0.00±0.03	0.66±0.01	0.34±0.02	20±5	5.0	‡
36	56.23/57	0.32±0.04	0.00±0.05	0.68±0.06	10±3	1.6	
37	68.69/57	0.00±0.61	0.67±0.61	0.34±0.01	5±2	4.5	
38	83.28/57	0.31±0.03	0.02±0.03	0.67±0.01	20±1	2.2	
39	70.91/57	0.14±0.06	0.4±0.06	0.48±0.01	7±3	2.6	
All	-	0.21±0.03	0.18±0.03	0.61±0.01	6.6	1.8	*

Table 5.2: Estimated string fractions and depths from maximum likelihood fits to the energy spectra of each string, using data taken from the start of the NCD phase to February 2006. The wire alpha fractions come from inspecting pulse width distributions. ‡: string resolution worsened significantly by counter gain differences. §: Multiple ^{210}Po peaks. ¶: String excluded from analysis. *: Excluding ^4He strings and string 18. ◇: ^4He string.

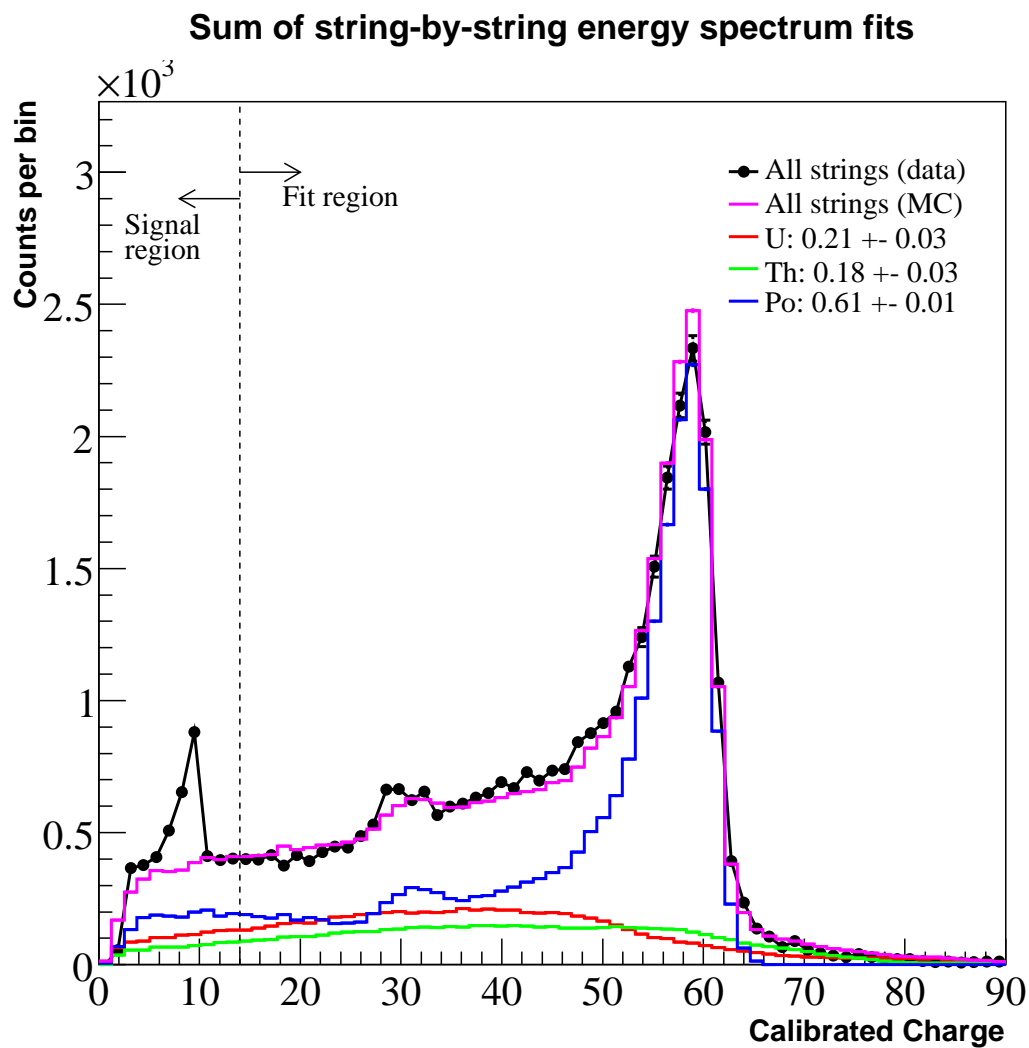


Figure 5.12: Sum of individual string energy fits, using data taken from the start of the NCD phase to February 2006. The neutron peak can be seen at calibrated charge ~ 9 .

case at the bottom left of fig. 5.10: there is a clear improvement in the fit quality. Varying the bulk impurity depths barely changes the extracted ^{210}Po and bulk fractions. However, there are significant differences in the predicted alpha rates in the neutron energy region. Accurate values of \bar{d} are therefore necessary to predict the low-energy α background shape, and to derive the number of background α events in the neutron energy window with confidence.

The neutron peak is clearly seen at calibrated charge ~ 9 . With a robust α background model in hand, neutrons can be statistically separated from alphas by fitting the NCD array spectrum in the neutron energy window. To perform such a fit, the shaper energy distribution expected of NC neutrons can be accurately obtained from ^{24}Na source calibrations, while the net alpha background pdf can be calculated using the present simulation. Further details of such energy fits can be found in [32, 103, 104].

5.7 β energy spectrum

5.7.1 Estimation of the β event rate

Fig. 5.13 shows the calculated probability of observing a ‘clean’ correlated scope-shaper β -decay event pair in the neutron region, as a function of the kinetic energy of electrons (between 0.2 and 3 MeV) coming out of the walls. There is a minimum at around ~ 1 MeV corresponding to the location of the minimum in the $\frac{dE}{dx}$ curve (fig. 4.3). The yield increases below and above 1 MeV because more energy is deposited in the gas. The MC indicates that, for most purposes¹⁵, a probability of 1×10^{-4} can be conservatively assumed. If impurities are uniformly distributed, the fractions of all ^{238}U and ^{232}Th decay β s penetrating the gas with over 200 keV K.E. are calculated by EGS4 to be 0.058 and 0.067. Assuming secular equilibrium, half lives of 1.4×10^{10} (^{232}Th) and 4.47×10^9 (^{238}U) years, concentrations of 3.4×10^{-12} gTh/gNi and 1.8×10^{-12} gU/gNi [36], and a total mass of $\sim 2 \times 10^5$ g of nickel in the array, the number of β events that would be observed in the 385 live days of the NCD phase are, approximately:

$$1.05 \cdot \frac{3.4 \times 10^{-12} \cdot 6.02 \times 10^{23} \cdot 2 \times 10^5 \cdot \ln 2}{232 \cdot 1.4 \times 10^{10}} \cdot 0.067 \cdot 1 \times 10^{-4} = 0.5 \quad (5.18)$$

for the ^{232}Th chain, and 0.8 for the ^{238}U chain.

¹⁵The probability of ^{238}U and ^{232}Th decay chain β s having more than 3 MeV K.E. is negligible (fig. 5.15).

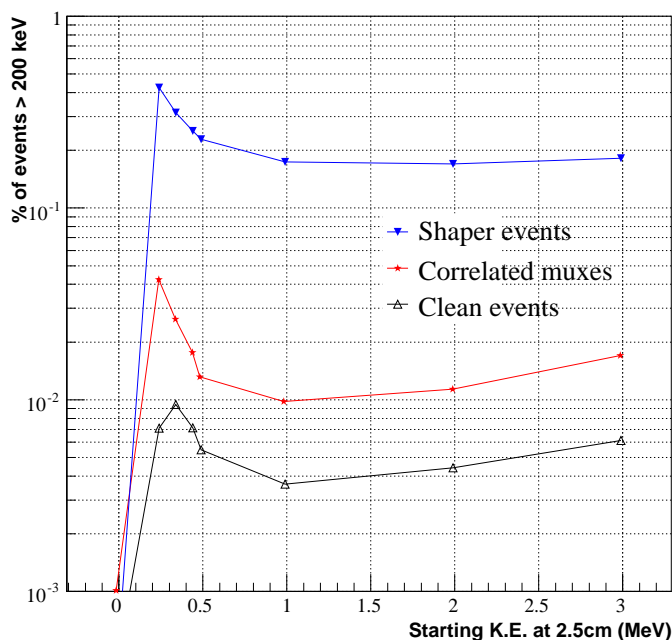


Figure 5.13: Calculated percentage yield of β events in the neutron energy region, as a function of kinetic energy. All particles start isotropically from a radius of 2.5 cm.

It therefore appears that β events constitute a negligible background. However, it is still useful to be able to calculate β energy spectra, in the event that a number of strong, localized sources of β particles are present on the inner surfaces of NCDs.

5.7.2 Simulation method

A semi-analytic method, based on the parameterization of MC results, was developed to calculate β spectra efficiently. It can be assumed that most electrons with more than 0.2 MeV of kinetic energy come from outside the gas, and leave the nickel isotropically. The strategy is to first find an analytic form for the measured shaper energy distributions of mono-energetic electrons leaving the nickel¹⁶ with an isotropic angular distribution. Given this parameterization, and the energy distribution of β s exiting the walls, the approximate spectral shape under a wide range of scenarios can then be computed at little computational expense, because all pulse shape calculations are by-passed.

¹⁶EGS4 was used for propagating electrons before computing their pulse shapes. The simulation parameter ECUT [74] inputted to EGS4 has to be lowered from its default value to below 0.2 MeV for all materials the NCDs are made up of.

In the kinetic energy range $0.7 < E_s < 3$ MeV, the spectrum, after data reduction, was found to be well described (see fig. 5.14, right) by a lognormal function (Eq. 5.19). The spectral shape is rather stable for E_s between 0.7 and 3 MeV. The weak dependence of the mean μ_l and standard deviation σ_l of the lognormal distribution on E_s is shown in table 5.3. When $E_s < 0.7$ MeV, the spectrum contains a cut-off and a peak at $\sim E_s$, since the particle cannot deposit more energy than what it started off with. In this case the spectrum can be described by the sum of a lognormal distribution truncated at $E = E_s$, and a Gaussian distribution centered at E_s . A skewed function such as Eq. 5.14, which takes into account space charge effects, is perhaps more appropriate, but is not adopted here, for simplicity. The width of the Gaussian is the counter resolution described in §5.3, while the relative normalizations of the lognormal and Gaussian functions are found by counting the number of events where E_s is fully deposited in the gas (table 5.3).

To summarize, the following parameterization for the NCD spectrum of mono-energetic and isotropic β particles of kinetic energy E_s can be adopted:

$$\begin{aligned}
 f_\beta(E) &= \frac{C}{E\sigma_l\sqrt{2\pi}} e^{-\frac{(\ln(E)-\mu_l)^2}{2\sigma_l^2}} & 0.7 < E_s < 3\text{MeV} \\
 f_\beta(E) &= \frac{A}{E\sigma_l\sqrt{2\pi}} e^{-\frac{(\ln(E)-\mu_l)^2}{2\sigma_l^2}} + \frac{B}{\sigma\sqrt{2\pi}} e^{-\frac{(E-E_s)^2}{2\sigma^2}}, & E < E_s \cap E_s < 0.7\text{MeV} \quad (5.19) \\
 f_\beta(E) &= \frac{B}{\sigma\sqrt{2\pi}} e^{-\frac{(E-E_s)^2}{2\sigma^2}} & E > E_s \cap E_s < 0.7\text{MeV}
 \end{aligned}$$

A , B and C are normalization constants. The ratios B/A at different values of E_s , are given in table 5.3¹⁷.

$E_s(\text{MeV})$	0.25	0.35	0.4	0.45	0.5	1	1.5	2	2.5
B/A	8.99	2.06	1.07	0.75	0.32	0	0	0	0
μ_l	-1.045	-1.045	-1.041	-1.04	-1.035	-1.023	-1.016	-0.996	-0.985
σ_l	0.249	0.247	0.246	0.246	0.245	0.238	0.231	0.224	0.219

Table 5.3: B/A , μ_l and σ_l as a function of electron kinetic energy E_s , evaluated using the electron pulse shape simulation, for β spectrum parametrization. Values of μ_l and σ_l below 1 MeV have been extrapolated from above.

As an example, suppose one wants to calculate the NCD spectra of ^{238}U and ^{232}Th

¹⁷These values are valid for spectra generated with SNOMAN v5.03.

decay electrons, under the assumption that all impurities are uniformly distributed within the nickel. Fig. 5.15 (left) shows the K.E. distributions of ^{238}U and ^{232}Th electrons (appendix B, table 5.4) leaving the walls, as predicted by EGS4. Folding in Eqs. 5.19 yields the energy spectra on the right. In analogy to α backgrounds, differences between ^{238}U and ^{232}Th shapes are very small. An interesting feature of bulk β spectra is the peak at ~ 0.35 MeV, which is a consequence of applying data cleaning cuts.

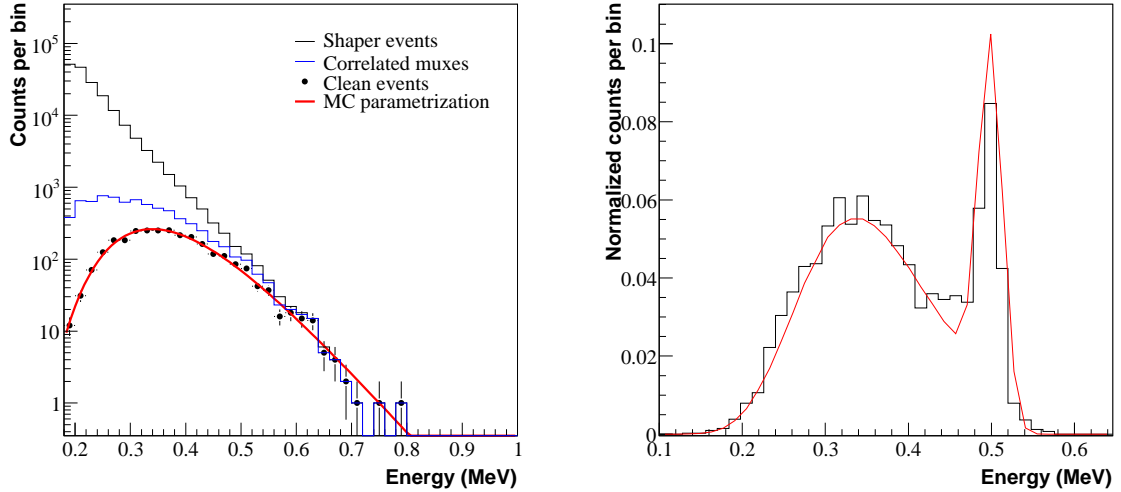


Figure 5.14: Parameterization of the Monte Carlo generated NCD spectrum of 1 MeV (left) and 0.5 MeV (right) K.E. electrons with Eqs. 5.19. Particles with less than ~ 0.8 MeV K.E. can deposit all their energy in the gas, producing a cut-off in the spectrum. After data reduction, this cut-off appears as a peak.

chain	^{232}Th				^{238}U				
isotope	^{208}Tl	^{211}Bi	^{212}Pb	^{228}Ac	^{210}Tl	^{214}Pb	^{210}Bi	^{214}Bi	^{234m}Pa
%	12.3	16.3	0.3	8.6	1.8	3.5	5.1	6.6	17.7
fraction	0.36	1	1	1	0.00021	0.9998	1	1	1

Table 5.4: Percentages of decays from β -emitting ^{238}U and ^{232}Th daughters, that result in an electron penetrating NCD gas with more than 200 keV K.E. Assuming equilibrium, the bottom row is the fraction of all ^{232}Th and ^{238}U decays containing a β from the daughter. Q-values and rough decay schemes can be found in appendix B. A uniform impurity distribution in the walls is assumed.

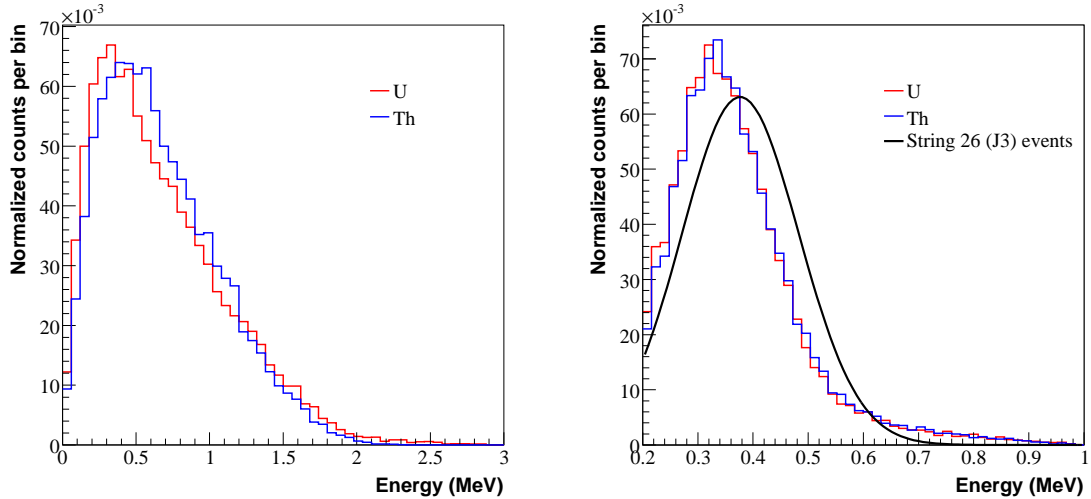


Figure 5.15: Left: Kinetic energies of NCD wall ^{238}U and ^{232}Th decay chain electrons penetrating the gas, assuming the impurities to be uniformly distributed. Right: the resulting shaper spectrum, with data cleaning cuts applied. The black curve is an analytic form for the spectrum of non-neutron-non-alpha events from string 26 (J3) [94]. The calculation used Eqs. 5.19.

5.8 Summary

This chapter focussed on the simulation of the energy spectra of ionization events, as measured by the shaper-ADCs. An accurate knowledge of alpha backgrounds is an essential component of the NC flux extraction.

Mono-energetic spectral peaks suggest the presence of at least one gain loss mechanism. A two-parameter space charge model that explains the shape of mono-energetic peaks (skewness, ledge-shaped features and non-linearities) was described. The model parameters were optimized by studying neutron calibration and ^{210}Po alpha data.

The simulation of wall backgrounds requires careful consideration of energy losses in the nickel. It was demonstrated that observed ^{210}Po alpha spectra are consistent with the ^{210}Po being slightly embedded inside the nickel. It was also shown that ^{238}U and ^{232}Th daughters are not uniformly distributed inside NCD walls. Exponential depth profiles were proposed for ^{210}Po and U/Th chain nuclei.

Using the background model, ^{238}U , ^{232}Th and ^{210}Po α fractions in each string were estimated by performing energy fits. Impurity depths in each string were obtained in the process. Wire alpha fractions were also estimated by means of a pulse width cut.

A fast method for calculating the spectrum of β particle events was introduced. The expected number of β events in the NCD phase was estimated and found to be negligible.

Chapter 6

Separation of Neutrons and Alphas

A central problem in extracting the NC flux in the NCD phase is the determination of the number of neutron events, *i.e.* discriminating neutrons from the dominant background, alphas. This chapter describes a separation technique that uses, almost exclusively, MUX-scope traces. The main difficulties that need to be overcome are:

- (1) A pure background sample does not exist, because the NC neutron signal could not be ‘switched off’. ^4He string α data are statistically limited, and not representative of the rest of the array. External sources could not be used to replicate the NCD array background.
- (2) The MC is biased, as described in §4.6.1. Furthermore, the reliability of MC-generated α samples depends heavily on estimated impurity depth values (§4.6.2).
- (3) A fraction of alpha events are indistinguishable from neutrons. Some of these pulses are not well-understood.

To tackle (1), the NCD simulation is applied to generate α pulse shape parameter distributions for use in a statistical separation of neutrons and alphas. The selected pulse parameter is $R_{10,40} = \frac{pw_{10}}{pw_{40}}$, which is the ratio of pulse widths at 10 % and 40 % of the amplitude. It is essentially a measure of how tapered a pulse can be. Discrimination results from the sizeable fraction of neutrons that are wide and less tapered than alphas. Besides its simplicity and good separation power, the choice of $R_{10,40}$ in this analysis is strongly motivated by the following reasons, which address issue (2) above:

- (a) In the appropriate basis, there are no model uncertainties on $R_{10,40}$ pdfs due to bulk impurity depths errors. This is demonstrated in the next section.

- (b) Corrections due to instrumental systematics can be evaluated and relatively straightforward to apply.

These corrections are described in §6.2. Issue (3) is discussed further in §6.2.3. The corrected $R_{10,40}$ pdfs are vetted against available α data in §6.2.4, and then used to extract the number of neutron events in the NCD phase (§6.3). This allows the NC flux to be deduced in §6.4.

6.1 Representation of alphas below 1 MeV

The most natural way to account for an observed alpha pulse shape parameter distribution is to simulate its ^{210}Po , ^{238}U and ^{232}Th components before mixing them in the right proportions. However, as first pointed out in §4.6.2 (see also fig. 4.18), the shapes of distributions change so rapidly with the impurity depth \bar{d} (which is not known accurately) that a satisfactory description of α data is difficult to achieve. In this section, an alternative representation of alpha pdfs is proposed to mitigate the effects of \bar{d} uncertainties. Instead of representing alpha data as a combination of three main impurity classes, which share similar waveforms, one might use a number of α groups with different generic shapes, to create a more ‘orthogonal’ basis. In the neutron energy region, at least two such groups can be identified:

- I** Sharp, narrow, and high amplitude pulses. These are high energy alphas that need to hit the wall shortly after they come out, in order to deposit less than 1 MeV in the gas.
- II** Broader, low amplitude, triangular-shaped pulses. These alphas exit the nickel with less than 1 MeV K.E. and stop in the gas.

These two groups are illustrated in fig. 6.1. The fractions of each type, x_{I} and x_{II} , are strongly dependent on how impurities are distributed. If isotopes are clustered close to the wall, there is a high concentration of surface-type pulses I and $x_{\text{II}} \sim 0$. If \bar{d} is large, bulk α pulses are mostly of type II. In the {I, II} alpha basis, pulse shape pdfs from embedded ^{210}Po , ^{238}U and ^{232}Th chain nuclei can be thought of as a mixture of type I and II alphas. In each case, x_{I} and x_{II} are determined by \bar{d} . Therefore, the value of \bar{d} is ‘converted’ into the ratio $x_{\text{I}}:x_{\text{II}}$ in the {I, II} basis.

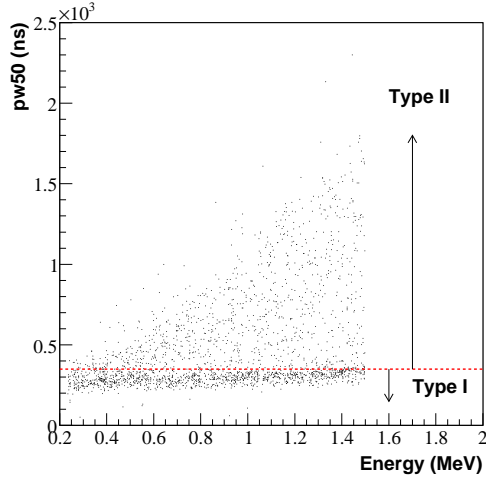


Figure 6.1: String 10 data, showing type I and II alphas in pulse width vs energy space.

Narrow surface ^{210}Po α events with $pw50 < 350$ ns, and ^{238}U pulses with $pw50 > 350$ ns¹, are chosen as templates for I and II, respectively. Using Monte Carlo simulations, it can be demonstrated that pulse moment² and $R_{10,40}$ distributions from *any* exponential depth profile can be decomposed accurately into I and II. Other shape parameters (*e.g.* mean and RMS) are less stable with respect to \bar{d} . This is shown explicitly for ^{238}U α events in table 6.1, where pulse shape parameter pdfs (mean, RMS, $m3$, $m4\dots m8$ and $R_{10,40}$) at various depths \bar{d} are broken into type I and II pdfs. K-S probabilities of the decompositions, assuming the values of x_I and x_{II} in the second column, are displayed for each variable in columns 3 to 11.

Fig. 6.2 shows distributions of the mean, RMS, and moments $m3$, $m4\dots m8$ of pulses in the energy range 0.2–1 MeV from MUX 1, 5 and 11, hand-fitted to neutrons³ (red), type I (magenta) and type II alphas (green). It is much harder to reach the same level of agreement in pulse moment distributions if the $\{^{238}\text{U}, ^{232}\text{Th}, ^{210}\text{Po}\}$ basis is adopted, because accurate values of \bar{d} are needed for each string in order to construct a proper mixture.

Let us summarize by stressing the two main benefits of using the $\{I, II\}$ α representation described above:

- (1) One avoids the need for pre-determined \bar{d} , and ^{238}U , ^{232}Th and ^{210}Po fractions for

¹The justification for the cut is that narrow bulk pulses mimic ^{210}Po pulses.

²Moments m_i are defined in appendix D.

³The neutron pdf is obtained from ^{24}Na calibration source data.

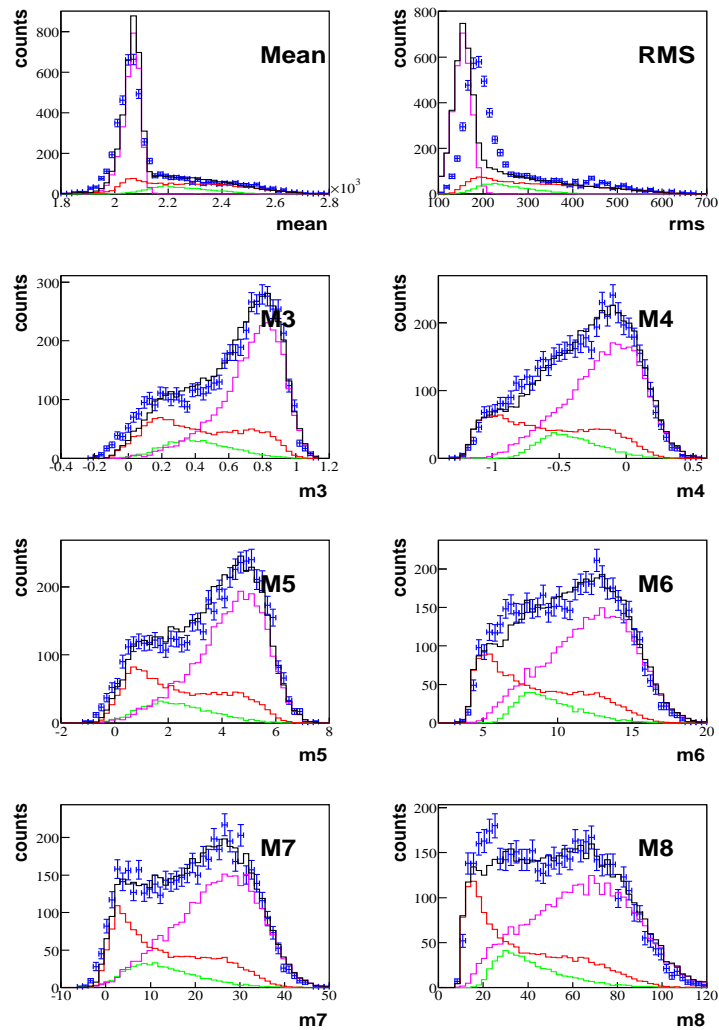


Figure 6.2: MUX 1, 5 and 11 neutrino data (blue) in the energy region 0.2–1 MeV, decoupled into neutrons (red), type I (magenta) and type II alphas (green). The relative fractions were roughly eyeballed to be 0.3, 0.6 and 0.1. According to table 6.1, mean and RMS pdfs are not accurately described in the {I, II} basis at all depth scales. Therefore, fits of lesser quality result in the top two plots.

depth $\bar{d}(\mu\text{m})$	ratio I:II	K-S probability								
		mean	RMS	$m3$	$m4$	$m5$	$m6$	$m7$	$m8$	$\frac{pw10}{pw40}$
2	0.67:0.33	0.	0.	0.33	0.62	0.47	0.44	0.14	0.13	0.71
3	0.41:0.59	0.	0.	0.2	0.47	0.23	0.43	0.21	0.23	0.89
4	0.26:0.74	0.	0.002	0.12	0.68	0.34	0.69	0.37	0.91	0.26
5	0.26:0.74	0.	0.	0.71	0.30	0.70	0.37	0.69	0.33	0.18
6	0.17:0.83	0.004	0.20	0.23	0.75	0.26	0.54	0.24	0.59	0.99
8	0.13:0.87	0.001	0.02	0.24	0.68	0.57	0.60	0.62	0.75	0.30
10	0.13:0.87	0.04	0.21	0.41	0.51	0.26	0.22	0.23	0.26	0.96
15	0.05:0.95	0.9	0.97	0.4	0.92	0.59	0.91	0.57	0.74	0.99
20	0.05:0.95	0.96	0.88	0.95	0.93	0.81	0.92	0.89	0.86	0.49

Table 6.1: The pdfs of certain pulse shape parameters are equivalently described in bases $\{^{238}\text{U}, ^{232}\text{Th}, ^{210}\text{Po}\}$, or $\{\text{I}, \text{II}\}$. In this example, ^{238}U pdfs at different \bar{d} are decomposed into type I and II pdfs. 1st column: mean depth of ^{238}U sample. 2nd column: approximate type I and II fractions comprising the sample. Subsequent columns: K-S probability of pulse parameter pdfs (mean, RMS, $m3$, $m4$... $m8$ and $R_{10,40}$) from the Monte Carlo generated ^{238}U sample being compatible with pdfs from the I-II mixture. The highlighted variable is selected for n - α separation.

each string when describing some alpha parameter distributions. The generation of Monte Carlo pdfs and analysis of data is simplified.

- (2) Effects of depth profile systematic errors on some pulse shape parameter distributions are substantially mitigated, as a result of (1).

The main disadvantage is that $\{\text{I}, \text{II}\}$ is not the physical basis, *i.e.* no meaning can be assigned to type I and II pulses, except that one class is, in general, narrower than the other. Moreover, not all variables can be decomposed at every value of \bar{d} . An optimal choice of type I and II templates, which makes this possible, might exist. With the type I and II prototypes used in this work, ‘good’ variables in the $\{\text{I}, \text{II}\}$ basis are *relative* quantities of some sort, *e.g.* ratios of widths and centralized moments.

6.2 Alpha $R_{10,40}$ parameter distributions

The pulse simulation is not perfect, implying that MC calculated pdfs are inevitably biased (*e.g.* as in §4.6.1 for neutrons). The major sources of discrepancies in $R_{10,40}$ parameter pdfs have to be identified, and corrections derived. These are described below.

6.2.1 Instrumental systematics

One advantage of using $R_{10,40}$ is that systematic corrections to account for incomplete hardware modelling are rather straightforward to implement. The two dominant sources of systematic biases that need to be considered here are:

(1) MUX corrections

Fig. 6.3 (left) shows the energy dependence of the mean value of $R_{10,40}$ for pulses with $pw50 < 350$ ns, from strings connected to MUX 4 (red, excluding the ^4He string 10), compared with the remaining boxes (black). String 10, shown in blue, is also connected to box 4, and is consistent with the red curve. This suggests that it is reasonable to use data from ^3He strings, to correct for electronic biases in boxes 1, 5 and 11. The Monte Carlo type I alphas are shown in green. At any energy E , a mean shift of $\Delta R_{10,40} = f_4(E) - f_{MC}(E)$ and $\Delta R_{10,40} = f_{1,5,11}(E) - f_{MC}(E)$ can be applied to the Monte Carlo calculated $R_{10,40}$, to predict expected values from the associated MUX. The $f(E)$ are cubic curves fitted to the data points in fig. 6.3, with coefficients given in table 6.2. Uncertainties on $\Delta R_{10,40}$ can be derived, and are of the order of ± 0.01 for boxes 1, 5 and 11, and ± 0.04 for box 4. Systematic corrections to Monte Carlo-generated type II alpha pdfs are found in the same way. In general, differences between boxes are less substantial than in the type I case.

(2) Width smearing corrections

Type I alpha $R_{10,40}$ distributions are rather narrow. Therefore, any mechanism that induces counter-to-counter variations in $pw10$ or $pw40$ has an impact on the width of $R_{10,40}$. Some of these processes, which are not included in the simulation are: (a) the amplitude of the reflected pulse component at the preamplifier, which depends on the degree of impedance mismatches, (b) dispersion in varying NCD cable lengths and electronic circuits, and (c) fluctuations in counter-by-counter gas properties. Therefore, simulated $R_{10,40}$ distributions need to be smeared before analysis. The additional variance is estimated from a number of sources, which are summarized in table 6.3.

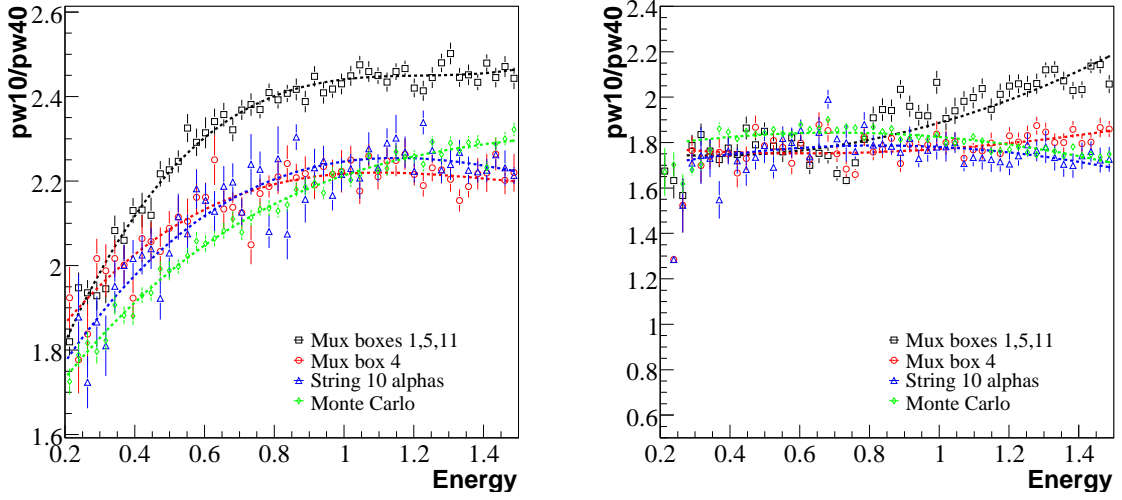


Figure 6.3: Biases on the mean value of $R_{10,40}$, due to MUX hardware differences. Left: type I pulses ($pw50 < 350$) ns. Right: type II pulses ($pw50 > 350$) ns. The curves are parametrized in table 6.2.

	a_0	a_1	a_2	a_3
f_{MC}	1.495	1.311	-0.760	0.160
I f_4	1.566	1.754	-1.603	0.493
$f_{1,5,11}$	1.374	2.666	-2.231	0.625
II f_{MC}	1.777	0.221	-0.171	0
f_4	1.753	-0.212	-0.348	0
$f_{1,5,11}$	1.823	-0.285	0.265	0

Table 6.2: Parametrization of the mean value of $R_{10,40}$ as a function of E for type I and II alphas. In the Monte Carlo, all MUX boxes share roughly the same curve.

	$\sqrt{\sigma_{data}^2 - \sigma_{MC}^2}$
^{24}Na data MUX 4 (†)	0.081
^{24}Na data MUX 1,5,11 (†)	0.135
string 10 data (†)	0.101
string 10 data (‡)	0.059
MUX 4 data (†)	0.106
MUX 1,5,11 data (‡)	0.093
Average (MUX 4)	0.09 ± 0.02
Average (MUX 1,5,11)	0.11 ± 0.02

Table 6.3: Variances of simulated $R_{10,40}$ pdfs are lower than observed. Corrections are derived for each box by using ^{24}Na calibration data and neutrino data above 1 MeV. †: neutron energy range (0.2–1 MeV); ‡: 1–1.2 MeV. String 10 is connected to box 4.

Source	Value	Ref.
e^- drift time scaling	$10 \pm 4 \%$	§3.3.1
Ion mobility	$1.082 \pm 0.027 \times 10^{-8} \text{ ns}^{-1}\text{V}^{-1}$	[65]
Space charge offset	154 ± 31	§5.2.3
Space charge gradient	782 ± 120	§5.2.3
Bulk and ^{210}Po impurity depths \bar{d}	negligible in {I,II} basis	§5.6

Table 6.4: Summary of physics model input parameter uncertainties.

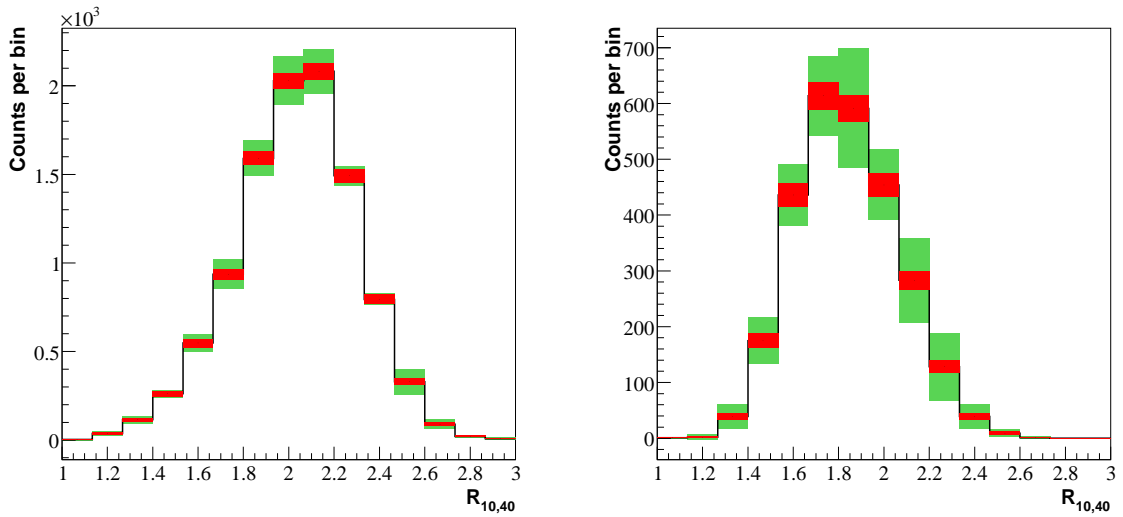


Figure 6.4: The impact of physics model uncertainties on $R_{10,40}$ distributions. Left: type I α s; right: type II α s. The red bands are statistical errors, while the green bands are the total error (*i.e.* the sum of all systematic deviations from the various physics model uncertainties, plus statistical errors).

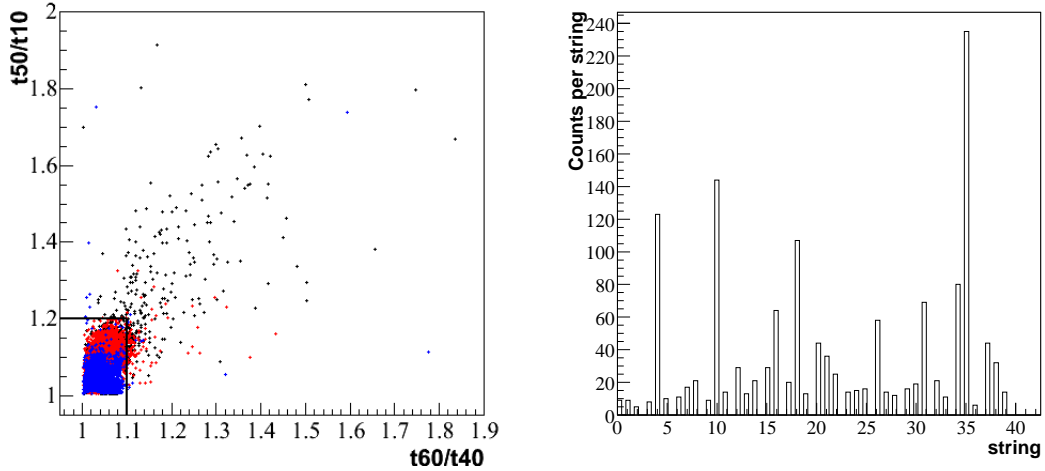


Figure 6.5: Left: end-cap alpha cut on string 10 data (black dots), with MC bulk alphas in red and ^{210}Po pulses in blue. Right: string-by-string distribution of events satisfying $\frac{t50}{t10} > 1.2$ and $\frac{t60}{t40} > 1.1$.

6.2.2 Physics model uncertainties

Pulse input parameters that have an impact on $R_{10,40}$ are listed in table 6.4, with their estimated errors. These uncertainties need to be propagated onto the extracted number of neutrons. Monte Carlo samples have been generated for this purpose, with $1\text{-}\sigma$ excursions on each input parameter. The impact of physics model uncertainties on the shape of type I and II pdfs are shown as green bands in fig. 6.4.

6.2.3 Wire, end-cap and other neutron-like alphas

A fraction of end-cap and wire connector events are indistinguishable from neutrons with large pulse widths. They distort type II $R_{10,40}$ pdfs noticeably by introducing a low tail that can be fitted as neutrons. As mentioned in §4.7.2, it is very hard to simulate these pulses correctly, and although a geometric estimate of their net abundance was made, one cannot determine accurately how many of them are in the neutron window.

A simple cut was developed to exclude a number of these events from the analysis. End-cap events typically have much longer rise-times than normal alphas. Pulses that lie outside the box

$$0 < \frac{t50}{t10} < 1.2, \quad 0 < \frac{t60}{t40} < 1.1 \quad (6.1)$$

are discarded. The t parameters are amplitude fraction times (see appendix D), *e.g.* $t50$

denotes the time bin on the leading edge of the pulse that corresponds to 50 % of the amplitude. Hence, ratios of amplitude fraction times are a good measure of how fast pulses rise. Fig. 6.5 (left) shows the scatter plot of $\frac{t_{50}}{t_{10}}$ vs $\frac{t_{60}}{t_{40}}$ for string 10, with the selected region on the lower left-hand corner. Strings with high rejection counts (4, 16 and 35) are discarded from the present analysis. In §5.6, these have also been identified as having abnormally active anodes. The neutron rejection of the end-cap cut can be determined from ^{24}Na calibration data and was found to be 0.187 ± 0.007 .

6.2.4 Comparisons with α data

Low energy α data from the NCD array is statistically limited. In particular, pure α samples in the neutron window are available only from ^4He strings, one of which has pronounced gain mismatches between individual counters. To test the corrections suggested in previous sections, the only usable data sets are: (1) data from ^4He strings 3, 10 and 30 in the 0.2–1.1 MeV energy range, and (2) backgrounds from ^3He strings, in a narrow energy range just above the neutron peak.

The first row of fig. 6.6 shows corrected Monte Carlo $R_{10,40}$ distributions, in the {I, II} basis, fitted to string 10 alpha data in the neutron energy window (left), and energy range 0.9–1.1 MeV (right). This tests the systematic corrections for MUX 4. The fit procedure is as described in §6.3.1, except for the energy cut, which is modified accordingly. The second row (left) shows corresponding fits for string 3 and 30, which are connected to boxes 1 and 5. Note that the fitted type II fraction in both cases decreases in the neutron window. The last row are fits to strings connected to boxes 1, 5, and 11 (right), and box 4 (left) in the energy ranges 0.9–1 MeV.

Agreement between data and MC in the neutron energy range is very good. The MC is assumed to be in a position to produce $R_{10,40}$ pdfs for the extraction of neutrons, which is tackled in the next section.

6.3 Extraction of neutrons

6.3.1 Fit procedure

^3He data from the 385 live days of the NCD phase is fitted to ^{24}Na calibration neutrons and Monte Carlo $R_{10,40}$ pdfs using a binned maximum likelihood method. It is assumed

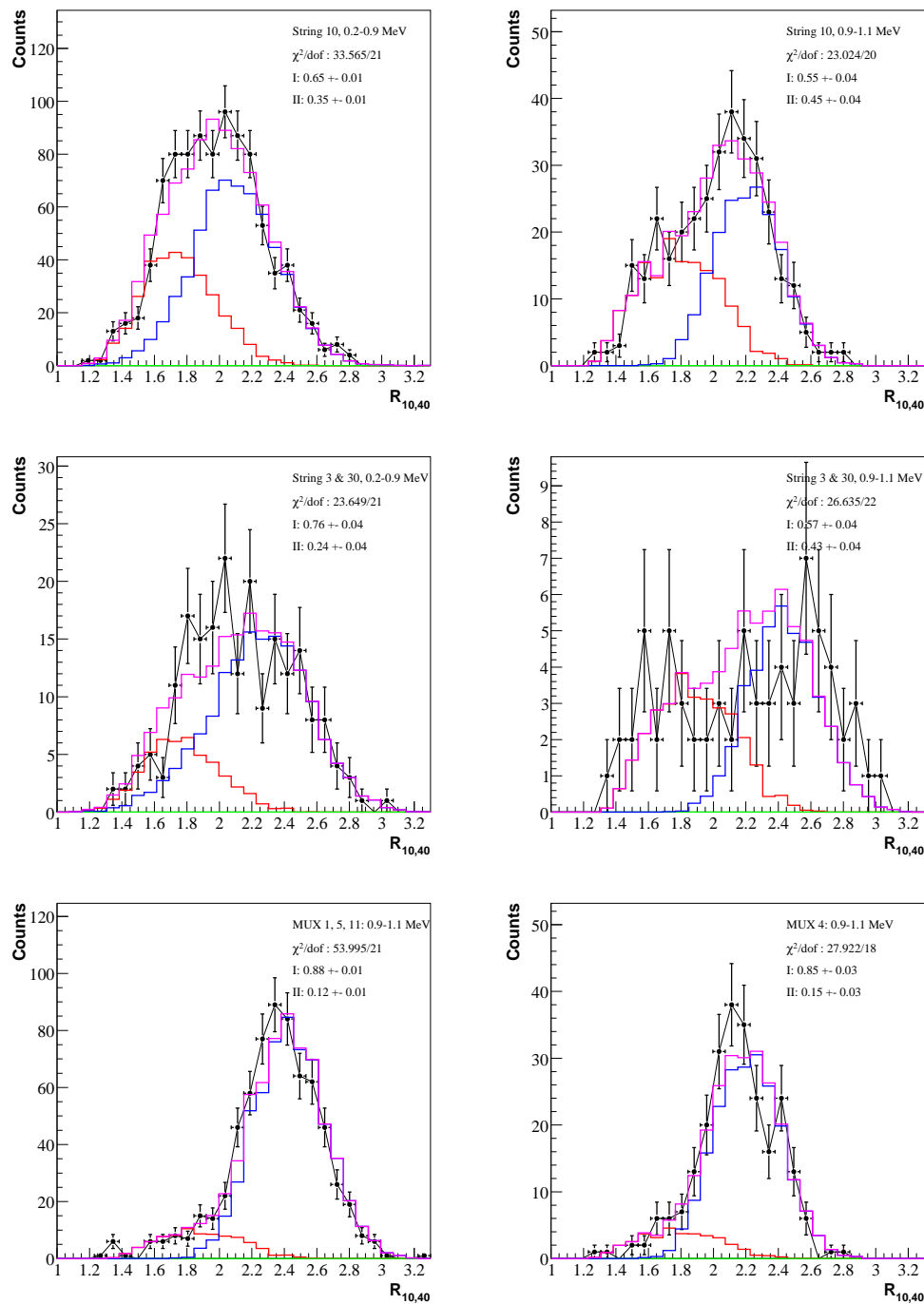


Figure 6.6: Comparisons of MC $R_{10,40}$ distributions with α data. Instrumental corrections and end-cap/quartz alpha cuts have been applied to data and MC. First row: fits to string 10 distributions to Monte Carlo type I (blue) and II (red) alpha pdfs. Left: 0.2–0.9 MeV; right: 0.9–1.1 MeV. Second row, left: strings 3 and 30 alphas in the energy range 0.2–0.9 MeV. Right: strings 3 and 30 alphas in the energy range 0.9–1.1 MeV. Last row, left: MUX 1, 5 and 11 (0.9–1.1 MeV). Right: MUX 4 (0.9–1.1 MeV). ^4He strings and strings 0, 1, 8, 18, 26 and 31 are excluded in the last row.

that there are no background instrumentals⁴, and that the number of β events is negligible (as estimated in §5.7.1). Only correlated scope-shaper pairs are considered, and the data cleaning cuts of Deng and Tolich [34, 35] are applied. The following additional cuts are applied to both data and MC:

- (1) $0.4 < E < 0.9$ MeV
- (2) $0 < \frac{t50}{t10} < 1.2$ and $0 < \frac{t60}{t40} < 1.1$
- (3) ^4He and strings 0, 1, 8, 18, 26 and 31 are excluded⁵, as recommended by [31]. Strings 4, 16 and 35 are also removed (§6.2.3).

Cut (1) discards pulses below 0.4 MeV, where α backgrounds are overwhelming, while (2) removes non-standard α events that, at the time of writing, are not correctly simulated (§6.2.3).

The fit statistic is defined as [93]:

$$\begin{aligned}\chi^2 &= 2 \sum_i D_i \ln \left(\frac{D_i}{M_i} \right) + M_i - D_i \\ M_i &= x_{\text{I}} \alpha_i^{\text{I}} + x_{\text{II}} \alpha_i^{\text{II}} + x_n N_i\end{aligned}\tag{6.2}$$

where D , M , α and N denote data and total expectation, alpha and neutron histograms, respectively. The x denote relative fractions. Estimates for x_{I} and x_{II} in the range 0.9–1.1 MeV (fig. 6.6) are used as starting values in the fit. There are only two fit parameters: x_{I} and x_{II} , with the neutron fraction constrained by $x_{\text{I}} + x_{\text{II}} + x_n = 1$.

The data is split in two groups, which are independent of each other: one smaller sample, containing events from strings connected to box 4, and a larger set for boxes 1, 5 and 11. This segregation is necessary, because the two groups require their own systematic corrections, and thus, different pdfs for ^{24}Na neutrons and type I, II alphas.

6.3.2 Results

Results of the fit, with physics model parameters at their central values, can be seen in fig. 6.7. It appears that α backgrounds are dominated by type I pulses. The extracted

⁴After applying data cleaning cuts, no evidence of non-neutron and non-alpha events have been found in any strings except 0, 8 and 26 [94], which are removed from the analysis.

⁵0, 8, & 26: for instrumental backgrounds; 1: for electrical disconnections [29]; 31: for electrical disconnections and radioactive hotspot; 18: for counter gain mismatches and radioactive hotspot.

neutron fraction in the selected MUX 4 data is 0.15 ± 0.05 , and 0.34 ± 0.04 for boxes 1, 5 and 11 combined. The different systematic error contributions to the neutron fraction, from model parameters and correction variables, are listed in table 6.5. These were estimated by extracting neutron fractions with independent $1\text{-}\sigma$ excursions on each source. Since $R_{10,40}$ involves pulse widths, the drift time uncertainty is the largest model systematic.

Source	MUX 4	MUX 1,5,11
$\Delta R_{10,40}$	± 0.0037	± 0.0064
Width smearing	± 0.0217	± 0.0025
e^- drift time	± 0.0151	± 0.0155
Ion mobility	± 0.0022	± 0.0082
Space charge offset	± 0.0096	± 0.0003
Space charge gradient	± 0.0072	± 0.0055
Total	± 0.029	± 0.020

Table 6.5: Systematic error estimates on extracted neutron fractions.

The 385 live days of the NCD phase produced 1,417,811 raw triggers, resulting in 91,631 correlated scope-shaper pairs passing all data cleaning cuts. Of these, 786 and 2,267 events from MUX 4 and MUX 1, 5, 11 passed the cuts (1)–(3). Given the neutron acceptance of cut (2) (0.813), the total number of neutrons detected in selected strings is found to be $1093 \pm 122(\text{stat.}) \pm 63(\text{sys.})$. The total systematic error is roughly 6 %.

6.4 The neutral current flux

The number of NC events per day, R_{NC} , is given by:

$$R_{NC} = \frac{f \cdot n_{total} - n_{BG}}{\epsilon_{NCD} \cdot \epsilon_{cut} \cdot T} \quad (6.3)$$

where $T = 385.17 \pm 0.14$ is the total number of live days [37]. n_{total} is the neutron number extracted in the previous section, and $n_{BG} = 185.6 \pm 24.6$ is the total number of detected background neutrons, as determined by other authors. The various contributions to n_{BG} are listed in table 6.6. ϵ_{NCD} is the neutron detection efficiency of the array (excluding strings 0, 1, 8, 18, 26, 31), determined by the neutron calibration group to be 0.211 ± 0.007 [95]. $\epsilon_{cut} = 0.862 \pm 0.004$ is a correction due to trigger thresholds, data cleaning cuts, and the requirement that scope-shaper pairs should be correlated [34, 96]. $f = 1.118 \pm 0.013$

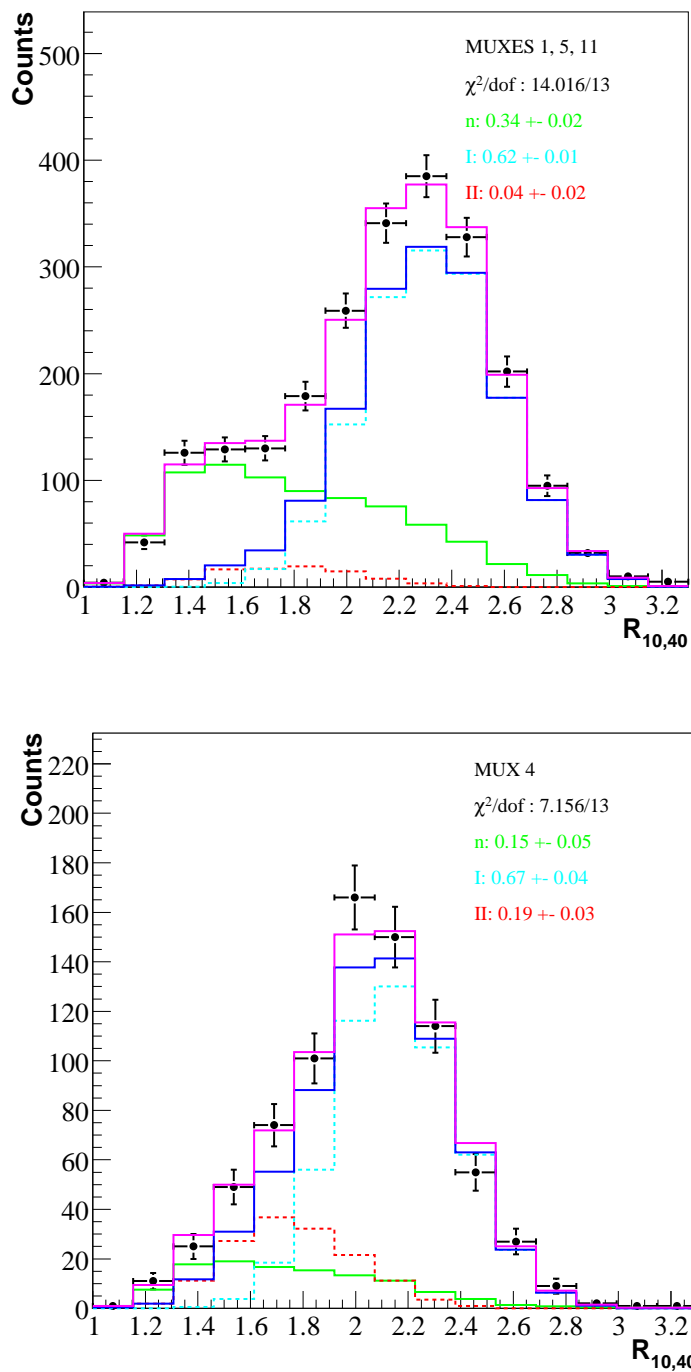


Figure 6.7: NCD phase data (black markers) fitted to ^{24}Na neutrons (green), and Monte Carlo type I (dashed cyan) and II alphas (dashed red). Combined backgrounds are shown in blue. The energy range is 0.4–0.9 MeV. Top: strings connected to MUX 1, 5 and 11. Bottom: strings connected to MUX 4.

is a correction factor, derived from ^{24}Na calibration data, to take into account the fact that 3 additional strings (4, 16 and 35) are excluded from this analysis.

Source	Detected neutrons	Ref.
U/Th in D ₂ O	28.7±4.7	[97]
U/Th in NCD bodies	27.6±9.6	[36]
string 18 hotspot	31.6±3.7	[98]
string 31 hotspot	32.8±5.2	[98]
H ₂ O and AV neutrons	40.9±20.6	[97, 99]
U/Th in NCD cables	8.0±4.0	[100]
Atmospheric	13.6±2.7	[101]
Other	2.3±0.3	[101]
Total	185.6±24.6	

Table 6.6: Neutron backgrounds in the NCD array.

Using these numbers, one gets $R_{NC} = 14.8 \pm 2.0$ (stat.) ± 1.0 (sys.) day⁻¹. Assuming the ^8B neutrino spectrum measured by Ortiz *et al.* [102], this translates into an NC flux of:

$$\Phi_{NC} = 5.74 \pm 0.77 \text{ (stat.)} \pm 0.39 \text{ (sys.)} \times 10^6 \text{ cm}^{-2}\text{s}^{-1} \quad (6.4)$$

in agreement with the BS05 SSM, which predicts a total solar ^8B neutrino flux of $5.69 \times 10^6 \text{ cm}^{-2}\text{s}^{-1}$ [18].

Jamieson [103], Loach [32] and Goon [104] extracted the NC flux by fitting the shaper energy spectrum (0.4–1.4 MeV) from the NCD array to the following pdfs: (1) a neutron energy spectrum, from ^{24}Na source calibration, (2) instrumental background pdfs derived from the problematic strings 0, 8 and 26, and (3) a net α background pdf generated by Monroe [61], using the simulation presented in this thesis. Their results are, respectively: $5.54^{+0.33}_{-0.31}$ (stat.) $^{+0.36}_{-0.34}$ (sys.) $\times 10^6 \text{ cm}^{-2}\text{s}^{-1}$, $5.44^{+0.329}_{-0.327}$ (stat.) $^{+0.318}_{-0.301}$ (sys.) $\times 10^6 \text{ cm}^{-2}\text{s}^{-1}$, and 5.39 ± 0.36 (stat.) ± 0.22 (sys.) $\times 10^6 \text{ cm}^{-2}\text{s}^{-1}$, which are all consistent with Eq. 6.4.

6.4.1 Discussion

The neutron extraction method presented here makes use, almost exclusively, of the shape of MUX-scope pulses. Energy information is used only to place the cut (1) in §6.3.1, and to correct for charge-dependent instrumental systematics. Therefore, the NC flux obtained above is an independent verification of results based on shaper energy fits [103,

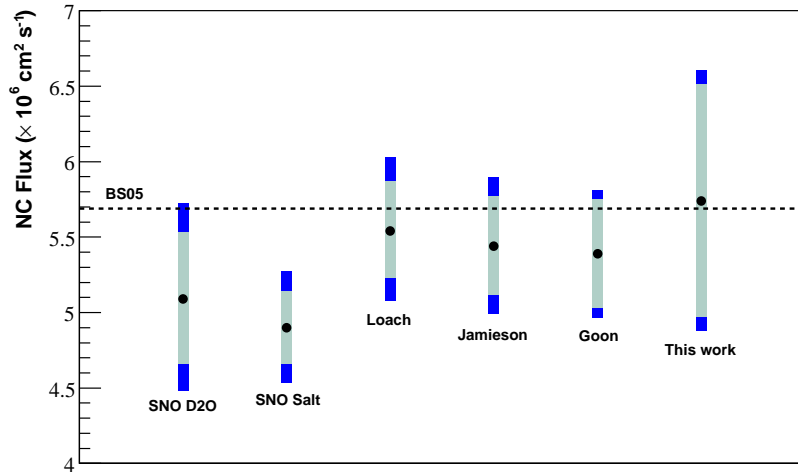


Figure 6.8: The NC flux result of this work, compared with previous SNO measurements from the first two phases [12, 27], and the shaper energy fit results of Jamieson, Loach and Goon [103, 32, 104]. Statistical errors are in light blue, while the total error is shown in dark blue. The dotted line is the BS05 SSM prediction [18].

32, 104], and also of previous SNO NC flux measurements [12, 27] (fig. 6.8). The statistical uncertainty on the extracted flux (Eq. 6.4) is higher than what is typically obtained from an energy fit, because the neutron-alpha separation power of $R_{10,40}$ is relatively worse.

As mentioned in §4.7, at least $\sim 1\%$ of all alpha pulses are not properly simulated. Efforts were made to identify, and remove these events from the analysis data set (§6.2.3). However, some neutron-like alphas may survive this cut, and be included in the extracted neutron number. A derivation of the neutron number that is based uniquely on an energy fit is more opaque to this problem, because the spectrum of end-cap α events should be rather flat, and is, thus, ‘absorbed’ into the spectra of other alpha types. An accurate estimate of the neutron-like alpha contamination is difficult without a reliable end-effect pulse simulation, which is beyond the scope of this thesis.

Chapter 7

Summary and Conclusions

A simulation of the SNO ^3He proportional counters was developed. This thesis discusses all aspects of the model, and uses it to extract the total ^8B solar neutrino flux. The work covered in previous chapters is briefly summarized here:

An electron transport simulation was developed to evaluate the radial dependence of drift times inside NCDs. CF_4 is one of the harder gases to simulate. Therefore, the code was first benchmarked against drift speed measurements for a number of common proportional counter gases, and good agreement was found. The drift speed calculations for 85:15 $^3\text{He}:\text{CF}_4$, however, had to be scaled by +10 % to comply with wire alpha studies. The effect of electron diffusion on the time resolution of pulses was evaluated. The electron transport code was also used to simulate electron avalanches near NCD anodes in order to investigate their properties.

A simulation of p - t and α particle trajectories was carried out using the ZBL method. This implements the effects of lateral straggling on pulses in a natural way. The consequences of the energy straggling of protons, tritons and alphas in the gas were investigated and found to be negligible. The straggling of α particles in the walls, however, can have significant effects on the shape of energy spectra. It was therefore parametrized and implemented in pulse calculations.

NCD pulses were calculated using a numerical method that applies to every kind of ionizing particle. Effects of NCD hardware on pulse shapes, such as preamplifier reflections and noise, were implemented. The simulation was tuned and validated by comparing with data taken during neutron calibrations. These comparisons led to the identification of non-standard alpha events such as wire and end-cap events. They were estimated to comprise

$\sim 2\%$ and $\sim 1\%$ of all alphas, respectively.

A detailed alpha background spectrum model was built. A simple space charge model was integrated within the pulse simulation to explain quantitatively certain features of mono-energetic spectra. Evidence for both the embedding of ^{210}Po (or Pb) nuclei and the non-uniformity of U/Th daughters are provided. Good agreement between simulated α spectra and data is obtained when the non-uniformity of impurities is accounted for. This allowed the mean impurity depths and ^{238}U , ^{232}Th and ^{210}Po α background fractions in each string to be estimated by means of energy fits. β energy spectra are also calculated. The expected number of β events in the NCD phase is estimated and found to be negligible.

MC generated alpha width ratio ($R_{10,40}$) pdfs were used to perform a ‘shape-only’ separation of NCD neutrons and alphas. The $R_{10,40}$ pdfs were first validated through comparisons to ^4He and ^3He data, after making corrections to existing biases. A change of pdf basis rendered impurity depth uncertainties, which are otherwise the dominant systematic error source in the α model, negligible. The systematic error on extracted neutron fractions using this method was estimated to be $\sim 6\%$. The NC flux was determined to be $\Phi_{NC} = 5.74 \pm 0.77$ (stat.) ± 0.39 (sys.) $\times 10^6 \text{ cm}^{-2}\text{s}^{-1}$. This is an independent confirmation of NC flux numbers derived via energy spectrum fits, and of the result published in [105].

Appendix A

String-by-string differences

String-by-string differences in simulation inputs were implemented in cases where measurements exist. These include: counter-by-counter gain variations, log-amplifier parameters (measured periodically during calibration runs), baseline noise variations, trigger threshold variations, counter-by-counter wall thicknesses, preamplifier RC constants, and shaper resolution. Table [A.1](#) lists the lengths, number of counters, MUX box number, and preamplifier RC constants associated with each string. Strings are otherwise assumed to be identical to each other in the model. Quantities that fluctuate from string to string, and which have been assumed to be uniform include: gas mix, electron drift times, space charge parameters, and reflection coefficients.

string	name	length (m)	counters	MUX	cable delay (ns)	RC_{preamp} (ns)
0	N4	11.19	4	11	94	3.11
1	M8	10.70	4	1	105	3.28
2	K8	10.21	4	5	114	3.35
3	I7	9.20	4	1	123	3.04
4	J8	9.70	4	4	119	3.28
5	L2	10.70	4	5	107	3.04
6	J7	9.62	4	1	117	3.04
7	M7	10.69	4	4	105	3.04
8	K7	10.21	4	11	113	3.11
9	I8	9.20	3	5	123	3.28
10	I6	9.20	4	4	123	3.04
11	K6	10.20	4	1	114	3.11
12	M6	10.64	4	5	107	3.04
13	J6	9.70	4	11	119	3.41
14	N3	11.20	4	1	93	3.04
15	L3	10.70	4	4	108	3.61
16	J5	9.66	4	5	117	3.14
17	M5	10.70	4	11	106	3.31
18	K5	10.20	4	4	114	3.41
19	I5	9.20	3	1	124	3.4
20	I3	9.20	4	11	124	3.61
21	K4	10.20	4	5	114	3.04
22	M4	10.70	4	1	105	3.41
23	J4	9.70	4	4	119	3.04
24	L4	10.67	4	11	112	3.41
25	N2	11.20	4	4	93	3.11
26	J3	9.71	4	1	119	3.41
27	M3	10.69	4	5	105	3.46
28	K3	10.21	4	11	113	3.14
29	I4	9.20	3	4	124	3.04
30	I2	9.20	4	5	123	3.14
31	K2	10.21	4	1	113	3.3
32	J2	9.68	4	11	119	3.3
33	M2	10.70	4	4	104	3.69
34	L1	10.70	4	1	106	3.46
35	J1	9.70	4	5	119	3.21
36	I1	9.19	3	11	124	3.61
37	K1	10.20	4	4	113	3.14
38	M1	10.67	4	11	105	3.55
39	N1	11.20	4	11	96	3.61

Table A.1: String names, lengths, number of counters, associated MUX box, cable delay times and preamp RC values.

Appendix B

^{238}U and ^{232}Th chains

URANIUM - RADIUM $A = 4n + 2$						Th 234 Q β 0.199 70.3% 0.107 19.2% 0.106 7.6%	Th 234 24.10 d	U 238 4.468 $\cdot 10^9$ a		
			Bi 214 Q β 3.272 18.2 % 1.894 7.43% 1.542 17.8 % 1.308 17.02% 1.425 8.18% 1.068 5.72%				Pa 234 Q β 0.642 19.4% 0.502 7.0% 0.4721 12.4% 0.4716 33 % 0.413 8 %	Pa 234m Q β 1.17 m	U 234 2.455 $\cdot 10^5$ a	
	Pb 214 Q β 1.024 6.3% 0.729 42.2% 0.672 48.9%	Pb 214 26.8(9) m	← Bi 214 6.002 99.999% 5.181 0.001%	Po 218 3.10(1) m	← Rn 222 5.490 99.92 % 4.987 0.078%	Ra 226 1600(1) a	← Th 230 4.687 76.3% 4.621 23.4%	Th 230 7.538 $\cdot 10^4$ a	← Pa 234* 6.7 h	← U 238 4.198 79.0% 4.151 20.9%
	Tl 210 1.30(3) m	← Pb 214 5.516 39.2% 5.452 53.9% 5.273 5.8%	Bi 214 19.9(4) m	← Po 218 6.693 90 % 6.653 6.4%	At 218 1.5 s					
	Tl 210 Q β 4.391 20% 4.210 30% 2.419 10% 2.039 10% 1.864 24% 1.609 7%	Pb 210 22.3(2) a	← Bi 214 7.687 99.999% 6.902 0.010%	Po 214 164.3(20) μ s						
		Pb 210 Q β 0.064 16% 0.017 84%	Bi 210 5.013 d	Bi 210 Q β 1.162						
								α E α MeV RI%	$T_{1/2}$ $\alpha\%$ $\beta\%$ $\gamma\%$	β MeV RI%
		Pb 206 stable	← Bi 210 5.304 100 % 4.516 0.001%	Po 210 138.376 d						

Figure B.1: α and β particles from the ^{238}U decay chain [106].

THORIUM $A = 4n$						Ra 228 Q β 0.040 10% 0.039 40% 0.026 20% 0.013 30%	Ra 228 5.75 a	Th 232 1.405 $\cdot 10^{10}$ a	
							Ac 228 Q β 2.069 8% 1.731 12% 1.158 30% 1.004 6%	Ac 228 6.15 h	
	Pb 212 Q β 0.574 12.3 % 0.335 82.5 % 0.159 5.17%	Pb 212 10.64(1) h	← Bi 212 6.778 99.998% 5.985 0.002%	Po 216 145(2) ms	← Rn 220 6.288 99.886% 5.747 0.114%	Ra 224 3.66(4) d	← Th 228 5.423 72.2% 5.340 27.2%	Th 228 1.9116(16) a	
	Tl 208 3.053(4) m	← Pb 212 6.090 27.12% 6.051 69.91%	Bi 212 60.55(6) m	Q β 2.254 55.46% 1.527 4.36%					
	Tl 208 Q β 1.803 48.7% 1.526 21.8% 1.293 24.5%	Pb 208 stable	← Bi 212 8.784	Po 212 299(2) ns					

Figure B.2: α and β particles from the ^{232}Th decay chain [106].

Appendix C

Semi-analytic pulse calculation

The following algorithm can be used to calculate NCD pulses in the absence of large-angle scattering:

- (1) For a given straight track, find the points that are closest and furthest to the wire, and evaluate the shortest and longest drift times from Eq. 3.16. This gives the pulse duration.
- (2) Loop over the duration of the pulse in 1 ns steps, and get the corresponding radial position r of each step by inverting the expression for t_d , Eq. 3.16. During each step, one calculates:

- (a) The point x along the track corresponding to a radial position r with the quadratic relation¹:

$$x = \frac{2r_0 \sin \theta \cos \phi \pm \sqrt{\Delta}}{2 \sin^2 \theta} \quad (\text{C.1})$$

where the quadratic discriminant Δ is given by

$$\Delta = 4r_0^2 \sin^2 \theta \cos^2 \phi - 4 \sin^2 \theta (r_0^2 - r^2) \quad (\text{C.2})$$

The track parameters r_0, θ, ϕ are defined in §4.3.3.

- (b) The energy deposited by the particle, using the SRIM range-energy relations. This is divided by W to obtain the number of primary electron-ion pairs.
- (3) Steps (1) and (2) give the number of primary electrons, as a function of time. Convolve this function with the ion tail, Eq. 4.5.

¹This follows from a simple geometric derivation that will not be given here.

- (4) Add the hardware response (§4.5).

FFT methods can be used for steps (3) and (4). This pulse algorithm, coded as a standalone package, was used to verify the (default) numerical implementation, Eq. 4.1. In the absence of large-angle scattering, excellent agreement was obtained at all pulse parameters investigated, both for neutron and α events.

Appendix D

Pulse shape parameters

The following pulse shape parameters are used in this work:

(1) **Amplitude**

This is denoted by A in fig. D.1. Pulse amplitudes are measured from the baseline.

(2) **Pulse widths** $pw10, pw20\dots$

Pulse widths are measured at some fraction of the amplitude. For example, fig. D.1 shows the width at 30 % of the amplitude. This is denoted by $pw30$. The 50 % amplitude width, $pw50$, is also referred to as Full Width at Half Maximum (FWHM).

(3) **Amplitude fraction times** $t10, t20\dots$

An amplitude fraction time is defined as the time corresponding to that fraction of the amplitude, preceding the dominant peak in the pulse. For example, $t30$ is the time bin at which the pulse is at 30 % of the amplitude (see fig. D.1).

(3) **Integral rise times** $irt50, irt60\dots$

Integral rise time is defined as the time it takes for charge in the current pulse to build up to some fraction of Q_T , which is the total charge contained between $t10$ and 15000 ns. Here, $irt50$ is the integral rise time corresponding to 50 % of Q_T , etc.

(4) **Moments** $m_i, i = 1, 2\dots 8$

The i^{th} normalized central moment of a pulse P is defined as:

$$m_i = \sum_{j=t10}^{pw10+t10} P_j \frac{(j - \mu)^i}{\sigma^i} \quad (\text{D.1})$$

where j runs from t_{10} to $pw_{10} + t_{10}$. P_j is the pulse amplitude of the j^{th} bin. The sum is truncated at $pw_{10} + t_{10}$, to avoid taking into consideration differences in the tail of pulses, which is a source of discrepancies between data and MC (see §4.6.1). The pulse mean μ and RMS σ are also calculated with this restriction.

The 3rd (m_3) and 4th (m_4) moments are also referred to as *skewness* and *kurtosis*.

(5) $R_{10,40}$

This quantity is defined as the ratio of the 10 % and 40 % pulse widths: $\frac{pw_{10}}{pw_{40}}$.

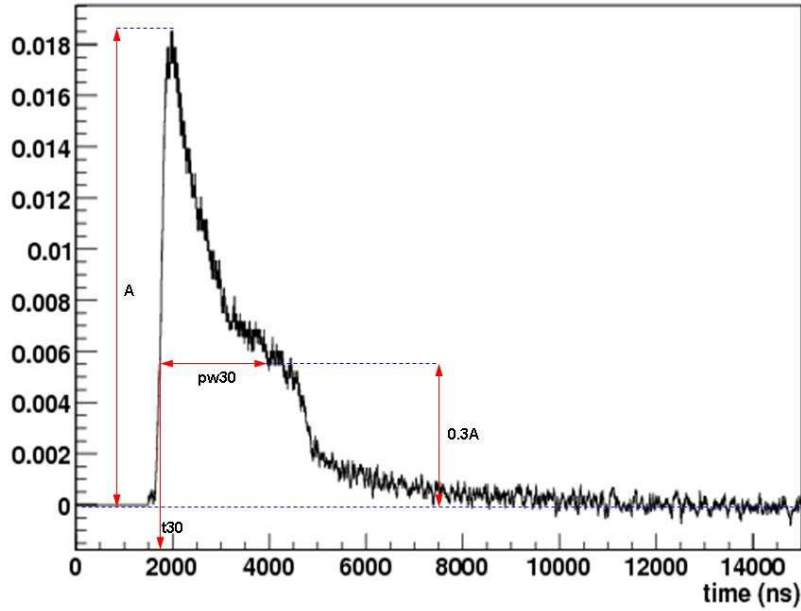


Figure D.1: Definitions of pulse widths and amplitude rise times

Appendix E

Software implementation

- (1) The proportional counter pulse simulation code is integrated within SNOMAN, the FORTRAN77-based, multi-purpose SNO simulation program. In addition to utility routines (*e.g.* for random number sampling and interpolation), SNOMAN provides the necessary geometric framework for all aspects of the SNO detector. The following packages are used by the pulse simulation code within SNOMAN: (1) MCNP [85], to propagate neutrons within NCDs, (2) FFTW [107], to handle Fourier transforms, and (3) EGS4 [74], to propagate electrons and γ -rays. Memory management is handled by ZEBRA, a CERN program library [108].

A standalone FORTRAN77 semi-analytic pulse simulation code has also been written to test the SNOMAN implementation. This package is less complete than the version that is shipped with SNOMAN.

- (2) The electron transport code described in chapter 3 is a standalone C++ program compiled with ROOT libraries [109]. All cross-section data were obtained from [42].

Both of the standalone programs mentioned above are available from the author upon request.

Appendix F

Low energy bulk α spectra

Assuming that ^{232}Th and ^{238}U impurities are uniformly distributed in the nickel wall, and that alphas start off isotropically, then for particles that come out in the gas with energy $E < 0.5$ MeV, $x = R - d$ is also uniformly distributed. This has been verified explicitly with a toy Monte Carlo. R is the maximum possible range, which depends on the starting energy in the nickel and d is the actual distance travelled by the particle in the wall.

The starting energy in the gas is found by integrating the Bragg curve curve (*i.e.* $\frac{dE}{dx}$ as a function of x) for alphas in nickel between $x = R - d$ and $x = R$. A rough functional form for the bulk energy spectrum $P(E)$ at $E < 0.5$ MeV can be calculated knowing that the probability $P(x) = C = \text{constant}$ and $\frac{dE}{dx} \approx \alpha x$ where $\alpha < 0$. The Bragg curve is approximated by a straight line since the peak occurs at ~ 1 MeV. One then has

$$P(E) = P(x) \frac{dx}{dE} \approx \frac{C}{\alpha x} \quad (\text{F.1})$$

Integrating $\frac{dE}{dx}$ with respect to x to get $x(E)$, and substituting, one gets

$$P(E) \propto \frac{1}{\sqrt{E + B}} \quad (\text{F.2})$$

where B is another constant. This function increases as $E \rightarrow 0$, but the low energy upturn is *not* observed in the data.

Appendix G

Coincidence events

The ^{220}Rn and ^{216}Po α coincidence events from the ^{232}Th chain provide an opportunity to examine the energy spectra of mono-energetic α lines originating from the inside of the nickel wall. The criteria for selecting these events were: (1) Pulses should originate from the same string and occur within 1 s of each other, (2) Pulses pass all data reduction cuts, (3) The pulse width is less than 2300 ns, (4) Events from some problematic strings are neglected (0, 8, 18, 20 and 26).

Fig. G.1 (left) shows the time between events distribution of selected pulses. The decay constant corresponds to a half life of 129 ± 9 ms for ^{216}Po decay. Fig. G.1 (right) shows the string distribution of candidate events.

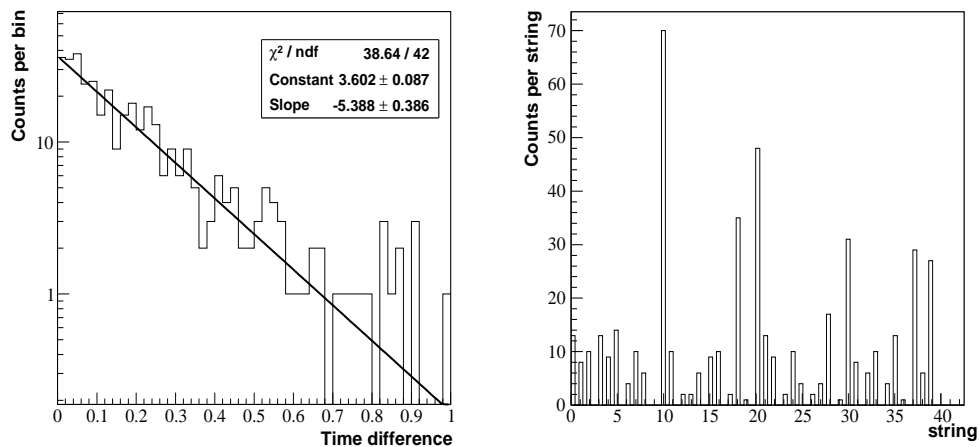


Figure G.1: Left: distribution of time differences between the first and second events in ^{232}Th double coincidence events. The extracted half life is 129 ± 9 ms. The half life of ^{216}Po decaying to alphas is ~ 145 ms. Right: string distribution of event candidates.

Appendix H

List of neutron-like alpha pulses

pulse	run	GTID	string	E	$R_{10,40}$	FWHM
1	50450	4725643	7	1.09	1.24	1631
2	51653	2188	16	1.04	1.30	2422
3	51653	82646	4	1.	1.20	1420
4	51748	3373839	15	1.03	1.24	1299
5	51760	1508786	29	1.13	1.15	1541
6	53890	510474	35	1.14	1.15	1541
7	54823	1371268	39	1.17	1.26	1864
8	54871	5425975	37	1.12	1.29	1251
9	55650	264276	4	1.06	1.26	1464
10	55702	1195423	39	0.93	1.12	1308
11	58296	10173447	16	1.16	1.27	2686
12	58452	3322213	16	1.01	1.25	2070
13	58493	408480	16	1.17	1.24	2460
14	58494	864466	29	1.16	1.22	1398
15	58507	1089093	16	1.19	1.25	2583
16	59292	1320101	4	1.13	1.15	2416
17	60207	1045740	16	0.93	1.24	560
18	60358	370997	16	1.04	1.17	1746
19	61128	2631555	4	1.15	1.28	1556
20	61208	1120158	4	1.08	1.19	2258
21	61847	893372	35	1.05	1.18	679
22	63501	581945	17	1.01	1.29	1168
23	63616	1625489	21	1.01	1.28	1584
24	63944	1493901	35	1.05	1.27	1565

Table H.1: A list of some neutron-like alpha pulses with $R_{10,40} < 1.3$ in neutrino data. Strings 4, 16 and 35 are excluded from the analysis. These 24 events can be viewed in fig. H.1.

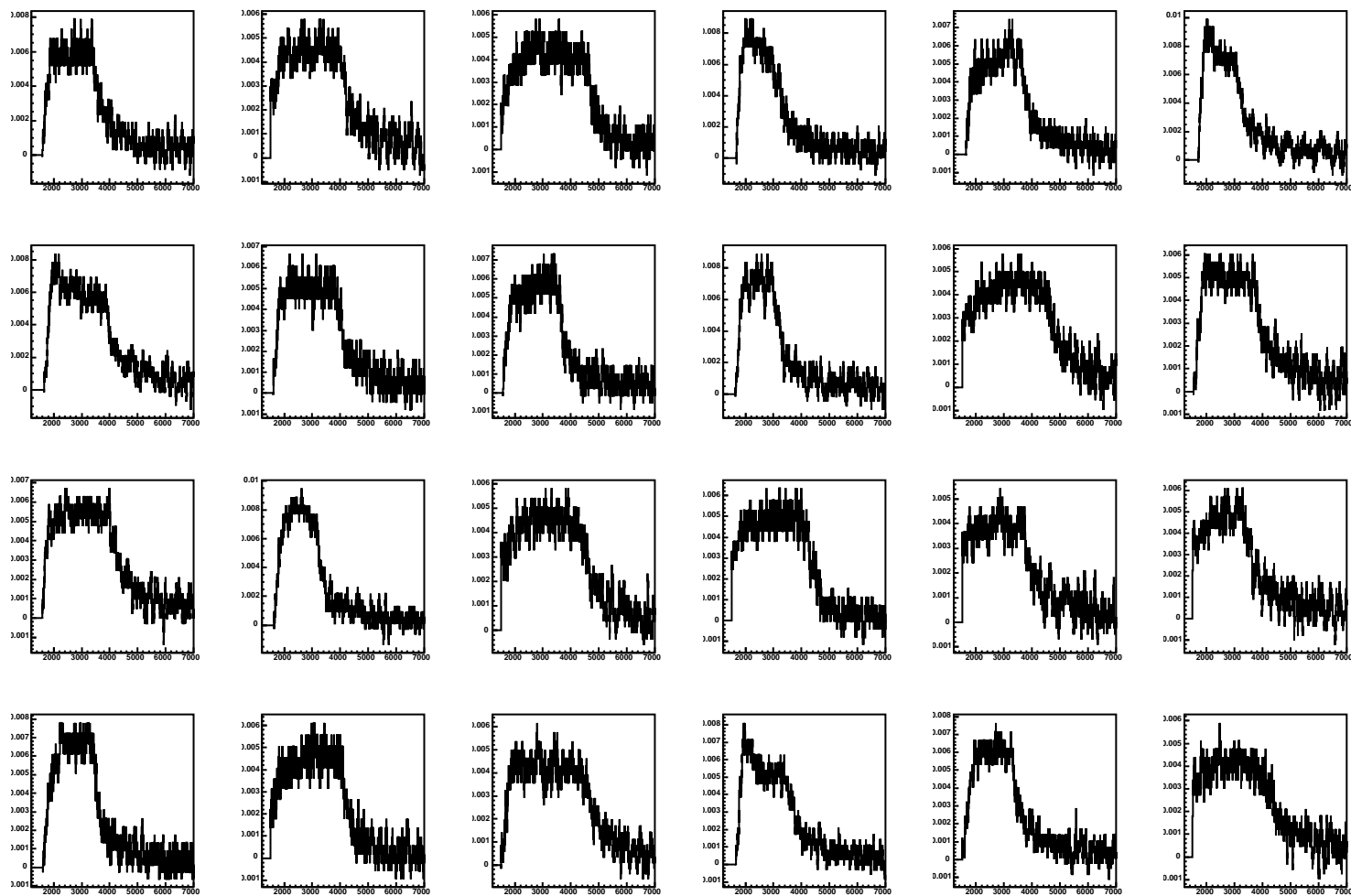


Figure H.1: The 24 neutron-like wide alpha pulse shapes with $R_{10,40} < 1.3$ in the range 0.9–1.2 MeV listed in table H.1. The numbering runs from top left hand corner (1) rightwards. Some of these events are not removed by the end-cap cut.

Bibliography

- [1] W. Pauli, Letter to a physics conference at Tübingen (1930), printed in *Physics Today* **31** (1978) 27 (Issue 9). [1](#)
- [2] F. Reines and C. L. Cowan Jr., *Phys. Rev.* **92** (1953) 830. [1](#)
- [3] F. Reines and C. L. Cowan Jr., *Nature* **178** (1956) 446. [1](#)
- [4] D. Decamp *et al.*, *Phys. Lett.* **B225** (1990) 399. [1](#)
- [5] G. Danby *et al.*, *Phys. Rev. Lett.* **9** (1962) 36. [1](#)
- [6] The DONuT Collaboration, K. Kodana *et al.*, *Phys. Lett.* **504** (2001) 218. [1](#)
- [7] C. S. Wu *et al.*, *Phys. Rev.* **105** (1957) 1413. [1](#)
- [8] M. Goldhaber *et al.*, *Phys. Rev.* **109** (1958) 1015. [1](#)
- [9] M. Apollonio *et al.*, *Eur. Phys. J.* **C27** (2003) 331. [2](#)
- [10] L. Wolfenstein, *Phys. Rev.* **D17** (1978) 2369. [2](#)
- [11] S. P. Mikheyev and A. Y. Smirnov, *Sov. Jour. Nucl. Phys.* **42** (1985) 913. [2](#)
- [12] The SNO Collaboration, Q. R. Ahmad *et al.*, *Phys. Rev. Lett.* **89** (2002) 11301. [2](#), [4](#), [123](#)
- [13] The Borexino Collaboration, C. Arpesella *et al.*, *Phys. Lett.* **B658** (2008) 101. [2](#)
- [14] The KamLAND Collaboration, K. Eguchi *et al.*, *Phys. Rev. Lett.* **90** (2003) 21802. [2](#), [4](#)
- [15] The K2K Collaboration, M. Ahn *et al.*, *Phys. Rev.* **D74** (2006) 072003. [2](#)

- [16] The MINOS Collaboration, D. Michael *et al.*, Phys. Rev. Lett. **97** (2006) 191801. [2](#)
- [17] The Super-Kamiokande Collaboration, Y. Ashie *et al.*, Phys. Rev. **D71** (2005) 112005. [2](#)
- [18] J. N. Bachcall *et al.*, ApJ **621** (2005) L85. [3](#), [122](#), [123](#)
- [19] J. N. Bachcall's home page, <http://www.sns.ias.edu/~jnb/> [3](#), [4](#)
- [20] B. T. Cleveland *et al.*, ApJ **496** (1998) 505. [3](#)
- [21] P. Anselmann *et al.*, Nucl. Phys. **B31** (1993) 117. [3](#)
- [22] M. Altmann *et al.*, Phys. Lett. **B490** (2000) 16. [3](#)
- [23] J. N. Abdurashitov *et al.*, Nucl. Phys. Proc. Suppl. **118** (2003) 39. [3](#)
- [24] The Super-Kamiokande Collaboration, J. P. Cravens *et al.*, Phys. Rev. **D78** (2008) 032002. [3](#)
- [25] S. J. Parke, Phys. Rev. Lett. **57** (1986) 1275. [4](#)
- [26] The SNO Collaboration, N. Jelley *et al.*, Nucl. Instrum. Meth. **A449** (2000) 172. [4](#), [7](#)
- [27] The SNO Collaboration, S. N. Ahmed *et al.*, Phys. Rev. Lett. **92** (2004) 181301; The SNO Collaboration, B. Aharmin *et al.*, Phys. Rev. **C72** (2005) 055502. [5](#), [6](#), [123](#)
- [28] J. F. Amsbaugh *et al.* Nucl. Instrum. Meth. **A579** (2007) 1054. [6](#), [10](#)
- [29] G. A. Cox-Mobrand, *Data Integrity and Electronics Calibration for the Neutral Current Detector Phase Measurement of the 8B Solar Neutrino Flux at the Sudbury Neutrino Observatory*, PhD thesis, University of Washington, 2008. [7](#), [11](#), [14](#), [56](#), [59](#), [60](#), [119](#)
- [30] M. K. Kopp *et al.*, Nucl. Instrum. Meth. **A201** (1982) 395. [8](#), [20](#), [28](#), [29](#), [30](#), [31](#), [33](#), [34](#)

- [31] K. Rielage, *Proposal to remove NCD strings from final NC analysis*, SNO technical report, 2007. [9](#), [119](#)
- [32] J. C. Loach, *Measurement of the Flux of ^8B Solar Neutrinos at the Sudbury Neutrino Observatory*, DPhil Thesis, University of Oxford, 2008. [10](#), [102](#), [122](#), [123](#)
- [33] M. A. Howe *et al.*, IEEE Trans. Nucl. Sci. **51** (2004) 878. [13](#)
- [34] H. Deng and J. Secret, *Data Cleaning in NCD Phase*, SNO technical report, 2008. [15](#), [119](#), [120](#)
- [35] N. Tolich, *NCD Data Cleaning: FREquency Analysis Kit*, SNO technical report. [15](#), [119](#)
- [36] H. M. O’Keeffe, *Low Energy Backgrounds in the NCD Phase of the Sudbury Neutrino Observatory*, DPhil Thesis, University of Oxford, February 2008. [16](#), [99](#), [102](#), [122](#)
- [37] J. Detwiler *et al.*, *Lifetime for the Full NCD Data Set*, SNO technical report, 2008. [16](#), [99](#), [120](#)
- [38] G. W. Fraser and E. Mathieson, Nucl. Instrum. Meth. **A247** (1986) 544. [19](#), [24](#), [32](#)
- [39] S. F. Biagi, Nucl. Instrum. Meth. **A421** (1999) 234. [19](#), [20](#), [25](#), [31](#), [32](#)
- [40] G. Schultz and J. Gresser, Nucl. Instrum. Meth. **A151** (1978) 413. [19](#)
- [41] B. T. Wu *et al.*, Eur. Phys. J. Appl. Phys. **35** (2006) 57. [19](#)
- [42] URL: <http://magboltz.web.cern.ch/magboltz/cross> [19](#), [27](#), [28](#), [29](#), [30](#), [133](#)
- [43] K. Rielage and A. Hime, private communication. [20](#), [38](#), [69](#), [85](#)
- [44] URL: <http://garfield.web.cern.ch/garfield> [19](#)
- [45] H. R. Skullerud, J. Phys. **D1** (1968) 1567. [22](#)
- [46] S. L. Lin and J. N. Bardsley, J. Chem. Phys. **66** (1977) 435. [23](#)
- [47] M. Thornton, *Classical Dynamics of Particles and Systems*, Harcourt, 4th Edition. [24](#)

- [48] S. Longo and M. Capitelli, *Plasma Chem. Plasma Process.* **14** (1993) 1. 25
- [49] J. L. Pack and A. V. Phelps, *Phys. Rev.* **121** (1961) 798. 28
- [50] J. C. Bowe, *Phys. Rev.* **117** (1960) 1411. 28
- [51] K. Yoshida *et al.*, *J. Phys.* **D29** (1996) 1209. 28, 29
- [52] J. L. Pack *et al.*, *Phys. Rev.* **117** (1960) 470. 28, 29
- [53] L. G. Christophorou *et al.*, *Phys. Rev.* **A38** (1988) 58. 30
- [54] L. G. Christophorou *et al.*, *Nucl. Instrum. Meth.* **A163** (1979) 141. 30, 31, 33
- [55] M. S. Naidu *et al.*, *J. Phys.* **D5** (1972) 983. 30, 31
- [56] R. A. Snelson, Ph.D. thesis, University of Liverpool, 1974. 30
- [57] K. J. Mathieson *et al.*, *J. Phys.* **D21** (1988) 1271. 31
- [58] J. S. Townsend *et al.*, *Phil. Mag.* **44** (1922) 1033. 31
- [59] R. W. Crompton *et al.*, *Aust. J. Phys.* **20** (1967) 369. 31
- [60] C. S. Lakshminarashimha *et al.*, *J. Phys.* **D10** (1977) 313. 31
- [61] J. Monroe, private communication. 33, 34, 35, 38, 122
- [62] J. F. Ziegler, *Transport of Ions in Matter*, Software package (2006). 33, 49, 51
- [63] G. F. Knoll, *Radiation Detection and Measurement*, 3rd edition, John Wiley & Sons. 38, 82, 90
- [64] B. Beltran, private communication. 38
- [65] N. Oblath, private communication. 38, 44, 59, 70, 85, 98, 115
- [66] A. Andronic *et al.*, *Nucl. Instrum. Meth.* **A523** (2003) 302. 38
- [67] D. H. Wilkinson, *Ionization Chambers and Counters*, Cambridge University Press, 1950. 46

- [68] W. W. M. Allison *et al.*, *Ann. Rev. Nucl. Part. Sci.* **30** (1980) 253. 49
- [69] J. F. Ziegler, J. P. Biersack and U. Littmark, *The Stopping and Range of Ions in Solids*, Pergamon Press, 1985. 49, 50, 52
- [70] H. H. Andersen and J. F. Ziegler, *Hydrogen Stopping Powers and Ranges in All Elements*, Pergamon Press, 1977. 50
- [71] J. F. Ziegler, *Helium: Stopping Powers and Ranges in All Elemental Matter*, Pergamon Press, 1977. 50
- [72] W. H. Bragg and R. Kleeman, *Philos. Mag.* **10** (1905) 318. 50
- [73] J. F. Ziegler and J. M. Manoyan, *Nucl. Instrum. Meth.* **B35** (1998) 215. 50
- [74] W. R. Nelson, H. Hirayama and D. W. O. Rogers, *The EGS4 code system*, SLAC-265 (1985). 51, 56, 103, 133
- [75] M. E. Rudd *et al.*, *Rev. Mod. Phys* **64** (1992) 441. 52
- [76] Electron Stopping Power and Range (ESTAR) program, available to run at <http://physics.nist.gov/PhysRefData/Star/Text/contents.html> 52, 54
- [77] H. Bichsel, private communication. 55, 91
- [78] H. Bichsel, *Nucl. Instrum. Meth.* **A562** (2006) 154. 55
- [79] G. A. Cox-Mobrand, private communication. 57, 61, 63
- [80] S. McGee, private communication. 58, 90
- [81] T. Burrit *et al.*, *NCD ECA Unidoc*, SNO technical report. 59
- [82] M. Huang, *Calibration of NCD Electronic (Non-LogAmp) Parameters II*, SNO technical report, 2005. 59, 61
- [83] A. W. Poon, private communication. 74
- [84] P. M. Thornewell, *Neutral Current Detectors for the Sudbury Neutrino Observatory*, DPhil thesis, University of Oxford, 1997. 77

- [85] X-5 Monte Carlo Team, *MCNP - A General Monte Carlo N-Particle Transport Code, Version 5*, Los Alamos National Laboratory. 79, 133
- [86] A. Hime, *Detector operating parameters and constraints*, SNO technical report. 80, 85
- [87] L. C. Stonehill, *Deployment and Background Characterization of the Sudbury Neutrino Observatory Neutral Current Detectors*, PhD thesis, University of Washington, 2005. 82, 95
- [88] G. Prior, *Shaper data from the ECA logamp runs for study of the electronics noise and stability over time of the electronics*, SNO technical report, 2007. 90
- [89] J. R. Comfort *et al.*, Phys. Rev. **150** (1966) 249. 90
- [90] D. A. Sykes *et al.*, Nucl. Instrum. Meth. **101** (1972) 423. 90
- [91] N. Bohr, Mat. Fys. Medd. Dan. Vid. Selsk **18** No.8 (1998). 91
- [92] R. G. H. Robertson, private communication. 95
- [93] G. Cowan, *Statistical Data Analysis*, Clarendon Press, Oxford, 1998. 98, 119
- [94] B. Monreal, *NNNA spectra on N4 and J3*, SNO technical report, 2008. 106, 119
- [95] The SNO Collaboration, *SNO NCD Phase Analysis Unidoc*, SNO technical report, 2008. 120
- [96] E. Guillian, *Final corection document*, SNO technical report, 2008. 120
- [97] H. M. O’Keeffe, *Merging of ex-situ and in-situ measurements of water radioactiviy*, SNO technical report, 2008. 122
- [98] B. T. Cleveland *et al.*, *Measurements of the activity and composition of the K5 and K2 hotspots*, SNO technical report, 2008. 122
- [99] B. Cai, C. Kraus and A. Poon, *External neutrons for the NCD phase*, SNO technical report, 2008. 122

- [100] H. M. O’Keeffe and J. C. Loach, *Captured neutrons from NCD cable radioactivity*, SNO technical report, 2008. [122](#)
- [101] J. A. Formaggio, *Other background sources for the NCD phase of the SNO experiment*, SNO technical report, 2008. [122](#)
- [102] C. E. Ortiz *et al.*, Phys. Rev. Lett. **85** (2000) 2909. [122](#)
- [103] B. Jamieson, SNO NCD Phase Signal Extraction with Integration over Systematic Nuisance Parameters by Markov-Chain Monte-Carlo, SNO technical report, 2008. [102](#), [122](#), [123](#)
- [104] J. Goon, *MXF with Scott’s SS method for the NCD Phase v.4.1*, SNO technical report, 2008. [102](#), [122](#), [123](#)
- [105] The SNO Collaboration, B. Aharmim *et al.*, Phys. Rev. Lett. **101** (2008), 111301. [125](#)
- [106] J. Farine, *New low background techniques for neutrino experiments at low energy. First Results.*, PhD Thesis, Neuchâtel University, 1996. Adapted from the Karlsruhe Nuklidkarte, 6. Auflage 1995, Pfenning *et al.*, Forschungszentrum Karlsruhe GmbH. [128](#)
- [107] FFTW software package, <http://www.fftw.org> [133](#)
- [108] CERN Program Library Long Write-up Q100/Q101, *ZEBRA*. [133](#)
- [109] R. Brun and F. Rademakers, Nucl. Instrum. Meth. **A389** (1997) 81. [133](#)